The Well-Dressed Spacecraft: Textiles for Cosmic Dust Metrology

by

Juliana Mae Cherston

B.A., Harvard University (2013)
M.A., MIT Media Lab (2016)

Submitted to the Program in Media Arts and Sciences
School of Architecture and Planning
in partial fulfillment of the requirements for the degree of

Doctor of Philosophy

at the

MASSACHUSETTS INSTITUTE OF TECHNOLOGY

September 2022

Author . . . .
Program in Media Arts and Sciences
School of Architecture and Planning
August 24, 2022

Certified by . . . .
Joseph A Paradiso
Alexander W. Dreyfoos (1954) Professor in Media Arts and Sciences
Thesis Supervisor

Accepted by . . . .
Tod Machover
Academic Head, Program in Media Arts and Sciences

The Well-Dressed Spacecraft: Textiles for Cosmic Dust Metrology

by

Juliana Mae Cherston

Submitted to the Program in Media Arts and Sciences
School of Architecture and Planning
on August 24, 2022, in partial fulfillment of the
requirements for the degree of
Doctor of Philosophy

0.0.0. Abstract

I envision cosmic grains that may have traveled light years to meet, in a microscopic blitz, the commonplace textile! This work brings the first electronic textiles to Low Earth Orbit, tracking advanced fabric sensor characterization from a tabletop laser accelerator, to a warehouse-scale electrostatic accelerator, to the walls of the International Space Station.

There is, increasingly, direct place-sharing between the specialized scientist and the lay explorer – a coexistence of scientific and humanistic pursuit that is muted in the specialized laboratories of the 20th century. When scientific and humanistic infrastructure are not gracefully coevolved, they clash. A key design vision for the current work is to propose opportunities exist to more deeply unify the infrastructural demands and desires of the explorer with the architectures that enable scientific inquiry.

For example, for decades, spacecraft and spacesuits have leveraged textile substrates as their outermost protective skins. The primary contribution of this work is the introduction of piezoelectric and charge sensitive fabric skin for sensing hypervelocity space dust, while simultaneously offering enhanced protective capabilities. Dust kinematic estimates can in turn suggest the grain's likely origin. From space webs on asteroids and 'sensory conductors' on extravehicular spacesuits to future 'textile telescopes' for sensing interstellar dust, I introduce a suite of additional conceptual avenues that together map out a landscape of opportunity for scientists and explorers alike.

Thesis Supervisor: Joseph A Paradiso
Title: Alexander W. Dreyfoos (1954) Professor in Media Arts and Sciences

The Well-Dressed Spacecraft:
Textiles for Cosmic Dust Metrology

by

Juliana Mae Cherston

This dissertation has been reviewed and approved by the following committee members:

Thesis Supervisor . . . .

Joseph A Paradiso
Alexander W. Dreyfoos (1954) Professor
of Media Arts and Sciences
MIT Media Lab

Thesis Reader . . . .

Yoel Fink
Professor of Materials Science
Joint Professor of Electrical Engineering and Computer Science
Massachusetts Institute of Technology

Thesis Reader . . . .

Hajime Yano
Department of Interdisciplinary Space Science,
Institute of Space and Astronautical Science,
Japan Aerospace Exploration Agency, Japan
Visiting Scientist, Institute of Soldier Nanotechnologies, MIT
Research Affiliate, MIT Media Lab

Acknowledgements:

This project did not happen in a vacuum.

Committee and Technical Mentors

To **Prof. Joe Paradiso** for seeing beyond black-and-white, for teaching by demonstration, and for believing the best in each of your students. Thanks also for enabling this free-spirited journey together exploring the grey area between fundamental physics and human-centered technology (which has taken multiple forms over the years).

To **Prof. Yoel Fink** for ferociously believing in this body of work and its future potential, for helping me to envision concrete future paths in research/leadership, and for teaching me the art of balancing technical rigor and storytelling.

To **Prof. Hajime Yano** for bringing the seed of this project idea to us, for helping me to appreciate how to make scientifically-minded contributions within the domain of space technology/metrology, and for patiently meeting at odd hours on Zoom (+ once in Japan!)

To Prof. Neri Oxman for helping me tap into authentic inner expression during a crucial decision point, and for appreciating the kernel of an artist in me. To Prof. Dave Miller for spending hours with me on the chalkboard demonstrating how to reason quantitatively through aerospace design decisions. To Prof. Neil Gershenfeld for teaching deeply influential courses (HTMAA and Physics of Information Tech). And thanks Prof. Kerri Cahoy, Prof. Rick Binzel, Prof. David Kaiser, Dr. Shobha Murari, Dr. Andreea Danielescu, Allison Goode, Prof. Melissa Franklin, Prof. John Parsons, and the team at Made in Space.

To Gavin Lund, Brian Mayton, Mark Feldmeier, and David Bono for mentoring me with tremendous patience over several years in electronics and PCB design. I'll pay this forward.

Financial / In-Kind Support

Thank you to the organizations and companies who have provided major financial support or in-kind support: The ISS US National Lab, Accenture, Hayashi-Ulvac fund, SpaceBD team, JPS Composite Materials team, Aegis Aerospace team, Lincoln Lab(Shock/Vibe) + Dr. Rebecca Masterson/MIT SSL(TVAC). Thank you also to Ariel Ekblaw / the MIT Space Exploration Initiative for seed funding and networking during this project's initial stages. Thanks LASP accelerator team and MIT ISN for facilitating ground-testing, specifically JSPS Kakenhi Grant Number 18KK0128 for use of the LIPIT vacuum chamber.

Project Team & Colleagues

To postdocs Wei Yan and David Veysset for demonstrating what the pairing of extreme technical competence and hard work looks like. I admire both of you. And to some other truly awesome collaborators: Yuchen Sun, Steve Kooi (for your LIPIT support), Grace Noel, Elizabeth Meiklejohn, Syamantak Payra, Irmandy Wicaksono, Joao Wilbert.

To ResEnv for our fun-filled, sun-filled, creative and open-minded lab space! Special shoutouts to textile guru Irmandy for research camaraderie, Caroline for support and accountability, David for your meaningful friendship since orientation, and Fangzheng for TVAC support. Thanks also to the Fibers@MIT group for treating me as an honorary member :) Finally, to Prof. Pattie Maes & the MIT Media Lab Festival of Learning team. The crazy-ideas talk series was a joy. I came to the Media Lab for this energy.

Personal To Dr. Mia Gore and to the Cambridge Zen Center (particularly Jane Dobisz) for helping me to grow as a whole person.

To Ina Jazic, my decade-long close friend and confidante. To my Media Lab partner-in-crime Natasha Jaques - our instant close friendship was a gift. I treasure our years hanging out at the Media Lab and beyond. To Bianca Datta for shared support and laughs through our very similar PhD journeys. To Hannah Gross, Claudia Gelfond, Sophie Rouhandeh, Sarah McCuskee for reminding me there's a life beyond this bubble. To my sister Caroline - a lifetime getting along so well, and a surprise visit at my defense! I depend on you.

To my partner Gavin Lund for sharing your anchored, clear-minded, and simplifying energy through my PhD. You have brought 6.5 years of joyful adventure! You saw all the grueling parts of this process. You are very precious.

To Mom and Dad - for remaining a selfless source of love in hard moments, for valuing my exposure to art, logic, and exploration in equal parts from a young age, for paying genuine attention to supporting my interests and inclinations, for cultivating a good spirit between Caroline and me, and for so deeply prioritizing our education.

Grade School On the note of education, I offer a hearty dose of gratitude to three grade school teachers at Dalton: Vance Condie (HS physics), Gordon Campbell (HS CS), and Ellen Stein (K-12 principal). You each provided younger me with your own flavor of mentorship that went overwhelmingly beyond your duties, and you even each paid a visit here at the Media Lab! I've continued to learn from you over the years by revisiting memories.

And to a further list of influential Dalton teachers. Thank you for encouraging me to build, write stories, play, wonder, solve puzzles, and choose the 'create your own project' option (I think you'd understand why I chose the Media Lab: a years-long Dalton lab.) Deena Amiry (French), Lisa Gross (5th grade), Carolyn Karp (7th grade English), Dianne Footlick (HS visual art), Malcolm Fenton (6th grade science), Peggy Proudfoot (Kindergarten), Ben Lesch & Sarah Levitt (3rd grade), Michael McNeill (5th grade French). I also appreciate Dalton's trusty motto, meaningful traditions, and Little Dalton music that can transport me back to age 6.

To any PhD students stumbling here: The PhD process is rarely easy, and the classic 'trust your gut' advice is the best I can offer. If you can perceive where those cliché words actually point, you will learn to make swift, effective, and difficult decisions. Yet, getting to the true heart of these words is a rigorous practice.

Contents

List of Figures

List of Tables

CHAPTER 1

Introduction

1.1 . Prelude: An Uncanny Encounter

The *uncanny*, borrowed by the Surrealists from Freud, pays heed to a particular strain of anxiety that arises when two incongruous objects are brought together by chance (Figure 1-1). In the Surrealist tradition, shock nucleates insight. Against this backdrop, the current work envisions cosmic grains that have traveled light years to meet, in a microscopic blitz, the commonplace textile!

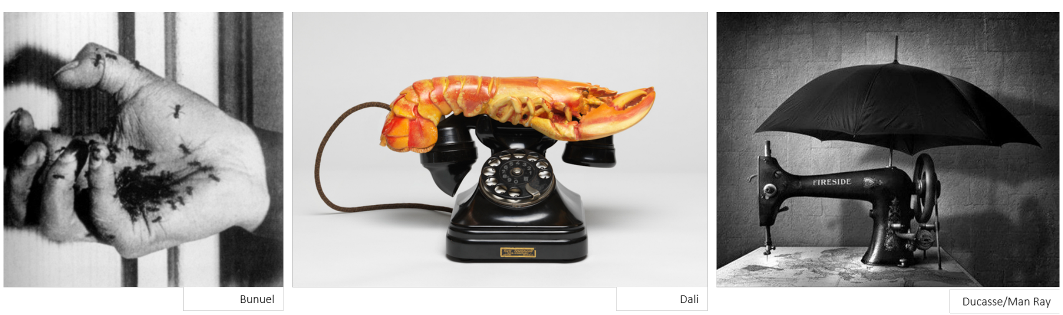

Figure 1-1: Works by Buñuel, Dali, and Man Ray on the 'uncanny encounter' - the anxiety of familiar objects considered in unfamiliar contexts

.

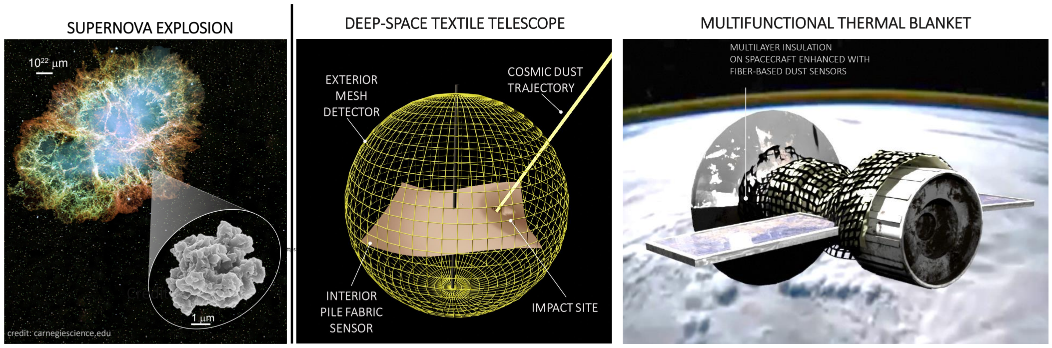

Figure 1-2: *Cosmic dust grain meets familiar textile* Left: supernova explosion and dust grain with respective scales shown. Center: Deep space "textile telescope" conceptual drawing. Right: Multifunctional thermal blanket conceptual drawing

.

In this uncanny and literally shock-inducing encounter, I aim long-term to converge the electronic-textile and astrophysics communities around the *textile telescope* - a new technology that might serve at once the scientist and the human explorer. By bridging these spheres, I also wish to create additional opportunities for designers in the hard sciences.

1.2. Textile Telescopes for Astrophysics

1.2.1. Dust Astronomy

A grain of space dust, like a photon, carries rich information from sites of cosmological intrigue across space and time. Once treated merely as a foreground in precision cosmology, these grains are increasingly appreciated for the crucial details they can offer on the dynamics of supernova explosions, the astrophysics of the interstellar medium, and potentially even the propagation of life through the galaxy. We are in the dawn of ‘Dust Astronomy’, first coined in 2001 by Eberhard Grün and further underscored in 2019 [28, 29]. The ‘Dust Telescope’, championed by Grün, Sternovsky, and others, will be this field’s essential in-situ experimental tool (see e.g. [67]).

Typically, a telescope localizes noteworthy sources using photons incident on a detection medium. Analogously, 'dust telescopes' use in-situ measurements of grains, typically trajectory/kinematic sensors and mass spectrometers, to trace their origins. As impact statistics will scale with detector area, dust telescope proposals should aggressively leverage the same advances in inflatable/deployable softgoods, in-space assembly, and station-keeping that are poised to mature conventional telescopes (see e.g. *The Future of Space Astronomy will Be Built*, a NASA-led contribution to the Astro2020 decadal survey [62]).

To this end, we introduce the *textile telescope* as a novel and mechanically robust medium for constructing dust telescopes. Significant increases in the physical scale of the detector aperture will in-turn increase field-of-view and count statistics. Fiber sensors, nonwoven fabrics, mesh structures, and fiber-reinforced thin-films all factor into this soft, stow-and-deploy capable design. The current work focuses predominantly on sensing dust kinematics/trajectories. In one conceptual sketch (Figure 1-2, center) a charge-sensitive meshed orb is spin deployed from a host satellite. When paired with an internal vibration and charge sensitive textile substrate, velocity, q/m, and trajectory can each be estimated. In sum, we aim to bring the rich work of the last decade in electronic textile innovation, disproportionately sequestered to applications in medicine, human-computer interaction, and military/consumer wearables, to an aerospace context.

1.2.2. Enhanced Spacecraft Thermal Blanket and Spacesuit

The textile has an additional crucial benefit, which is central to the current work. For decades, spacecraft and spacesuits have leveraged textile substrates as their outermost protective skins (Figure 1-3). For example, the exterior multilayer insulation (MLI) of the International Space Station is composed of Teflon-coated fiberglass ('Beta Cloth') which is robust to atomic oxygen erosion and designed for combined strength, durability, and flame retardation. Similarly, the outermost skin of a spacesuit is frequently composed of a Nomex, Gore-Tex, and Kevlar blend ('Ortho-fabric'), which balances flexibility with resilience. Though these two representative protective materials benefit from decades of flight heritage, they remain notably passive, despite offering key

Figure 1-3: Bigelow inflatable habitat on International Space Station, a clear display of Beta cloth fabric as exterior skin (Reprinted from [52]).

large-area real-estate on the spacecraft for active sensing and actuation during long duration missions.

Fabric, which is two-axis conformable, is a robust alternative to thin-films for protecting spacecraft. We seek to integrate large area fabric dust sensors directly into this MLI, an approach that is more deeply motivated in the next chapter. This work is conducted alongside JAXA's CLOTH, our sister project, which embeds thin film PVDF within MLI [16]. This multifunctional design approach affords an added structural health monitoring opportunity for the host satellite. Alongside the CLOTH team, we believe that explicitly bridging space science infrastructure into humanistic infrastructure represents a crucial practical approach to conducting space science.

1.2.3. A call to action: Extreme Environment Textiles

Ultimately, deep space exploration is only one avenue in our quest for fundamental knowledge. Humanity's instinctive will to explore draws modern civilization towards evermore extreme environments, sustained by a hunger for radical and direct sensory experience, as well as a conviction to comprehend the fundamental nature of things on Earth and beyond. Alas, until it

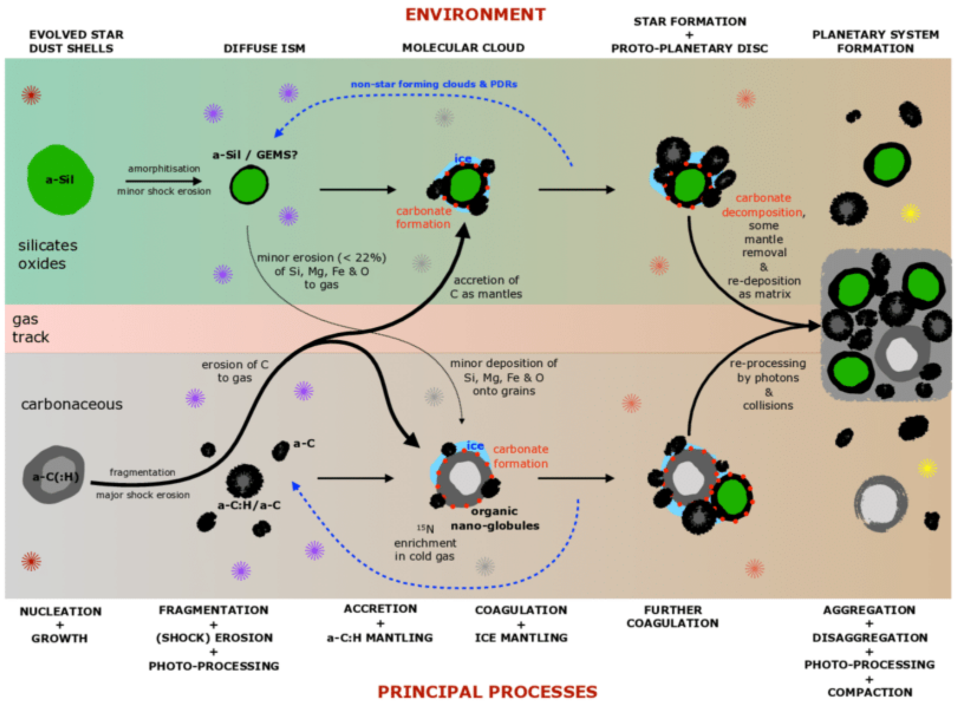

Figure 1-4: Lifecycle of dust in the interstellar medium (Reprinted from [35]).

is possible to substantially alter the human body, the humble textile will continue to serve as a boundary - a second skin - for the arctic explorer, for the deep-sea diver, and indeed for the astronaut. The textile will also continue to operate as core foundational infrastructure - the likes of tethers, ropes, nets, and habitat skins - that enable and sustain our journeys. Let us bring life to this skin !

1.3 . Cosmic Dust: Nature's Closed-Loop Recycling

We begin by reviewing in scientific terms the closed-loop lifecycle of dust in the cosmos, which is also depicted in Figure 1-4. From there, we will return to motivating the current work through a design and engineering lens.

'Cosmic dust' typically refers to particles in the nm to 100μm size regime that permeate interplanetary, interstellar, and intergalactic space. The fusion of dust and heavy elements requires cool, dense gas formed inside stars in the Milky Way. Condensed grains, composed predominantly of carbonaceous

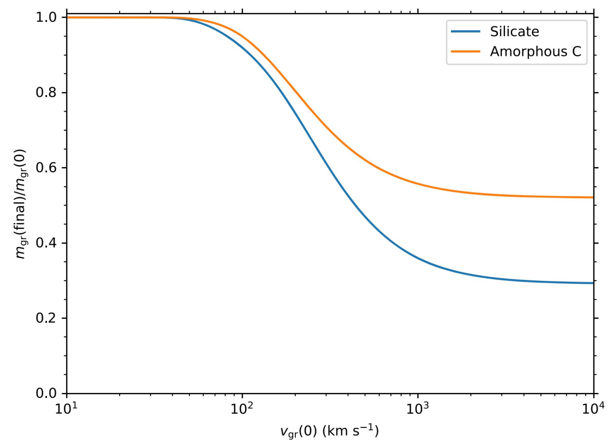

Figure 1-5: Final surviving grain mass fraction as a function of initial grain speed relative to the gas (Reprinted from [63]).

and amorphous silicates, are slowly ejected until the end of the star's life, at which point a stellar nova or supernova explosion ejects copious matter at speed estimates estimated from 10 km/s to 0.03c (see Figure 2 in [63], which is reprinted here as Figure 1-5) or 100-1000km/s (see Table 2 in [4]).

Supernova core collapse events are ubiquitous and common at intergalactic scales, with a star exploding every second somewhere in the universe and producing copious amounts of dust on the order of a fraction of a solar mass in the process. (The occurrence of supernova explosions within 1000 parsecs of Earth is estimated every few hundred years.) In this initial explosion, grains below 0.05 microns are destroyed by sputtering, grains between 0.05 and 0.2 microns are trapped behind a forward shock wave, and grains > 0.2 microns diameter overpower any gas drag, embed in the plasma ejecta and escape into the interstellar medium (ISM).

In the interstellar medium, these grains are on the one hand subject to growth via accretion of atoms and molecules. With regard to metallic nucleation, for instance, more than 65% of iron is ejected into the ISM in gaseous form, and believed in more recent work to then precipitate via cold accretion onto the carbon and silicate grains [23]. On the other hand, these grains are simultaneously subject to disintegration from incident high energy photons or cosmic rays, as well as shock-heated gas and sputtering. In sum, these growth and

Figure 1-6: Artist Tomas Saraceno prints cosmic dust from a 1982 NASA catalog using sequestered air pollution as ink. Closed loop recycling via cosmic dust lies in sharp contrast to the dust produced in man-made ecosystems (Reprinted from [60]).

disintegration mechanisms tend to restrict interstellar grains to a size regime from 10nm to 500nm, or at most single digit μm. Further, these physical effects constrain the lifetime of this dust. According to certain models, grain material traveling in excess of 220km/s is sputtered by supernova remnant (SNR) blastwaves, limiting lifetimes of solid matter in the ISM to $4 \cdot 10^8$ years [22]. In terms of grain speeds relative to surrounding gas, sputtering threshold velocity is 20km/s [63].

In addition to accretion and disintegration mechanisms, traveling dust grains are subject to various forces that will influence their trajectories. For instance, in the diffuse ISM, the radiation field is anisotropic, and so radiation pressure induces drifting on the order of <1 km/s [69]. Then, once arriving in the vicinity of the solar system, the gravitational force of the sun, solar radiation pressure, and the Lorentz force induced by the interplanetary magnetic field (IMF) will typically shape the dust's trajectory.

Over time, this dust and gas is responsible for the formation of new stars in the galaxy, as well as the formation of planets, moons, and asteroids around these stars, each in turn generating more heavily processed interplanetary sources of dust. (Comets, meanwhile, are comprised of minimally processed matter

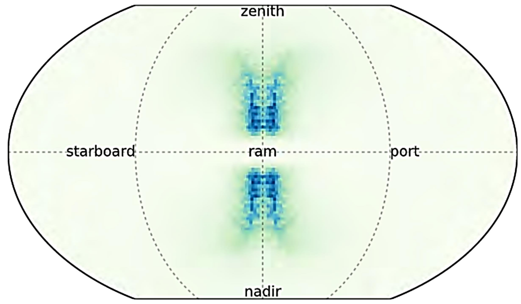

Figure 1-7: Example of anisotropic flux in the apex as estimated by NASA's MEM3 model. The directionality is plotted in a body-fixed frame, in which the center corresponds to the spacecraft's direction of motion (Reprinted from [50]).

from the birth of solar system). Hence, dust uniquely traces out the universe's grand astrophysical recycling pathways.

As an aside, the perpetual reuse of cosmic material via these closed-loop dust cycles lies in sharp contrast to the man-made dust and microplastic plaguing our local ecosystems. In commentary, Tomas Saraceno prints grains from a 1982 NASA Cosmic Dust catalog using PM2.5 pollution sequestered from the air of Mumbai, on display in 2022 at the Shed in New York City (Figure 1-6). This display was part of a magnificent experiential art experience on acoustic nets.

1.4 . Near Earth Supernova Explosions

Meanwhile, from the vantage point of our solar system, it is well known that the meteoroid flux is anisotropic (see e.g. Figure 1-7 for estimated apex anisotropic flux estimates from NASA's Micrometeoroid Engineering Model [50]). One source of excess interstellar dust might be the Local Interstellar Cloud (LIC), or 'Local Fluff' (maybe more accurately thought of as a void, as it about half the average density of the interstellar medium). The sun entered this cloud within the last 10,000 years, and is estimated to leave in less than 1900 years [42]. In 2019, a landmark discovery of radioisotope $_{60}$Fe in freshly deposited Antarctic snow from a near-Earth Supernova explosion establishes a possible link between these deposits and the current location of the Solar System within the LIC [38]. These fresh deposits complement ancient supernova signatures in Earth's fossil record that exceed expected background by a factor of 100, and signatures in lunar regolith that exceed background by a factor of 50 [8]. Together, the data provides evidence that dust survival over a minimum of many tens or hundreds of parsecs through the interstellar medium is plausible, and, remarkably, that dust from a near-Earth Supernova explosion is continuing to rain down on Earth.

Further, it has also been shown that particles with sufficiently low surface charging ($\ll$500 V) and sufficiently high velocities ($\gg$50km/s) will in fact be minimally deflected in the solar system (few AU for 50 km/s, undeflected at 100km/s), while particle velocities will be reduced only by a few % over a distance of 100 AU [4]. These estimates imply that dust from a near-Earth supernova explosion *does* in fact retain its ballistic trajectory. In sum, there is new evidence that some dust in our vicintiy specifically comes from a recent near-Earth Supernova explosion, and that this dust trajectory may be immune or only minimally influenced by local forces in the solar system. The Astro2020 decadal includes an urging by leading astrophysicists for more investment in Near Earth supernova detection [25].

1.5 . Dust Detection Mechanisms

1.5.1. Remote Sensing

Remote characterization is possible due to several physical mechanisms, well summarized in a quintessential paper by Draine in 2003 [21]. Foremost is the wavelength-dependent attenuation of starlight, either via scattering or via absorption at short wavelengths and reradiation in the infrared. This wavelength-dependence, a so-called extinction curve, is used to constrain the dust's size distribution. Most simply, Mie scattering (solution to Maxwell's equations at incident wavelength $\lambda \approx$ particle radius x) parametrizes the scattering radius as a function of wavelength as x $\frac{2\pi a}{\lambda}$. The spectral content is used for chemical identification - a 220nm bump indicates carbon, and 9.7μm & 18 μm features indicate silicate.

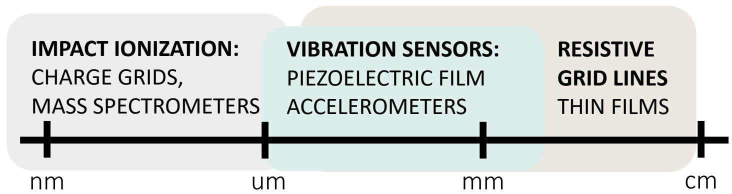

Figure 1-8: Predominant in-situ sensing method as a function of dust size

Grains in the Local Interstellar Cloud (LIC) are of strong interest as representative for the diffuse ISM. However, remote optical observations are hindered for studying interstellar dust grains in the LIC due to their low absorption (i.e. small optical depth, related to the extinction curve and treated essentially as the opacity of a medium). Further, so far as I can surmise from the literature, remote optical measurements cannot reliably be used for velocity estimates, which are instead modeled on the basis of Supernova and ISM properties. These limitations were motivations for the onset of in-situ measurement, beginning in the 1970's [3].

1.5.2. In-Situ Sensing

A variety of sensing techniques are used in in-situ dust detection (Figure 1-8). The two most common architectures are (1) PVDF thin films (See for example the 2014 ALADDIN Acoustic Detector incorporated into the Ikaros solar sail, [31]), and (2) charge grids and mass spectrometers assemblies that rely on impact ionization (see e.g. 2015 Hyperdust Chemical Sensor [66], and 1973 HELIOS Mass Spectrometer [20], among others.) On the pipeline is the Interstellar Dust Explorer (IDEX), part of NASA's IMAP mission [46]. At high ecliptic angles where it will fly, interstellar dust dominates. Finally, RF emission from impact plasma is also an increasingly plausible signature, particularly for impactors $\gg$8km/s. I have previously reviewed and summarized in technical detail this RF sensing approach in [11], also included in a later chapter.

As a proposed in-situ sensor, the current work fits within this context. Can fabric double as an enormous detector of interstellar grains, tiny messengers from cataclysmic events of scientific intrigue traveling at tens-to-hundreds of kilometers-per-second and originating hundreds of light years away? This work will justify instrumenting a robust fabric with sparse fiber sensors, building the case for ultra-large area sensing.

1.5.3. Dust Collection

Finally, a brief note that dust collection using Aerogel is also achievable, which has historically has allowed for the return of grains to Earth for further study.

CHAPTER 2

Astrophysics and Damage Sensing: A Bridge to Humanistic Infrastructure

Summary: *Whereas the previous section offered scientific context for the work, this section begins very broadly, and is written as an appeal to design-minded readers on the fluidity between scientific and humanistic infrastructure. Some context is also offered on the debris crisis in Low Earth Orbit (LEO). In practical language: (1) science experiments like large-area dust sensors benefit from piggybacking on critical spacecraft modules. (2) The dust/microparticle population in Low Earth Orbit poses a tangible threat to the safety of our space-based assets, which creates incentive to incorporate dust sensors into MLI. MLI-based sensors would ultimately track damage and initiate repair sequences.*

2.1 . Historical Context

Throughout the 17th-18th centuries, there was much greater fluidity between the natural philosopher and the lay person than is exhibited today. Even the most extravagant scientific equipment of the time could fit in a living room, and indeed, it was very common for western European makers of telescopes, microscopes, precision clocks, prisms and globes to sell gilded versions of such devices to rich patrons, much in the way that the grand piano continues to be a routine object of cultural and intellectual enrichment amongst the wealthy. The French *expérience*, with origins in the 17th century, aptly translates both as 'experiment' and as 'experience' into modern times [59].

'Scientist' was coined in 1834 by Cambridge University historian and philosopher of science William Whewell, and soon became a formal profession with an associated university degree. By 1850 there existed 40-foot telescopes, and microscopes of increasing operational complexity, and by 1950 there were nuclear reactors, particle accelerators, and other specially constructed scientific spaces. Thus, the infrastructure associated with frontier science outgrew the household drawing room, and scientific pursuit outside of the laboratory was relegated to amateur organizations, some of which exist into the present era. These amateur groups pre-stage today's scientific outreach programs, citizen science initiatives, and the well-established Do-It-Yourself (DIY) movement. Nowadays, it is also common for large scientific organizations to tout technology spinouts as a means to drum up funding. In particular, there are foundational and sometimes ubiquitous innovations derived from science and engineering laboratories, the likes of solar cells and CMOS imagers from NASA [3] and the World Wide Web from CERN [9].

Still, the fact remains that in any fixed moment in modern time, a divide now prevails between the infrastructure produced for frontier scientific investigation, and the infrastructure built in service of humanistic experience. This divide is driven by the increased complexity and scale of scientific infrastructure, though may not be as fundamental as it seems – certainly it was not nearly so immediate in the early days of scientifically minded pursuit.

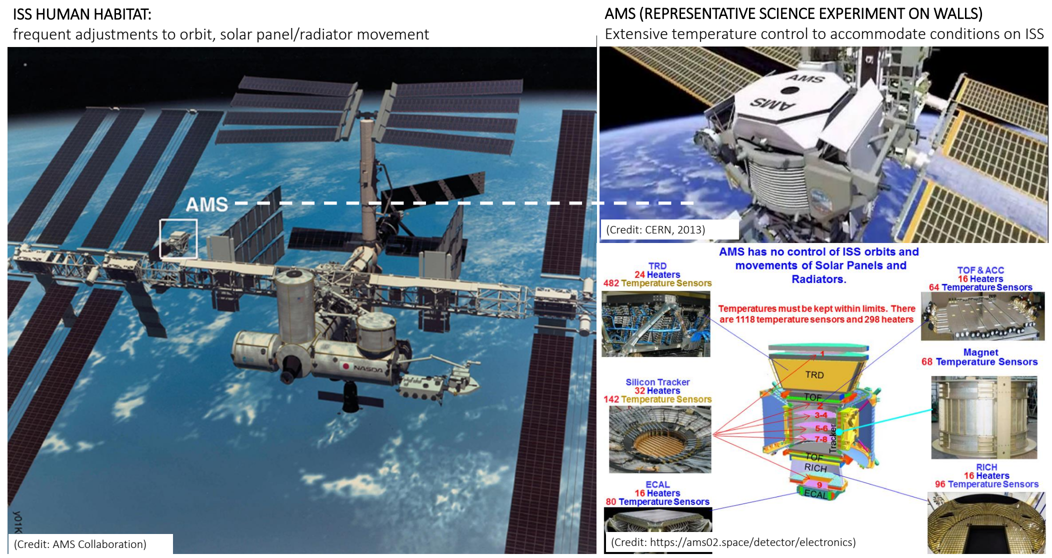

Figure 2-1: The Alpha Magnetic Spectrometer (AMS) is an example of a science experiment that balances the humanistic realities of living on a human habitat. From AMS website: 'AMS has no control of the ISS orbit nor movements of the ISS solar panels and radiators. In addition, the ISS attitude is changed frequently, for example, for the docking and undocking of visiting vehicles (Soyuz, Progress, SpaceX-Dragon, Northrup/Grumman-Cygnus, etc.). However [...] the temperatures must be kept within limits so that the detectors perform optimally, and so that no damage occurs to the detectors or the electronics. To achieve this [...] a substantial amount of electronics was installed to monitor the 1118 temperature sensors and control the 298 heaters' (Reprinted from [39]

).

2.2 . Cosmologist and Cosmopolitan on Orbit

Humanity now endeavors to establish a more significant presence in Low Earth Orbit and beyond. In this quest, the frontier explorer is sustained by a hunger for rich, thrilling, and immediate sensory experience of a cosmos filled with worlds that can be known and explored - NASA's famous *Visions of the Future* posters come to mind [37]. Meanwhile, the scientist is willed by a conviction to comprehend the fundamental nature of things on Earth and beyond. In Low Earth Orbit, the cosmologist and the cosmopolitan increasingly rub shoulders. Or, phrased in other terms, there is, increasingly, direct place-sharing between the specialized scientist and the lay explorer – a coexistence of scientific and humanistic pursuit that is evidently absent in the specialized laboratories of the 20th century. On the International Space Station, this place sharing is most immediate, though the boundaries still pronounced - one ends up with curious juxtapositions of astronauts playing with Nickelodeon's famous slime indoors [33], while the Alpha Magnetic Spectrometer (AMS, Figure 2-1) counts cosmic rays in search of dark matter on the spacecraft's opposing face [39].

Outside the station, scientific and humanistic infrastructure share the road, though generally from a distance. For instance, Iridium satellites operate alongside the Hubble Space Telescope in Low Earth Orbit - the one providing cellular phone connectivity, the other imaging deep into the cosmos - neighboring cars on a remote highway. When scientific and humanistic infrastructure are not gracefully coevolved, they clash. We are witnessing this clash as Elon Musk's Starlink network overtakes the clear skies essential to astronomers. Finally, there is also a third class of infrastructure – one that provides a broadly relevant resource that leverages the unique vantage point of space. Earth imagers like Landsat are a typical example, with evident use to scientists and laypersons alike [70].

Alas, only successfully deployed infrastructure is typically referenced. Often, a scientific mission proposal is not funded due to cost, or is deemed infeasible due to the required scale of deployment for conducting meaningful science. How might a more integrated and context-aware design approach to our space-based infrastructure work in service of both humanism and science in space? A key conceptual vision of the current work is to now propose that the secondary function of a multifunctional design need not relate directly to the primary mission. In a single substrate or system, opportunities exist to deeply unify the infrastructural demands and desires of the explorer with the architectures that enable scientific inquiry. In impressionistic terms – one can imaging riding a robotic spectrometer around an asteroid, visiting a distant telescope, or deploying an adaptive satellite swarm in e.g. a lunar elliptical orbit whose nodes capture images of Earth on one day, and operate as a deep space low frequency radio emissions the next.

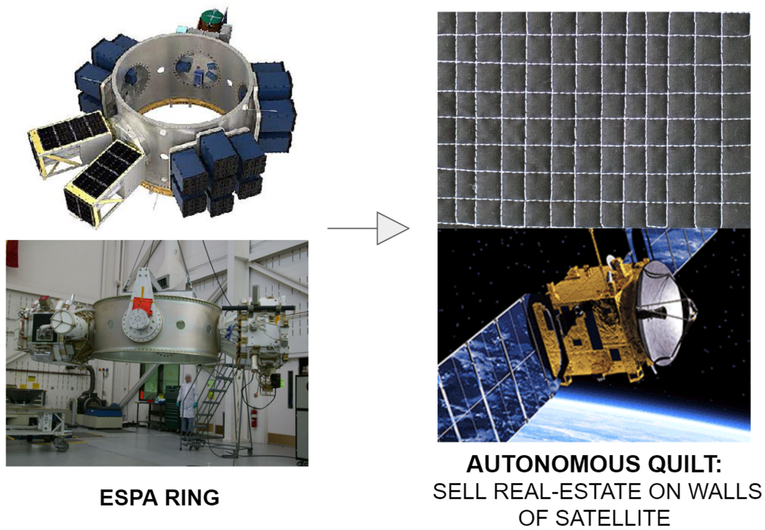

Figure 2-2: The EELV Secondary Payload Adapter (ESPA) is an adapter for launching secondary payloads on orbital launch vehicles.

Indeed, a very timely instantiation of this design paradigm comes from the Japanese startup ALE – in the coming years, artificial meteor showers will be used simultaneously as a source of entertainment and awe as well as a means to probe at the upper atmosphere [68], (see also vapor tracer technology [54]). It is not typically expected that the World Olympics would finance upper atmospheric studies. Yet, as a first customer of ALES' new service, their purchase will by consequence support this research.

Through widespread adoption of this multifunctional design paradigm, scientific experiments may increasingly 'piggy-back' on critical protective spacecraft submodules in a similar spirit to how e.g. today's CubeSats piggyback off of large spacecraft launches using secondary payload adapter (ESPA) rings - see Fig. 2.2. Massively distributed scientific measurements thereby become more realistic by way of higher technology adoption rates, with mass manufacturing increasingly an enabler for frontier science.

And, vice versa: humanistic considerations (notably the desire to visit remote spaces) may increasingly be prioritized when designing space-based scientific telescopes, rovers, and payloads, leveraging our intrinsic motivations for exploration as a means to promote private investment in scientific infrastructure.

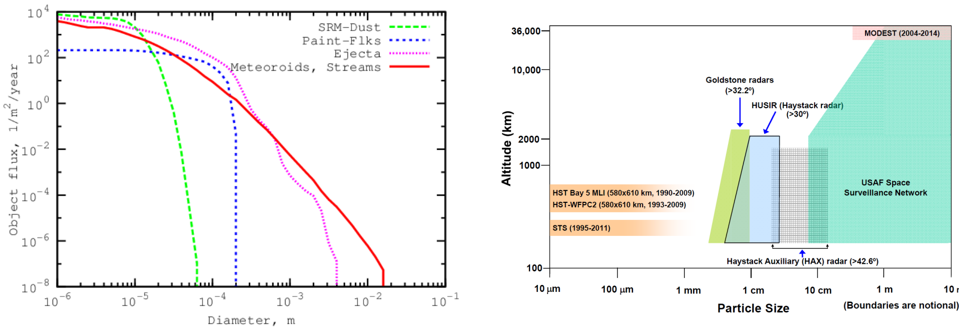

Figure 2-3: (Left) Dust flux in Low Earth Orbit incident on $1m^2$, estimated from European Space Agency's master model by size and material (reprinted from [2]). (Right) Tracking thresholds for radar technologies. The sub-cm debris population is probed by analyzing spacecraft parts returned to Earth reprinted from ([56]).

(I note that a recent major research effort in the Responsive Environment's Group – the "Tidmarsh" distributed sensing project, happens to promote a similar vision on Earth: a single sensing architecture servicing both scientific need and humanistic experience in a wetland restoration site [45]).

Scientific experiments do not tolerate haste or flourish – the design requirements governing each operating mode of a multifunctional system must be balanced early in the planning phase in order for each to be feasible. Figure 2-1 previously offered an example. While it is unlikely that such deep integration will be universally sensible, the current work seeks to identify a class of scenarios for which it is not only operationally logical but also scientifically preferable to pursue an integrated engineering approach. The spacecraft skin, owing to its large, space-exposed, and at present unused real-estate, will be the work's focus.

2.3. Space Dust and Manmade Debris in LEO

In this section, we briefly introduce a crisis in Low Earth Orbit that should provide clear incentive to aerospace engineers to adopt impact-sensitive MLI or similar technology, particularly as e.g. inflatable and soft-deployable structures become more commonplace in space. To achieve both scientific and safety objectives, benchmark dust sensitivity must be balanced on the basis of the

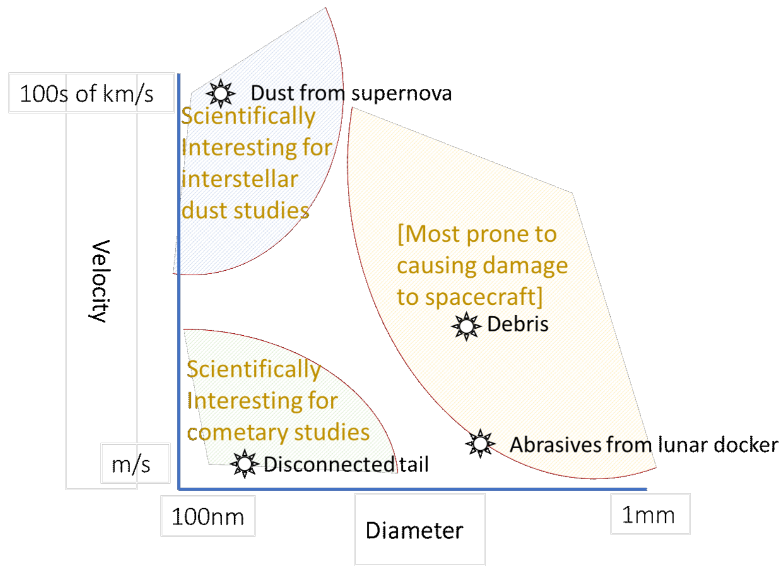

Figure 2-4: Semi-quantitative plot showing disparate speed and velocity regimes of interest based on detection objective

scale and velocity regimes of interest. See Figure 2-4 for a semi-quantitative comparison of dust kinematic regimes.

The number of objects on orbit around the Earth has grown significantly in recent decades, and it is of top priority to mitigate the risk to spacecraft posed by hypervelocity impact. For instance, Figure 2-3 (left) shows estimated dust flux by size and material. The risk these large objects pose to spacecraft can typically be managed, as they are within tracking thresholds of ground radar (Figure 2-3, right). On the other hand, smaller impactors below a few mm in diameter still may cause catastrophic damage, yet cannot be tracked, thereby posing a substantial threat. For example, a 1mm impactor can cause cratering up to 1 cm in diameter, enough to penetrate thin spacecraft walls and damage internal equipment [32]. Dust also poses risk on lunar and interplanetary missions. For example, abrasion caused by the dust ejected on NASA's Lunar Gateway following lunar lander redocking maneuver has been flagged by the team as a concern, and the recent impact event on the James Webb telescope's primary mirrors suggests an excess of dangerous micrometeoroids at the Lagrange points.

While there is significant engineering investment in impact-resilient material design, it is also important to quickly localize damage – particularly on life-supporting space habitats – in order to diagnose and initiate repair operations. As recently as 2018, NASA's live stream indicated that astronauts on the International Space Station relied on binoculars and zoom lenses to track down an air leak [53], rather than using a structural health monitoring technology. We see an opportunity for improvement!

CHAPTER

3

Research Contribution

Woven substrates have long served as protective agents against harsh environments on Earth, ranging from human-scale, thermally resilient fabric preventing firefighters from overheating [6] to kilometer-scale, high-stiffness geotextiles ensuring that land embankments remain stable [36]. The textile's mechanical flexibility, myriad achievable material properties, and ease of manufacturing at scale uniquely precondition it to certain feats of engineering.

Humanity now endeavors to establish a more significant presence in Low Earth Orbit and beyond. Broadly underpinning the work described here is a fresh avenue for inquiry: what unique experiences and modes of scientific data collection might be enabled by advancing the electrically passive aerospace-grade textile found on habitats, spacesuits, and spacecraft tethers into a *multifunctional, electroactive, and scalable sensate medium?*

In the previous two chapters, we have broadly introduced the scientific, humanistic, and design motivations for the current work: scientifically, we wish to measure cosmic dust kinematics (and eventually trajectory / composition) leveraging the material advantages of a textile sensor. In support of humanity's infrastructure in LEO, we wish to localize damage induced by high-speed dust

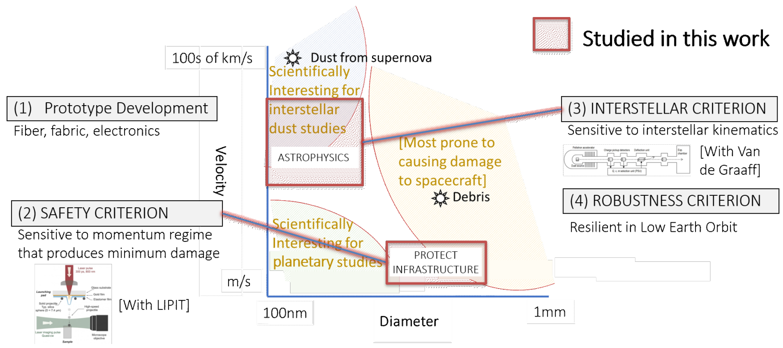

Figure 3-1: This work studies fabric sensitivity in momentum regimes relevant for infrastructure safety and interstellar dust sensing.

by enhancing MLI. From a design lens, we wish to achieve both of these objectives in a single system. And as a longer term scientific objective, we advocate for an ultra-soft and ultra-large, dedicated deep-space dust telescope. With this foundation, a still broader world will open up for augmenting space-based fabrics.

This brief section offers additional specificity on the research objectives and contributions of this work, and the organization of the remaining chapters. Hearkening back to the semi-quantitative map of dust kinematics, Figure 3 shows the two kinematic regimes that will be studied in this work, proving out this technology for astrophysics and infrastructure protection dual-use scenarios.

3.0.1. Summary of Key Questions

Main body of work:

[**Motivated previously in Chapter 1**] From a scientific perspective, can fabric double as an enormous detector of interstellar dust, tiny messengers from cataclysmic events of scientific intrigue traveling at tens-to-hundreds of kilometers-per-second and originating hundreds of light years away?

—> What are the mass and velocity regimes to which this fiber is sensitive? —> How does this sensitivity threshold compare to anticipated interstellar dust kinematics? —> How might fabric enable sensitivity to dust incident angle?

—> Can the fabric sensor system survive for at least one year in Low Earth Orbit? What are the primary degradation risks? Note that we anticipate around 100 interstellar particles per m^2 in LEO.

As future work, a dust telescope deployed outside the orbital plane of the solar system will see interstellar dust dominate. (In this case, environmental effects will differ: atomic oxygen erosion will be suppressed, and thermal cycling enhanced.) Only conditions in LEO were considered in this work, which is where the overwhelming majority of spacecraft are deployed today. .

[**Motivated previously in Chapter 2**] With regard to structural-health-monitoring, can a sensor-enhanced spacecraft skin also be used to localize damage on future space habitats induced by the tens-of-thousands of pieces of manmade orbital space debris and micrometeoroids too small to be tracked by ground radar?

—> What is the minimum distribution of sensitive fiber elements to allow localization of impactors to within a few cm?

Chapter 4 tracks the development of our baseline advanced fabric prototype, progressing from piezoelectric fiber sensors to space resilient fabrics to readout electronics.

Chapter 5 verifies the 'safety' (minimum damage sensitivity) criterion in Figure 3, and shows that piezoelectric fibers sparsely weft inserted at 1cm spacing can detect impact signatures associated with the most minute damage (breakage of a few filaments).

Chapter 6 verifies the 'interstellar criterion' in Figure 3, introducing an enhanced goldized Beta fabric and conductive pile fabric (fur) for achieving sensitivity to interstellar dust. The piezoelectric fibers are shown to transition likely acoustic to likely electromagnetic responsivity around the 2km/s speed regime.

Chapter 7 verifies the 'robustness criterion' in Figure 3, verifying sustained performance of the thermally drawn piezoelectric fiber following 14.5 months in Low Earth Orbit, and justifying the future addition of a white silicone-based thermal coating to minimize buckling effects.

Chapter 8 shares preparatory work to further validate the 'robustness criterion' by deploying an electrically active sample in space. This chapter takes us from sample design to initial 30-min in space power-up, in which very basic telemetry data is received from LEO.

Chapter 9 synthesizes and concludes the main body of work

Chapter 10 asks: what is the landscape of opportunity for advanced fabrics in space? I close with an extended chapter advocating for the future of advanced textiles in space. For instance, as a curious extension to the main body of work, what if astronauts could feel touch and texture right through their pressurized spacesuits? Can nets serve as foundational infrastructure on asteroids?

Appendices show some additional studies on PVDF yarn poling, validation of fur, additional microscopy searching for dust candidates on fabric, and some additional impact data from ground facilities.

The remainder of this dissertation anchors around dual-use multi-layer insulation (MLI) while also keeping a steady eye on longer term vision of a textile-based multi-use fabric system, with applications that include acoustic sensing, impact-induced plasma sensing, and perhaps eventually other parameters relevant to space habitats like optical detection of impact flash or gas-leak pressure sensing. By combining acoustic and electromagnetic signals into a single system, we will be able to, generally speaking, further validate and discriminate between effects at play in the space environment.

CHAPTER

4

Design of Space Fabric System

4.1 . Principal of Piezoelectricity

Piezoelectric materials demonstrate electromechanical coupling due to noncentrosymetric crystalline structures in e.g. quartz or due to beta-phase dipole alignment in semi-crystalline polymers.

PVDF behaves as a ferroelectric below the Curie temperature of 195°C. The hysteresis curve that defines phase changes for PVDF is well characterized and defined by Equation 4.1 [7, 19].

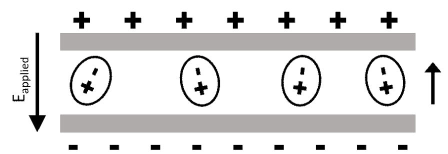

Figure 4-1: Electric field applied to align dipoles

$$\frac{dF_p}{dt} = \alpha(T - T_c)P + bP^3 + cP^5 = E. \tag{4.1}$$

This expression is derived by Taylor expanding the Gibbs free energy expression with polarization as an order parameter, minimizing free energy at thermal equilibrium, and applying work term **EP** - derived from Maxwell's equations - for the external electric field. To induce permanent alignment of dipoles, a voltage above the coercive field strength, as approximated using Equation 4.1, must be applied at elevated temperature. The coercive field strength of PVDF ranges from 50 MV/m to 90 MV/m in the literature.

On the one hand, PVDF fibers tend to have sufficiently high crystalline beta phase concentration for performance as sensors, as the linear stress in their manufacturing tends to yield preferential beta alignment. See for instance my FTIR and XRD measurements for bare PVDF fiber in an appendix and in [11]. However, poling is a bottleneck. The application of the previously cited coercive field to an inherently porous fabric or fiber array is limited by the dielectric breakdown strength of the medium. For many months, I experimented with poling bare PVDF fiber in dielectric greases and oils, and also with poling piezoelectric ink screen-printed on fabric. Results were inconclusive.

Conversely, the breakdown strength of PVDF is approximately 770 MV/m. Thus, the poling of nonporous thin films is more readily achieved. Therefore, multimaterial fiber drawing (with the active PVDF layer essentially as a thin film internal layer) is the most sensible manufacturing approach.

4.2 . Piezoelectric Sensor Design

Commercially available piezoelectric geometries are flexible thin films and bulky cabling. Piezoelectric materials are also available as more rigid/brittle ceramic discs, cubes and fibers. More recently, inks and 3D printing filaments have also come to market, though are unproven (I saw only inconclusive evidence of performance from the ink trialed).

Thin, flexible piezoelectric multilayer fibers have also been developed over the last $\sim$10 years in chemistry and materials science laboratories using a variety of precision multimaterial fiber extrusion techniques [24, 40, 30, 55].

Bearing in mind the state of this technology, we ultimately took two approaches.

4.2.1. Thermally Drawn Fiber

First, we partnered with the Fibers@MIT group to leverage their new thermally drawn piezoelectric nanocomposite fiber, abbreviated as TDF, and summarized in Figure 4-2. This fiber contains an active PVDF-TrFE layer with dispersed barium titanate nanoparticles, achieving a peak d_{31} piezoelectric coefficient in the range of 40-50 pC/N. Fiber design is summarized in Figure 4-2. I supported acoustic performance measurements and poling strategies (publication available at [72]). This fiber gradually become a priority in the work as our collaboration tightened, and so some measurements in this thesis are only presented for this fiber design.

4.2.2. Modified Piezoelectric Cable

In an effort to broaden access to this versatile fiber sensor across a wider range of disciplines and research institutes (human computer interaction laboratories, advanced concept prototyping teams, etc), fellow RA Joao Wilbert and I discovered a simple method for modifying commercial piezoelectric cabling for reduced bulk and improved compatibility with conventional textile weft insertion techniques. As depicted in Figure 4.2.2, the outer rubber shielding and outer copper braiding are removed using precision wire strippers, leaving an inner copper wire core and poled PVDF-TrFE cladding. The PVDF-TrFE cladding is subsequently coated in conductive elastomeric ink CI-1036 from Engineered Conductive Materials (EMS) and cured on a hotplate for 12 hours at no more than 90°C to form an outer conductor. The piezoelectric electromechanical coupling coefficient d_{33} remains unchanged (as confirmed using a quasi-stable Berlincourt d_{33} meter from PolyK Technologies).

This approach allows fibers of arbitrary lengths to be manufactured with a bend radius measured at roughly 3cm (improved from the bulk product) and d_{33} measured at roughly -33 pC/N, comparable with the bulk product. Some additional details and extensions to this method are described in our publication [14].

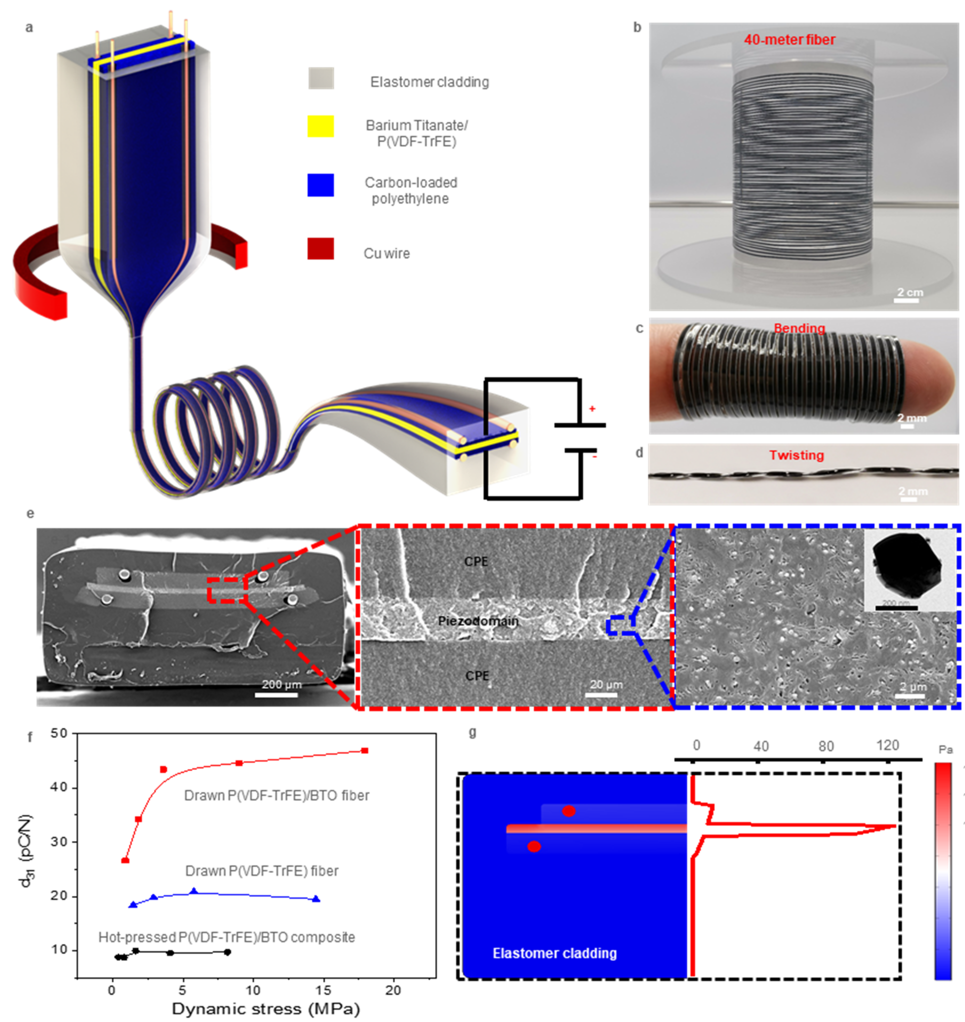

Figure 4-2: Design of Thermally Drawn Piezoelectric Fiber, spearheaded by Wei Yan in the Fibers@MIT group. Reprinted from [72], where I am a contributing author.

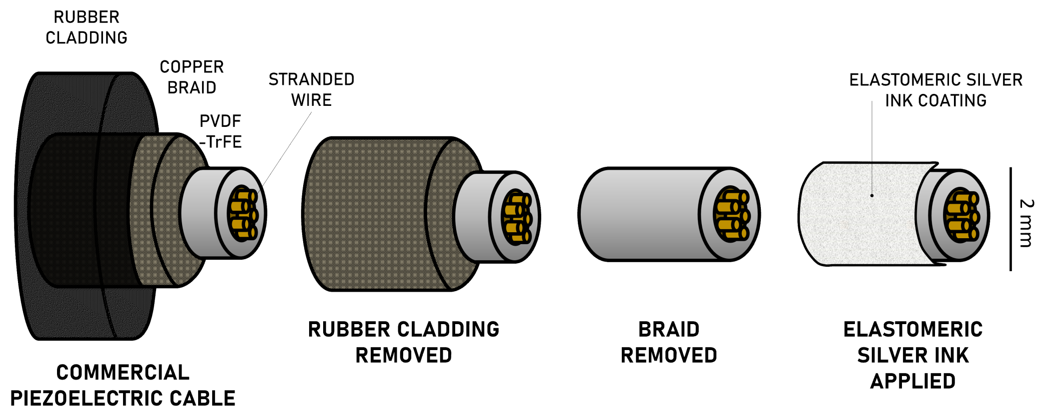

4.3 . Fabric Construction

4.3.1. Overview of Industry-Academic Partnerships

When augmenting specialized fabrics with sensory enhancements, industry partnership is a tremendous asset for access to specialized manfacturing knowledge and equipment for small-scale runs. I worked with JPS Composite Materials R&D to minimally adapt NASA-approved manufacturing specifications to accommodate our fiber sensors while remaining compatible with their available prototyping loom. Our work required significant technical discussion between academic and industrial R&D researchers. One of the prototype weave swatches sent to space was also contributed by Elizabeth Meiklejohn at Rhode Island School of Design. By working closely with industrial suppliers and textile engineers, our team was able to perform higher fidelity performance testing, baselining against heritage material.

4.3.2. Beta Cloth Specification vs. Commercial Counterpart

Beta cloth is a densely woven, Teflon-impregnated beta ('BC') fiberglass fabric used as an exposed shell layer on persistent space assets and spacesuits ranging from Apollo era spacesuits to Bigelow Aerospace next generation inflatable habitats. At 4.3 micron diameter, BC filament yarn produces the most flexible commercially available fiber bundle, and the resulting fabric is

Figure 4-3: Gallery of fabric prototypes. Swatches on the bottom are: (1) Commercial Beta Cloth (2) Beta cloth simulant with conductive yarn inserted (3)Teflon impregnated Beta cloth simulant with spacer yarn (4) Teflon Coated Beta Cloth simulant with weft-inserted thermally drawn fiber (5) Teflon Coated Beta Cloth simulant with weft-inserted coated cable

notable for its resilience to atomic oxygen erosion and other aspects of the harsh space environment (for instance, extended particle/UV radiation and thermal cycling). Its high weave density protects underlying multilayer insulation coatings from erosion. Most importantly, this material has decades of flight heritage. In order to enhance Beta cloth fabric, we first obtained small samples of this densely woven, Teflon-impregnated fiberglass material from Dunmore Aerospace.

In initial prototypes, thin film sensors were laminated or epoxied onto the fabric backing. Following a series of experiments in which sufficient sensitivity to ballistic stimuli was confirmed, we were ready to directly weft-insert fiber sensors into this material. Several prototypes are shown in Figure 4-3.

However, one key limitation arose in the manufacturing process. Commercial Beta cloth (Figure 4-3, (1)) is typically woven into a tight mat and impregnated in Teflon, which increases the durability and tear resistance of the fabric. A surfactant is added to improve Teflon adhesion, which is subsequently removed during a heat treatment process. Because this heat treatment is likely to depole or otherwise damage piezoelectric fibers, we pivoted in our principal prototype to sourcing BC fiberglass yarn pre-coated with Teflon from W.F. Lake, forgo Teflon impregnation, and thereby directly weft-insert the sensors during the manufacturing process without any heat treatment required. The resulting fabric (Figure 4-3, top right) is more porous than an impregnated counterpart, and the yarn denier is increased (a requirement for good adhesion of coating to a yarn). In exchange, the precoated beta fibers do not need further treatment for loom compatibility and are thus a higher quality product.

For completeness, a secondary prototype with traditional Teflon impregnation and heat treatment was completed, which also contains removable spacer yarns weft-inserted into the textile, allowing sensors to be inserted manually (Figure 4-3, #3). This manufacturing procedure more closely emulates NASA's approved process, yet with the added complexity of hand-insertion of sensors. Because hand insertion is not scalable, we focus primarily on evaluating our primary prototype. Other sensor integration methods may also be feasible.

Sample	**Texture** (yarns/in)	**Thickness** (in)	**Weight** ($yards/lb^2$)	**Filament** (in)
Commercial Beta Cloth (NASA)	85 x 60	.008	.44	.00017
Teflon Coated Fiberglass Yarn	42 x 35	.01	.56	.0112
BC Yarn, Teflon Impreg., Heat Treated	85 x 60	.014	0.5	.005
Fiberglass + Silvered Vectran Hybrid .	42x40 .	0.01 .	0.7 .	.0112 (BC yarn) .0089 (Vectran)

Table 4.1: Comparison between key textile metrics for commercial Beta cloth vs. modified Beta cloth materials

Finally, a third prototype incorporates Liberator conductive yarn from Syscom Advanced Materials (Figure 4-3, #2) which I considered in this work for hypervelocity impact plasma charge measurements on habitats, capacitive touch detection on spacesuits, and general signal routing across future space-grade e-textiles. Ultimately, this yarn was used in the construction of plasma charge sensing fur, which is further introduced in a later chapter.

4.4. Development of Low Power Readout Electronics

In total, there were four revisions to the readout electronics used during ground testing. Additional detail on PCB rev.3 is shown in Figure 4-4. Subsequent active flight electronics are detailed in a later chapter.

Electronics revisions progressed from:

- V1: Protoboard (Early LIPIT testing with piezo thin film)
- V2: One channel amplifier (Ambient pressure LIPIT testing)
- V3.1/V3.2: Multichannel, low power design (Vacuum LIPIT testing)

These designs were then superseded by two flight board revisions, which included a fully redesigned digital domain plus additional sensing sophistication and are summarized in a later chapter. During these sequential revisions, I received mentorship from noble electronics experts (referenced in the acknowledgements section) who ultimately helped me to achieve near self-sufficiency in complex, 6-layer board designs.

Ultra low power design was of central importance during the PCB design phase, as I was building towards a potential in-space deployment opportunity

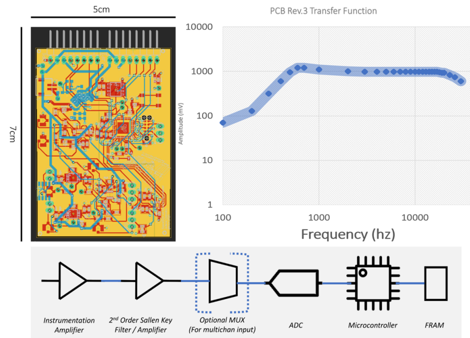

Originally designed to run off of coin cell for a year! => Ultra low power consumption prioritized

Key Power Specifications	Quiescent Current (µA)
INA333 Instrumentation amp	50
MIC861 operational amplifier	4.6
ADS7142 ADC	0.4 (900 nW/chan)
MSP430FR5969 MCU	100 (100 µA/MHz)
MB85RC1MT FRAM	15 (standby)

200µA / channel (active)
70µA / channel (sleep)

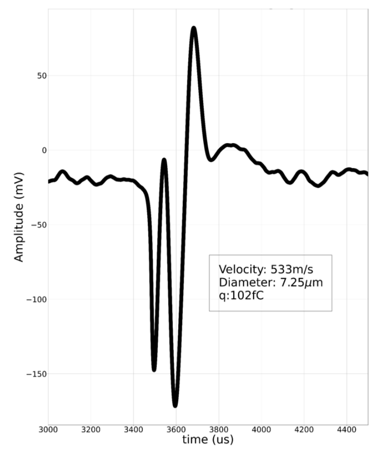

Key Board Specifications		
Expected signal duration	500	µS
Target sampling rate	240	kHz
Bandwidth	30	kHz
Min Resolvable frequency	500	Hz
Gain	100	

Figure 4-4: PCB Revision 3

Part #	Type	Vin range	Quiescent Current	Bandwidth @ 100x Gain	Common Mode Rejection Ratio
INA333	Instrumentation	1.8-5.5V	50 uA	3.5kHz	115dB
INA333-HT	Instrumentation	1.8-5.5V	50 uA (<135C) 198uA	3.5kHz	100dB
INA 2321 (wide temp)	Instrumentation	2.7-5.5V	40uA	5kHz	94dB
INA827	Instrumentation	3-36V	200uA	150kHz	104dB @>100x
AD8421	Instrumentation	5-36V	2.3mA	2MHz	134dB
MAX4208	Instrumentation	2.85-5.5V	750uA	7.5kHz	135dB
INA828	Instrumentation	4.5-36V	650uA	260kHz	140dB
AD8253	Instrumentation	5-15V (dual)	4.6mA	100kHz	120dB

Figure 4-5: Ultra low power instrumentation amplifiers considered

to be powered off of a coin cell battery for one year.[1] A secondary reason for prioritizing ultra low power design is to increase adoption rates of a future scaled space fabric system by demonstrating negligible burden on a spacecraft's resources.

This board design uses some of the lowest power consumption instrumentation amplifiers available commercially at the required bandwidth. Table 4-5 shows a comparison of parts considered. Analog amplifiers were selected primarily on the basis of high common-mode rejection ratio (CMRR) and ultra low quiescent current, with sufficiently low noise and at least 30kHz bandwidth at 10x gain. The INA333 instrumentation amplifier offers $\sqrt{\text{Hz}}$, 50μA quiescent current and 350 gain-bandwidth product. Low quiescent current was weighted more heavily as a consideration than CMRR & bandwidth, again due to the prospective coincell-powered launch opportunity.

In its final form, power consumption of this design at 2.2 volts line voltage and with independently operating channels (no multiplexing) is estimated at 200μA per channel in active state and 70μA per channel in sleep state. Therefore, based on calculations informing this low power design, one might expect, as a first order approximation, a current consumption on the order of tens to hundreds of mA for a system that is one day scaled to hundreds of sensor channels.

4.5 . Noise Analysis

Noise considerations are also crucial, as the noise floor will influence the sensitivity threshold of the system.

Output-referred noise will be dominated by contributions at the first op amp stage. A 10MOhm source resistance at the INA333 input weakly couples one side of the signal line to half supply. There are three contributions to noise in this implementation:

- Resistor noise voltage (Johnson noise)
- Amplifier noise voltage

[1] Instead, we were later awarded a fully powered deployment

- Amplifier noise current across source resistor

The resistor thermal noise voltage is calculated at 20°C to be around 70 $\mathbf{uV_{RMS}}$ using $V_{n(\mathrm{RMS})}=\sqrt{4K_BRT\cdot(F2-F1)}$ where K_B is the Boltzmann constant, T is temperature, and F2-F1 is the bandwidth (30kHz).

The INA333 noise voltage is 50 $\mathbf{uV}\sqrt{\mathrm{Hz}}$ RMS from amplifier voltage noise. Across 30KHz, the noise contribution is 8.65 $\mathbf{uV_{RMS}}$.

The INA333 current noise is quoted in Figure 8 of its datasheet at around $100\mathrm{fA_{RMS}}/\sqrt{\mathrm{Hz}}$. Across 10MOhm, this produces 1 $\mathbf{uV}_{\mathrm{RMS}}/\sqrt{\mathrm{Hz}}$. Across 30kHz bandwidth, noise contribution ís 173 $\mathbf{uV_{RMS}}$.

Treating these noise sources as uncorrelated, they will sum as $\sqrt{70\mu\mathrm{V}^2}+\sqrt{173\mu\mathrm{V}^2}+\sqrt{8.65\mu V^2}$ or $186\mu\mathrm{V_{RMS}}$ noise referred to input. At 100x gain, 18.6mV would be expected.

On the other hand, capacitance at the input, such as approximately 200pF in the case of the thermally drawn fiber, will form an RC filter that will reduce noise . There is also a possibility that input capacitance simultaneously contributes noise (see classic paper by Radeka - [58]), though this effect may be minimal for voltage mode amplifiers [65].

In a basic simulation prepared for the project, the input capacitance appeared to reduce noise to $233\mu\mathrm{V_{RMS}}$ referred to output, or 2.3mV intrinsic noise at 100x gain. Indeed, experimentally, $1.88\mathrm{mV_{RMS}}$ intrinsic noise is measured at the second stage using a digital oscilloscope with bandwidth limiting enabled. The sample is measured in an Earth-grounded vacuum chamber during this measurement. (Susceptibility to pickup, of course, is a different matter!)

CHAPTER

5

Sensing Impact-Induced Damage on Fabric

Although the current work has been contextualized in terms of hypervelocity / semi-relativistic interstellar dust, we should not lose sight of the potential value a large-area, stow-and-deploy type sensor might find in sonic/hypersonic speed regimes. A hypersonic tabletop accelerator (called the Laser Induced Particle Impact Test, or LIPIT) is reviewed in this chapter. The LIPIT facility includes a high speed camera for in depth study on impact dynamics, and is capable of accelerating 30μm-scale particles to ∼500m/s.

The most crucial observation of the momentum regime easily accessed by LIPIT is that it induces the minimum detectable damage on a Beta cloth fabric - breakage of a few filaments. Thus, sensitivity in this regime implies strong likelihood of sensitivity to /textitany damage inducing regime.

A an aside, the dust speed regime ≪1km/s is also very exciting from a planetary science perspective. For example, the dust/vapor plumes emanating from the oceans of Saturn's moon Enceladus follow a power law distribution maxed at ∼500m/s (for reference, this is $\approx 2{\cdot}v_{esc}$). Of course, these speeds apply only

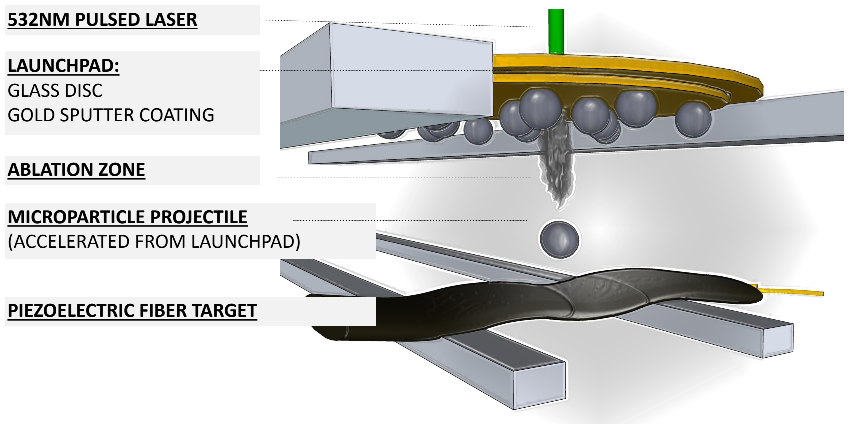

Figure 5-1: Render of Laser Induced Particle Impact Test (LIPIT), showing bare thermally drawn fiber as target

for stationary landers near a plume - flyby missions must additionally account for the spacecraft's velocity. With the right sensor suite, we might even find aquatic life on moons like this one [64].

In this chapter, we will present results for both the thermally drawn fiber and silver coated fiber. Operation of this facility was spearheaded by three of our expert collaborators: postdoc David Veysset, PhD student Yuchen Sun, and research staff Steve Kooi. By later testing campaigns, I became self-sufficient at operating LIPIT once the laser was appropriately aligned in the vacuum chamber.

5.1 . Impact Dynamics: Piezoelectric Fiber

Using high speed camera footage, the first study concentrates on building understanding for the mechanical dynamics of the impactor on both the thermally drawn fiber's SEBS elastomer cladding, and the coated cable's PVDF and silvered ink cladding. Three collision conditions can be distinguished - penetration, sticky, and recoil. These conditions are shown for thermally drawn fiber as a series of high speed camera images from three representative trials in Figure 5-3.

A bare fiber is placed in the LIPIT particle beam line under ambient condition, and 30 micron steel particles are accelerated towards this fiber target. The

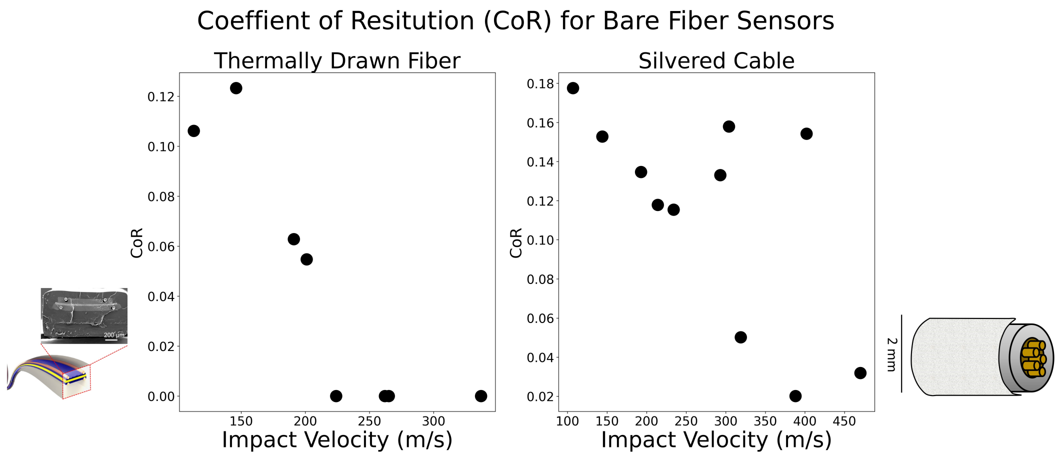

Figure 5-2: (Left) Coefficient of Restitution (CoR) for Thermally Drawn Fiber smoothly decreases. (Right) CoR for silvered cable bifurcates around 300m/s. Note that this data is taken with 30μm steel as impactor.

basic experiment setup is depicted as a render in Figure 5-1.

The coefficient of restitution (CoR), which measures input and output momenta for the recoil condition assuming conservation of energy and momentum in the system is defined as:

$$\mathrm{CoR} \ \frac{|\, V_{\mathrm{r}} \,|}{|\, V_{\mathrm{i}} \,|}$$

where V_r is the particle's recoil velocity and V_i is the particle's initial velocity.

Figure 5-2 plots coefficients of restitution as a function of impact speed. The thermally drawn fiber transitions smoothly from the recoil condition, sticky condition, and penetration conditions between 100m/s and 300 m/s. Further, the dynamics of impact(conveyed in Figure 5-3) are simple. SEBS compression on the order of 10μm is observed for the recoil condition. At higher speeds, the particle penetrates into the SEBS.

The same cannot be said for the coated cable! This sample only exhibits the recoil condition in the speed regime tested - it appears to transmit a growing percentage of energy to the fiber up to 250m/s, at which point the

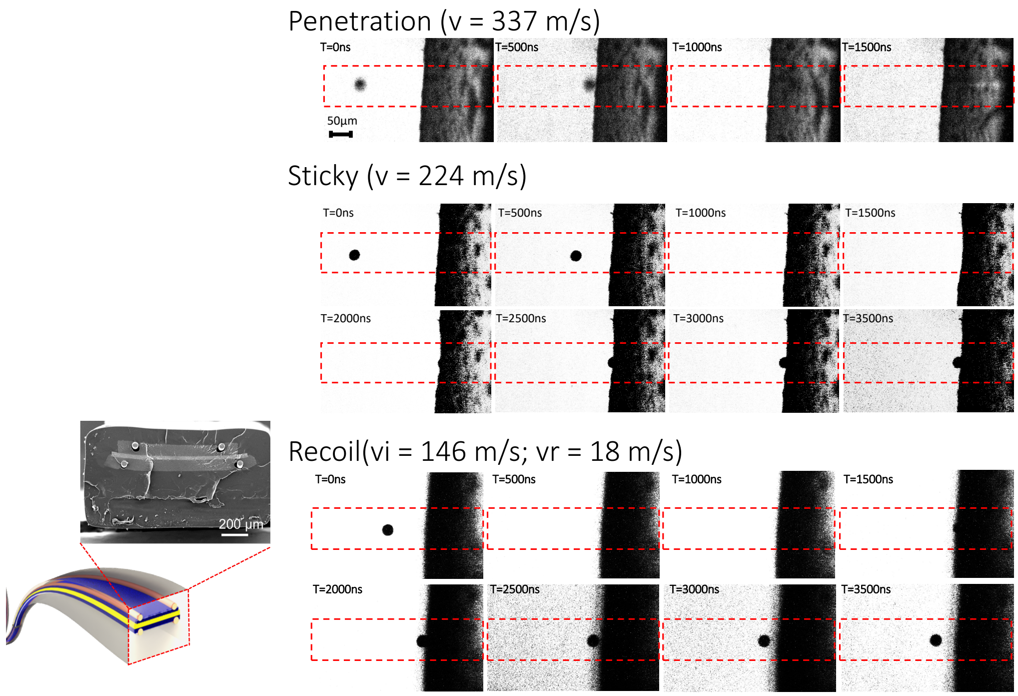

Figure 5-3: Penetration, sticky, and recoil conditions on TDF SEBS cladding

data bifurcates - in some trials, recoil speed continues to decline, while in others, an elastic collision is observed. What could be causing this different behavior at high speeds?

To address this question, we turn to the dynamics of impact on the silvered cable, which become quite interesting at speeds exceeding 300m/s. In certain trials that result in low coefficient of restitution, the particle partially adheres to the coating, then recoils, erodes some coating, and becomes tethered to the surface. After a few μs, the recoil momentum is sufficient to overcome this adhesion. The ‘tether’ of eroded material breaks, freeing and also torquing the recoiled particle. This behavior is shown as a series of stills in Figure 5-4. While the particle recoil speed increases after the tether breaks, these energetic processes assuredly reduce the recoil speed relative to other trials. While a curious phenomenon, in the context of sensor design, the simpler dynamics observed in the thermally drawn fiber are preferred in the interest of predictable dynamics.

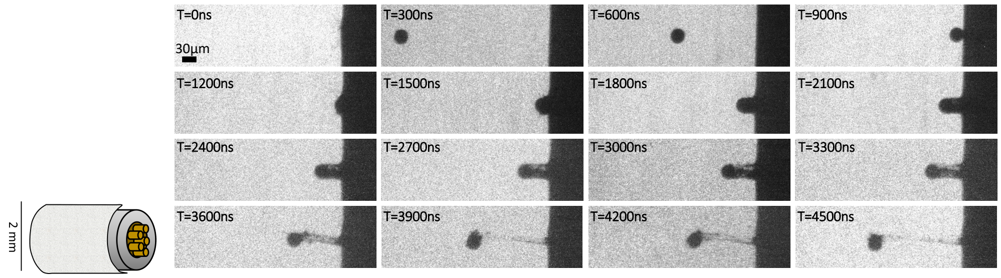

Figure 5-4: Exotic recoil/erosion event observed for silvered cable sensor.

Finally, a few dynamics trials were achieved at LIPIT's maximum capability - accelerating 7μm SiO2 particles to speeds exceeding 2km/s, (towards the lower boundary of the Van de Graaff's capabilities discussed in Chapter 6) In two trials on the thermally drawn fiber, the silica particle recoils at a sharp 45° angle, and in one case bits of debris are also ejected. A sharp recoil angle implies uneven absorption of energy at the impact site, possibly due to surface roughness (These trials are not pictured and are best reviewed as videos.) On the silvered cable, the same impact kinematics produce a cloud of eroded material, with debris speeds vastly exceeding the particle recoil speed (Figure 5-5). The damage site is on the order of 20μm in width, or 3x the diameter of the impactor. A debris cone signature is faintly visible in one frame at an angle of 40deg relative to the site of impact. Partial plasma formation is possible at these speeds, especially on this more rigid target.

For context, the iron used in the Van de Graaff (described in Chapter 6) is at minimum half the size and 3x the mass of this silica particle, but we are within the same order of magnitude to the lower limit of kinematics in the Van de Graaff, and here have had the advantage of characterizing the effects visually.

5.2 . Sensing on Piezoelectric Fiber

Having gained some understanding of the mechanical dynamics of impact at speeds in the regime of 100's of meters per second, the next task is to examine whether impact can be detected by piezoelectric material in the fiber. The likelihood of direct impact on fiber is determined by the sparsity of weft inser-

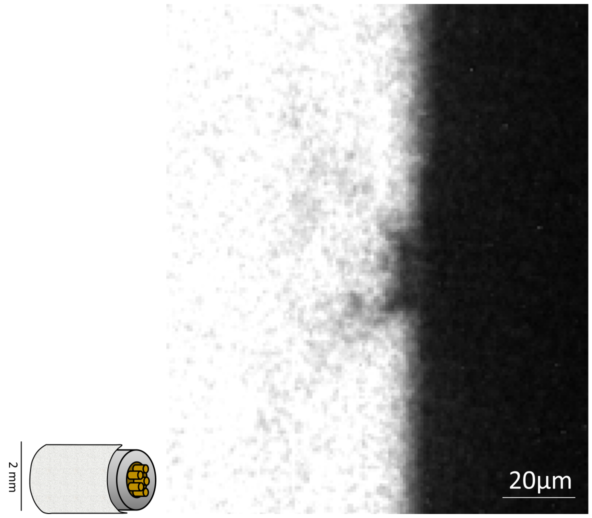

Figure 5-5: 7μm Silica incident on coated cable at 2980m/s under ambient condition produces conical debris plume. Angular ejecta is also visible for a thermally drawn fiber impact in this speed regime, though debris is sparser and best reviewed as video.

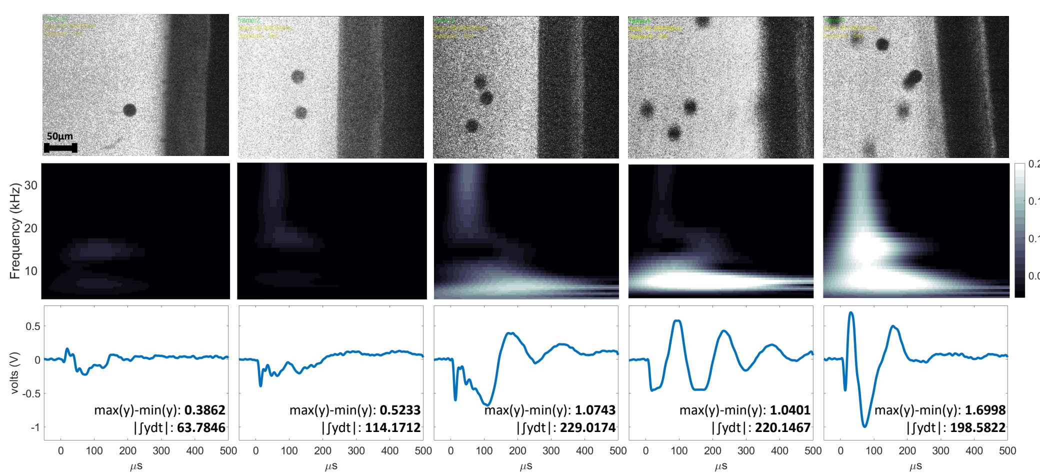

Figure 5-6: Changing only the location on the launchpad that the laser is focused, while holding all other parameters of the experiment steady, data appears to show correlation between particle count (ie/total mass) and signal amplitude. Note that there is a gain f 10x (f< 2kHz) and 5x (f> 2kHz) included in the data.

tion. Denser spacing yields grater impact sensitivity and higher channel count, coming at a likely cost of power and sampling frequency. At the 1cm weft spacing emphasized in this section, 2mm fiber sensors represent roughtly 20% of the total fabric area, with a corresponding likelihood of impact. Here, we study whether we are sensitive to, once again, the minimum damage criterion, corresponding to 300m/s impact speeds where we previously saw penetration of particles into the fiber's cladding.

Energy transmission is as: particle recoil, heat, friction, transverse mechanical waves, and longitudinal mechanical waves. The pressure waves propagating longitudinally through the fiber's cladding will strain the fiber's internal active layer.

At the time we began running tests at the LIPIT facility in late 2019, the thermally drawn fiber had only started showing any sensitivity one week prior. A sample was added to our testing schedule the day before testing was scheduled, and there was great delight to observe promising indication of its sensitivity! Under ambient condition, one way to build confidence in genuine impact signature is to fix all parameters of the experiment (laser energy/focus, fiber mounting) and adjust only the number of particles in a particle cluster onto which the laser is focused. With only this experimental parameter modified, all background signatures are expected to remain constant. Figure 5-6 shows high speed camera footage and corresponding piezoelectric fiber time domain signatures, and frequency domain signatures (via Wavelet transform) for 1, 2, 3, 4, and 7 particle conditions on the thermally drawn fiber. Data is sampled under ambient pressure at 2MHz. Peak-to-peak amplitude appears to scale with particle count, and resonances at around 5kHz and 15 kHz are apparent at higher masses.

The piezoelectric fiber is sensitive to impact !

We acknowledge some limitations: particle count estimate is estimated based on camera field-of-view (though out-of-focus particles will have proportionally less energy). There is slight clipping in the 4-particle case, but it is still shown for completeness. Finally, the wavelet transform is used to depict frequency content in Figure 5-6. In general, the wavelet transform offers improved time resolution at high frequencies at the expense of time resolution at low frequencies. However, this comes at the expense of risk of artifacts - the cone of influence (COI) constitutes a region in which the wavelet power spectra are distorted because of the influence of the end points of finite length signals.

5.3. Impact Dynamics on Film and Yarn

As sparse weft insertion of the sensors is anticipated (and therefore direct impact on fiber statistically suppressed), we now move swiftly to considering impact on material adjacent to the fiber sensor. This study progresses gradually from thin film to yarn to fabric.

5.3.1. Mylar Film

In order to better understand the dynamics of impact on fabric, we begin with a brief study of impact on 25 micron Mylar thin film. These test were conducted using 30 micron steel particles incident on 1mm x 25mm Mylar film, with the high speed camera focused along the x-z plane (taking the surface of the film to be the x-y plane). At 400m/s, these particles have an energy on the order of 9μJ, which appears to be very close to the penetration limit for the film. The film deforms to a maximum amplitude of roughly 30 microns (order of the particle size) over a 200ns period, before settling to rest after 1μs. The time averaged force applied by the impactor is thus estimated at 40mN, and estimating surface contact of 1/4 of the impactor's area, then the local pressure is estimated at 56mPa. The particles appear to crater into the film in this momentum regime, with further evidence for cratering in confocal imaging. Example of impact dynamics on film and cratering are shown in Figure 5-7. Some trials also show transverse wave propagation at least 300μm from the impact site.

For completeness, a further set of trials were conducted impacting the Mylar film with 7 micron silica in the 1.6km/s-2km/s speed regime (available by video). At 2km/s, these particles have on the order of 700 nJ of energy, an order of magnitude less than steel at 400m/s. Of 7 trials, 2 contained evidence

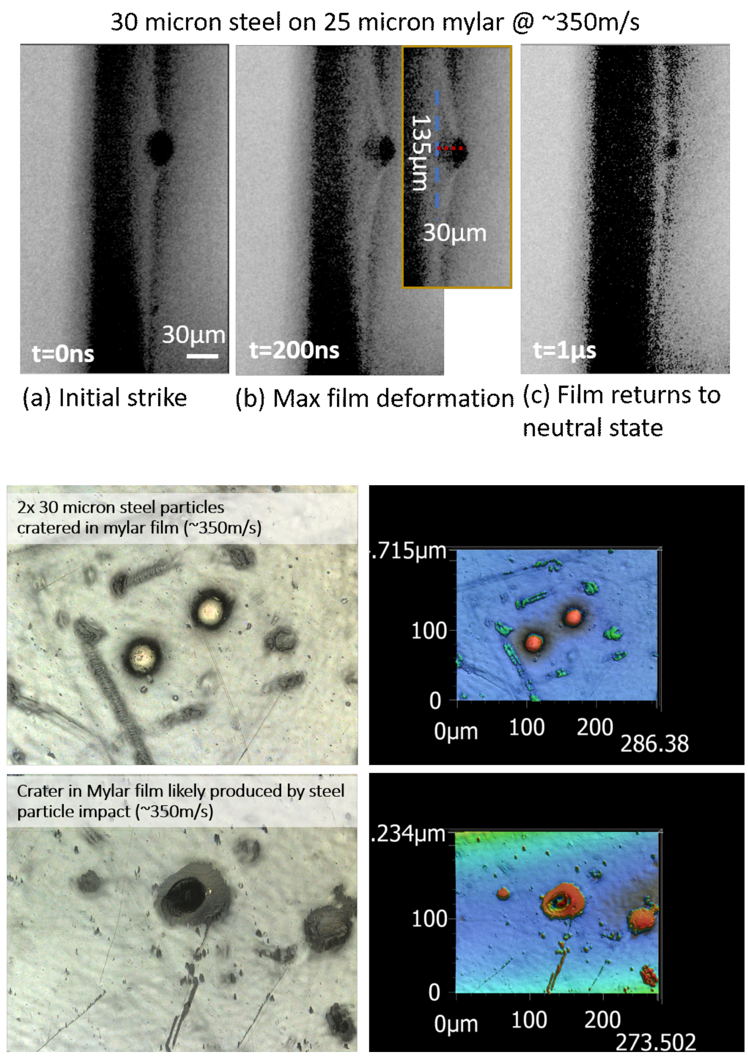

Figure 5-7: 25 μm Mylar thin film impact dyanmics and cratering

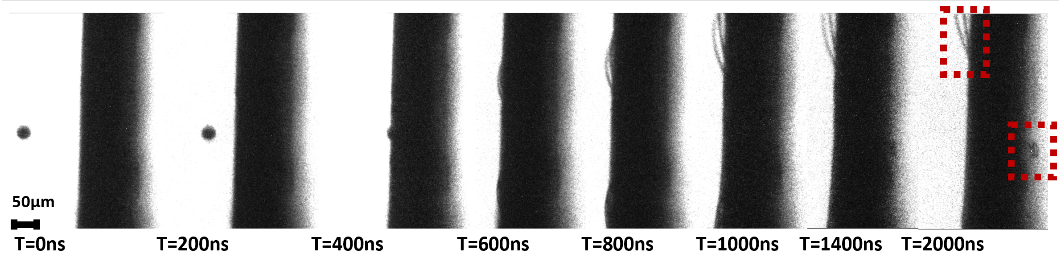

Figure 5-8: Wave propagation on Teflon coated yarn

of perforation in an after-image of the damage site.

In sum, large particles cause local deformation of the film (including cratering and transverse wave propagation) and small particles may cause perforation.

5.3.2. Yarn

Unlike in film, wave propagation on Teflon coated yarn is carried at least partially by individual filaments. The propagation speed of the wave can be coarsely measured. Taking one trial as an example, an interframe sampling time of 500ns and an estimated 145 micron propagation distance from the impact site, the surface wave speed is 290m/s, essentially equal to Vin. Following impact, the damage site is also visible as broken filaments (which have diameter 4.3 microns).

A subsequent series of 5 tests on Teflon coated yarn with emphasis on studying surface wave propagation time showed wave speeds ranging from 170-275m/s for impact velocities of 300-370m/s. The waves are consistently carried by individual filaments, and appear to quickly slow and spread following impact. In one particularly clear shot, shown in Figure 5-8, the wave is carried by two filaments, with amplitude growing to 30 microns and transverse damage also visible on the opposing face of the yarn.

At speeds above 325m/s, steel particles adhere to the Teflon coated yarn. The crater formed in three trials is shown in Figure 5-9 and suggest that cratering depth ranges from 10-20 μm. In two cases, individual breaks in filaments are also visible.

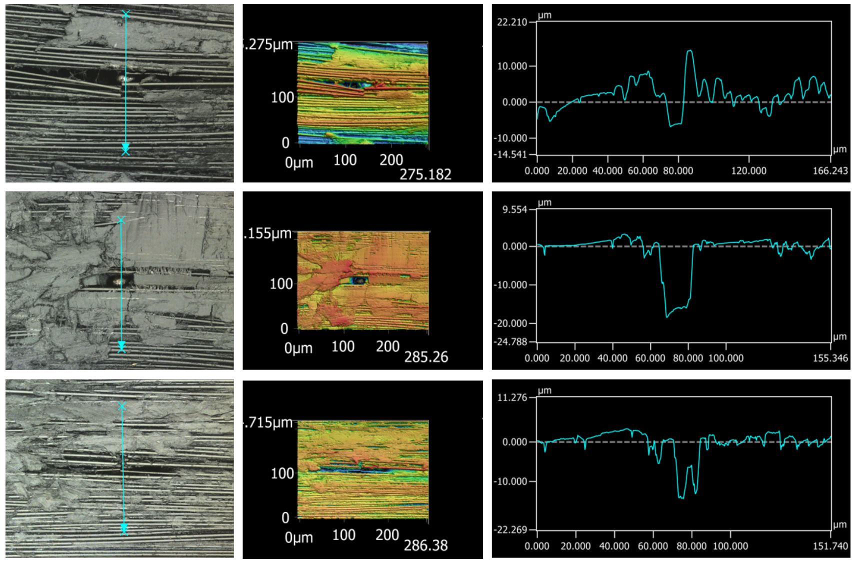

Figure 5-9: Craters formed on Teflon-coated yarn following impact by particles in the $\sim$ 325m/s regime

Finally, for 7.4 micron silica, there is no visible propagation wave or filament breakage. Over 9 trials for Teflon Impregnated fabric and 8 trials for Teflon coated fabric, the coefficient of restitution represented recoil velocities ranging from 4% to 25% of input energy (else a sticky collision), implying that between 75% and 96% is transferred to the target material in the recoil scenario.

The most crucial takeaway from this study is that in film and in yarn, we are seeing the transverse energy propagation that allows a piezoelectric fabric with sparsely weft-inserted sensing elements to function as a sensor. Second, we are directly observing hypersonic impact dynamics, which is not possible on a full fabric substrate due to transverse obfuscation of view, and is also not possible at the Van de Graaff accelerator facility.

5.4 . Sensing on Fabric

Fabric experiments were conducted in a vacuum chamber in order to minimize blast wave acoustic effects. By this stage of experimentation, fiber sensors had been professionally woven into beta fabric simulant. The fabric samples contain 4cm long active fiber sensor samples and are mounted at each of 4

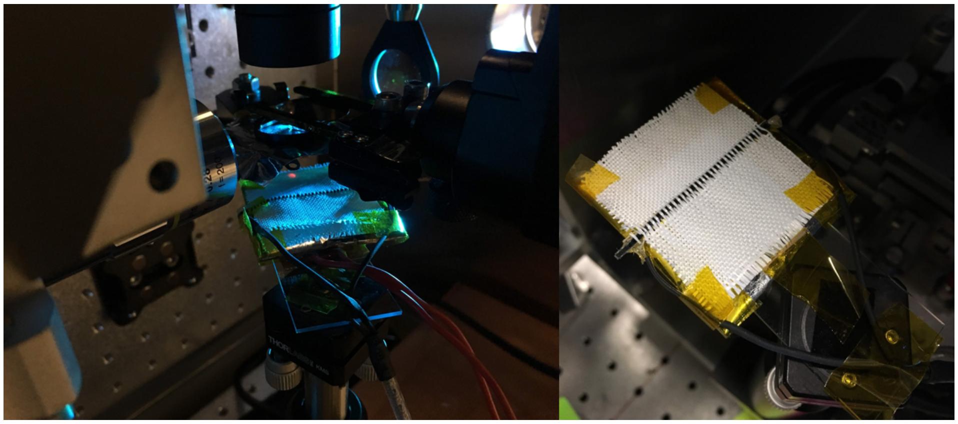

Figure 5-10: Fabric setup in LIPIT

corners onto a glass backing with Kapton tape and loaded into the test setup. Impact signatures were compared when striking directly on the active fiber vs. 1-2cm offset from the fiber. Experiment setup is shown in 5-10, and results are shown in Figure 5-11. Figure 5-12 additionally represents this information in terms of the estimated sensitivity of the fiber as a function of distance for the fixed steel impactor mass/size under consideration. **Taking a desired SNR of 5 for the minimum damage-inducing speed regime, we conclude that the fiber has sufficient sensitivity for detection of damage 1cm distance away**.

Figure 5-11, a key result, shows measurements from an experiment conducted with 4cm long thermally drawn fiber in Beta fabric. Integrated and peak-to-peak measures and lines of best fit are pictured for direct impact as well as impact offset by 1cm and 2cm from the sensor. On the basis of this plot, integrated and peak-to-peak voltage do correlate with steel impactor speed, as well as distance from sensor. Note that in units of $\frac{q}{m}$ (ie/ C/kg), this data corresponds to an estimated 10^{-3}C/kg (order of magnitude) when factoring in gain and capacitance.

Figure 5-13 additionally shows some data from an experimental configuration with multiple fibers, with data points all in speed regimes between 250m/s and 375m/s. Note that all impactors are within the approximate range of 250-375m/s, right at both our sensitivity and damage inducing thresholds. Indeed, we appear to see impact events showing single fiber and multifiber actuation,

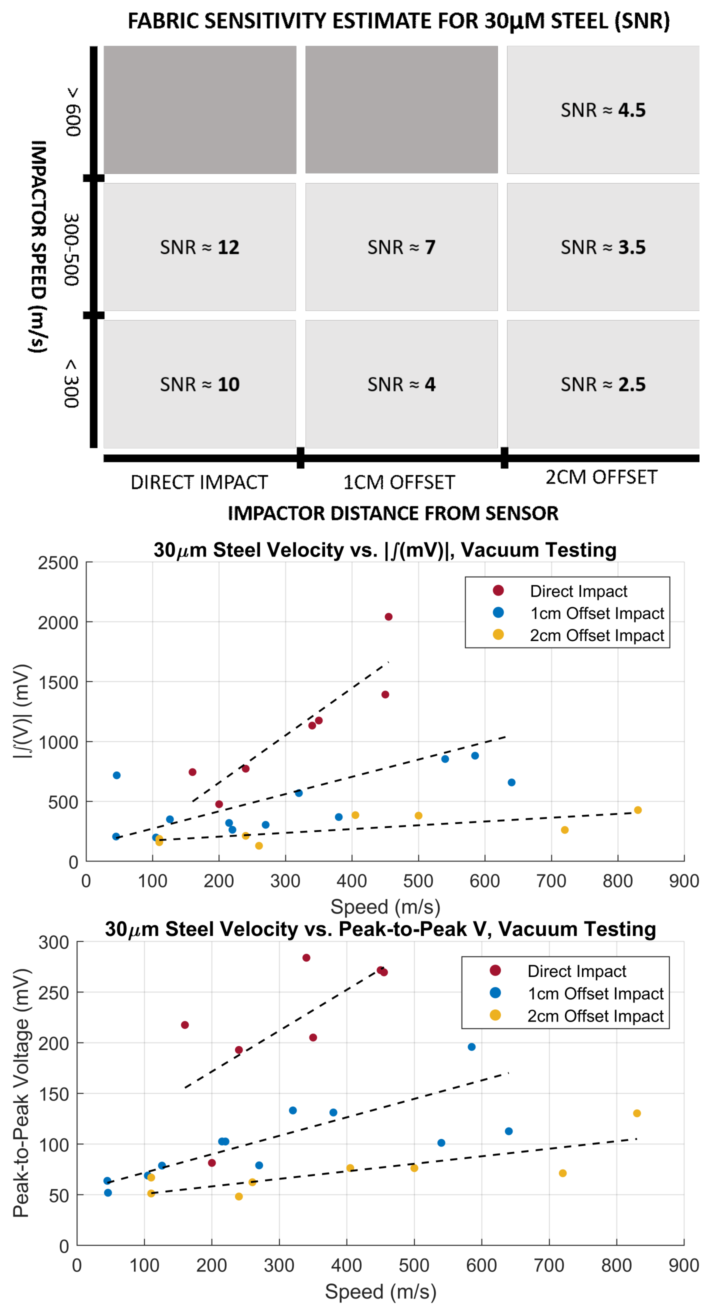

Figure 5-11: Chart showing estimated sensitivity of fiber to impactors at different speeds and distances from fiber, based on peak-to-peak (P2P) measurements. Output data (P2P and integrated) also shown.

Figure 5-12:

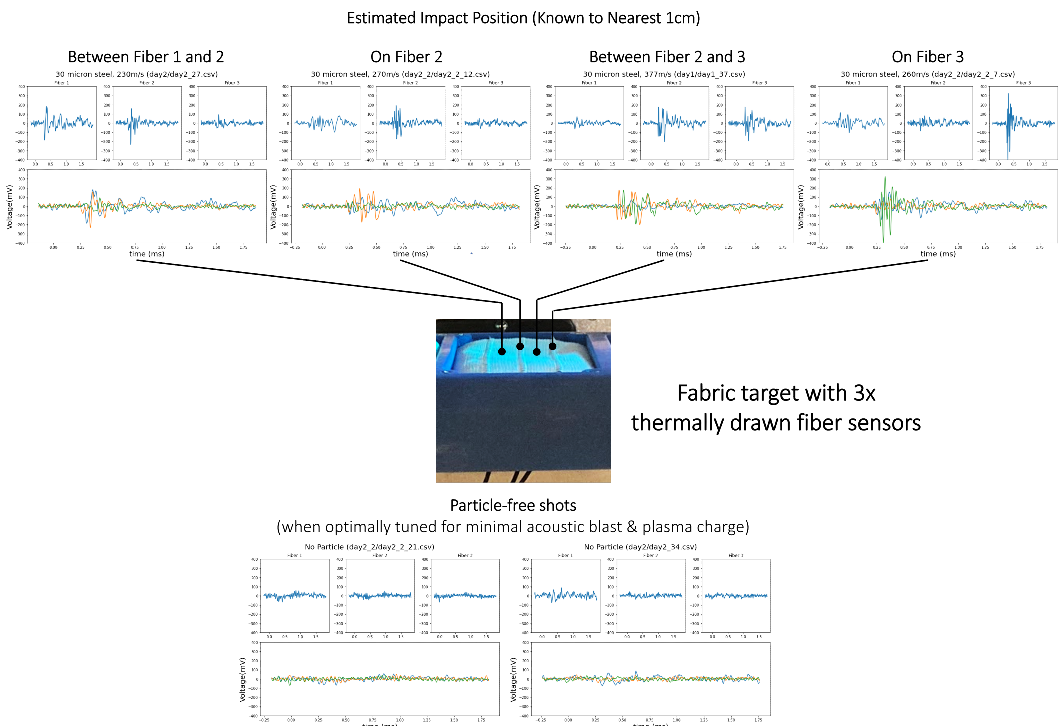

Figure 5-13: Chart showing representative data shown for multifiber configuration.

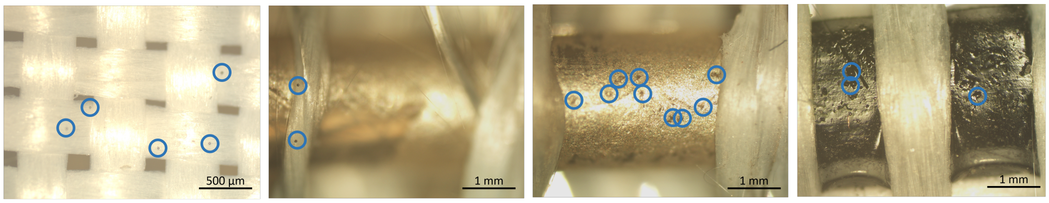

(a) Steel particles on Beta fabric surface approx. 5mm offset relative to sensor
(b) Steel particles on warp yarn securing sensor in fabric
(c) Craters on sensor - presumably artifacts of impactor recoil
(d) Thermally drawn fiber: particle embeds in SEBS

Figure 5-14: Inhomogeneities in impact site on fabric

as anticipated. Any timing deltas between signals are deemed unreliable at this close fiber spacing, and not used in the analysis.

There are several caveats to this data. First, the ground truth impact position is only known to the nearest 1cm due to variability in particle acceleration angle at the LIPIT facility, and due to the distance between launchpad and target. Therefore, an assumption is made based on relative impact signatures on the approximate likely impact location. Second, although clean background (ie/particle-free) signatures are shown, this result requires careful tuning of shielding, grounding, and in particular vacuum chamber pressure to reject both gold launchpad impact plasma (suppressed in air) as well as acoustic blast wave (suppressed in vacuum). There is continued risk that these two background sources remained an intermittent influence in our measurements. Third, owing to more than a year of technical malfunction of the LIPIT facility, only speeds in the range of 250m/s and 375m/s were accessible during our last opportunity to conduct this test. (The LIPIT facility has since been professionally repaired!)

Fabrics have inhomogeneities. From post-impact microscopy we observe some offset particles on warp/weft crossover points, vs. some on bare fiber. We observe some direct impact particles on weft fibers and others that actually strike the fiber's surface. This variability in surface characteristics can account for some of the data spread (Figure 5-14).

Some additional plots from LIPIT calibration are included in the appendix.

CHAPTER

6

Sensitivity of Fabric to Interstellar Dust Kinematics

To claim sensitivity to interstellar dust, the scale/mass regime $\ll 3\mu$m must be probed. In this chapter, we explain the current performance boundary of LIPIT, and briefly introduce the Van de Graaff dust accelerator, which remains state-of-the-art for accelerating particles with kinematics representative of interstellar dust. We then describe a series of experiments conducted to measure acoustic and charge signatures, including motivation for conductive pile fabric 'fur'.

6.1 . Current Performance Boundary of LIPIT

The LIPIT has a major advantage of being a tabletop-scale apparatus. This facility has only recently been considered for space dust impact studies, and it is the subject of significant research to improve its performance. For example, the recent introduction of a vacuum chamber minimizes blast wave shock acoustics.

In both vacuum and in air, the LIPIT facility's upper limit on imparted mo-

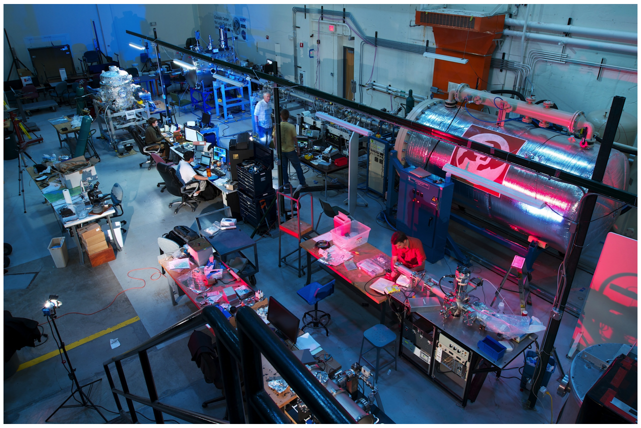

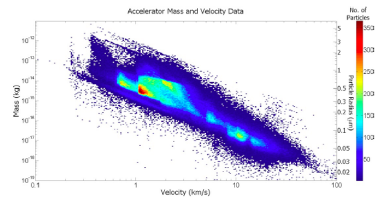

Figure 6-1: (Top) Image of LASP Van de Graaff accelerator. (Bottom) Distribution of dust kinematics (velocity, mass, radius) achievable at LASP Van de Graaff accelerator (Reprinted from [51]).

mentum is constrained firstly by the properties of the polymer layer on the launchpad. When this polymer layer is omitted, and with fine-tuning of the apparatus, the facility has been shown to accelerate particles in the 5μm regime up to 1-2 km/s, at which point the acceleration is limited by fracturing of the particle from the imparted energy. However, achieving these speeds in LIPIT is at present time-limited and complex - without the polymer layer, only a single shot can typically be taken per launchpad (as the impulse ejects all particles off the surface). Further, absent a polymer layer, additional debris ejecta must be shielded with a pinhole and foil. Meanwhile, the $\approx$5μm size regime limit is set by the resolution of the high speed camera, as it is at present the only means to determine a ground truth for the kinematics of individual particles.

6.2 . Overview: Van de Graaff Dust Accelerator

Van de Graaff acceleration remains our best tool for accessing the desired kinematic regimes. A warehouse-scale, modified 2MV Van de Graaff accelerator located at the Laboratory for Atmospheric and Space Physics (LASP) is briefly summarized, and is further described in [48]. Dust is loaded into a small $\sim$cm-scale cylindrical chamber with a needle suspended at the center. The needle is held at +20kV, and the walls are pulsed with high voltage. The

Figure 6-2: Overview graphic of three primary targets used in experiments.

particles tend to acquire a slight negative charge and are attracted to the needle. In a stochastic process, some particles touch the needle, rapidly acquire a positive charge, and are ejected at high speeds away from the needle. In a second acceleration stage, the particle then passes through a potential gradient. Charge and speed are measured with precision. The accelerator allows for down-selection on the basis of these kinematics using a high voltage pulse that can eject individual particles out of the beamline. Selected particles enter into an ultra-high vacuum chamber where experiment targets are mounted.

Figure 6-1 shows the distribution of particles launched in a generic run at this facility [51]. Speeds on the order of 50+ km/s are achievable for sub-micron particles up to a few μm in size. Note that detection of particles greater than $\sim$10km/s requires use of an FPGA-based trigger, which requires additional processing and event matching efforts by the user.

In the following sections, we describe a series of experiments conducted with bare thermally drawn piezoelectic fiber and conductive pile fabric ('fur'). The primary samples used in this investigation are shown in Figure 6-2.

6.3 . Measuring Fiber Sensitivity

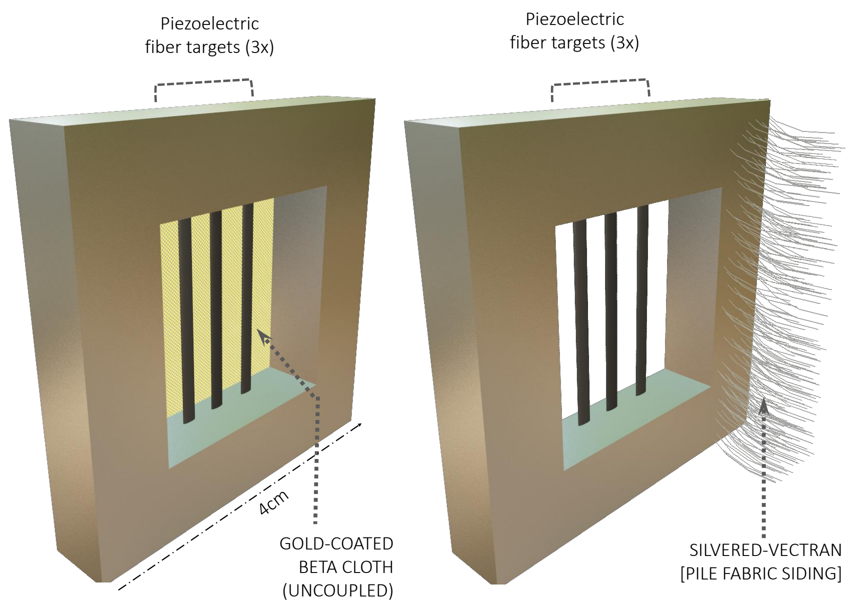

Figure 6-3: (Left) Sample #1: (3x) 4cm long piezoelectric fiber target with goldized Beta cloth backing. (Right) Sample #2: 3x 4cm piezoelectric fiber target with conductive pile fabric siding

6.3.1. Setup

Our first objective is to characterize the acoustic & charge sensitivity of thermally drawn piezoelectric fiber to impactors at high speed. It is the first time piezoelectric fiber is subject to these conditions. The piezolectric fiber base sample is shown in Figure 6-2, and specific sample configurations are shown as renders in Figure 6-3.

These samples are baked for 48 hours and installed in the facility's UHV chamber (see also Figure 6-10 in later section). U.fl coaxial cables route signal to a nearby amplification stage. The majority of experimental runs use commercial readout electronics selected specifically for this campaign - Cremat CR-110 Charge Sensitive Amplifier (gain of 1400 mV / pC). Meter-long BNC cables then route signal via electrical passthroughs to the exterior of the chamber and into a Cremat CR-200 pulse shaping stage with either 2.4μs or 19μs pulse width (FWHM). Additional gain on this stage is configured per experiment, then calculated and calibrated out during the data processing phase by comparing the raw CSA output and pulse shaper output.

Impactors are incident at a fixed 0° angle. The sample is suspended via thin, flexible lines of Kapton from a rigid mounting beam to minimize acoustic coupling. In the first configuration, three thermally drawn fibers, each 4cm in length, are anchored at the tips to a metal frame, suspended on a chamber mounting point, and exposed to the particle beam. This setup was designed bearing in mind that the particle beam diameter is on the order of 1cm. Therefore, this fiber-only setup ensures that any acoustic events are due to a particle incident on a fiber (as opposed to fabric or frame). In addition, pile fabric, motivated in later sections of this chapter, is maintained on the frame as a supplemental charge detection medium.

In the second configuration, a goldized beta cloth fabric backing is added to the frame (with a 1mm gap - ie/ not in direct contact with the fibers). In these experiments, it is no longer possible to discriminate between a particle striking the piezoelectric fiber vs. goldized backing, but in general terms, greater charge production for certain impactors is anticipated.

Due to ultra-high-vacuum cleaning and bakeout requirements for any item introduced in the chamber, strict 8hr per day accelerator access, many-hour requirement for pumping down the chamber, and 3-channel read-out limit, only one experiment setup could be treated per day of beamtime. Note that data from two fibers are shown in this chapter. Data from the third piezoelectric fiber was dedicated to collection of supplemental calibration data for flight electronics and is not presently included in this study.

6.3.2. Motivation for Use of Goldized Beta Fabric Backing

As previously noted, in all charge sensing experiments and a subset of piezoelectric fiber experiments, gold sputtered beta fabric is used as a target material. The motivation for this experiment design is as follows. In this first experimental run, there was uncertainty regarding fiber sensor performance in these new kinematic regimes, and for this reason, maximizing impact charge production was set as an experimental priority.

Table 1. Impact Charge Yield Relations From the Literature, After *Auer* [2001][a]

Target Material	Scaling Relation	Range (km/s)	10 km/s	50 km/s	Reference
Al	$7.0 \times 10^{-1}\, m^{1.02} v^{3.48}$	2–40	1,060	287,000	*McBride and McDonnell* [1999]
W	$5.1 \times 10^{-1}\, mv^{3.5}$	2–40	1,610	451,000	*Dietzel et al.* [1973]
Al	$1.4 \times 10^{-3}\, mv^{4.8}$	8–46	88	200,000	*Grün* [1984]
Au	$6.3 \times 10^{-4}\, mv^{5.6}$	9–51	2,508	20,600,000	*Grün* [1984]
PCB-Z Paint	$4.7 \times 10^{-3}\, mv^{4.1}$	3–36	59	43,400	*Grün* [1984]
Antenna (Ag/BeCu)	$5.0 \times 10^{-2}\, mv^{3.9}$	3–40	397	211,000	*Grün et al.* [2007]
Kapton (Al coated)	$1.0 \times 10^{-2}\, mv^{4.6}$	3–40	398	654,000	*Grün et al.* [2007]
Polyimide	$1.2 \times 10^{-1}\, mv^{3.3}$	3–45	239	48,500	*Grün et al.* [2007]
Ag	$8.9 \times 10^{-3}\, mv^{3.9}$	2–40	71	37,600	This work
BeCu	$1.2 \times 10^{-2}\, mv^{3.8}$	2–30	76	34,300	This work
Kapton (Ge coated)	$2.5 \times 10^{-3}\, mv^{4.5}$	2–40	79	110,000	This work
Solar cell	$4.7 \times 10^{-3}\, mv^{4.2}$	2–40	74	64,200	This work
MLI[b]	$1.7 \times 10^{-3}\, mv^{4.7}$	2–40	85	164,000	This work

[a]Scaling relation mass in kg, speed in km/s, example yields are in fC for a 1 pg projectile at the indicated speeds.
[b]MLI, multilayer thermal insulation.

Figure 6-4: q=mv^x scaling relations and impact charge yield for various target materials subject to impact in the km/s - 50km/s regime. Note that gold is shown to produce orders-of-magnitude more charge in comparison to other common space materials (Reprinted from [17]).

There are three sources of charge relevant to these experiments: (1) surface charge of the impactor (2) surface charging internal to piezoelectric material (3) charge released in the impact plasma plume.

In the ultra high speed regime accessible by this facility. Impact plasma charge production becomes meaningful. Figure 6-4, reproduced from [17], quantifies impact plasma charge production for various common spacecraft materials at different speed regimes. While charge production is similar across materials in the 1 km/s speed regime, gold is found to produce between 2x-40x more charge in the 10km/s speed regime (30x charge relative to MLI), and 45x-600x more charge in the 50km/s regime (125x relative to MLI). Specifically, for a 1pg projectile at 10km/s, gold was measured to produce 2.5 picocoulombs, and at 50 km/s, gold was measured to produce 20.6 nanocoulombs. Hence by coating fabric targets in gold, we anticipate the benefits of high charge production while preserving the material properties of Beta cloth. To my surprise, goldized beta fabric actually has a legacy from the early days of spaceflight, where its beneficial radiation and heat shielding properties are leveraged. Now, I propose yet another function for this gold!

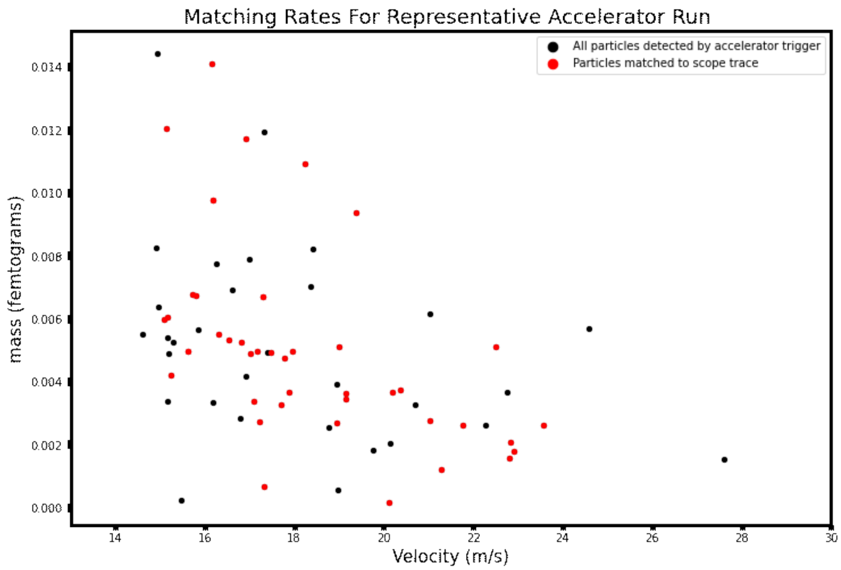

Figure 6-5: Representative example of matched elements in dataset, showing no correlation with mass or velocity. Depending on accelerator configuration, some particles may not enter the chamber. A false negative in the data-matching post-processing step is also possible.

6.4 . Data Processing

The process to match trace files from a LeCroy WaveRunner scope to the particle metadata produced by the accelerator's triggering system is ultimately simple, but building confidence in the matching quality (and minimizing false positives) is involved. To build confidence in the chosen method, I first hand-annotated data from several runs to indicate which runs show a clear signal. From there, a velocity estimate is computed: when a trigger pulse is detected, it is used in conjunction with the physical distance between the trigger and the target to estimate velocity. When a trigger pulse is not available (such as when triggering off of the FPGA for high speed shots) then velocity is estimated more coarsely, taking t=0 as a reference. Next, timestamps with sub-second accuracy are extracted from both repositories and a time delta is estimated. Finally, a peak detector estimates maximum peak.

Once velocity estimates, timestamps, and detected peaks are extracted, a set of trigger conditions are required. As a reference example from one charge experiment:

- Estimated velocity within 0.7x to 1.3x database
- Timestamp delta between 580ms and 750ms
- Peak at least 25mV (ie/ SNR > 2)

These trigger conditions resulted in successful matching of 96 out of 140 database entries for an example run, as shown in 6-5. Note that these criterion are only offered as an example. Trigger conditions are customized to the unique characteristics of each run, and sometimes, timestamp is relied upon more heavily than estimated velocity. Qualitatively, Figure 6-5 also shows that there is no velocity or mass dependence on this matching algorithm. While some further optimization may be possible to increase matching rates, the current triggers are designed to exclude false positives with strong confidence (even at the expense of statistics). There are several explanations for the unmatched database entries. Some particles may pass through the beamline trigger but fail to reach the chamber due to glancing collisions at the chamber entry point. Some may in fact have reached the target, but may not meet the trigger conditions set (ie/false negatives). Finally, some may produce charge yields that are below the detection threshold for our system, due to the stochastic nature of collisions, or variations in the deposited gold at the impactor site.

6.5 . Thermally Drawn Fiber Sensitivity

Figure 6-6 shows representative CSA output (pulse shaping stage omitted) for piezoelectric fiber impact at low velocity ($<$2km/s) and large diameter ($>1\mu$m). Acoustic ringing is clearly observed through at least 1-1.5km/s. Figure 6-7 then shows CSA output for larger v ($>$ 16km/s) and small diameter ($<$ 66nm), which takes the form of pulses visible on both channels. The black trace corresponds to the central fiber and is more likely to be closer to the impact site.

Note once again that a goldized beta fabric backing is included in these trials,

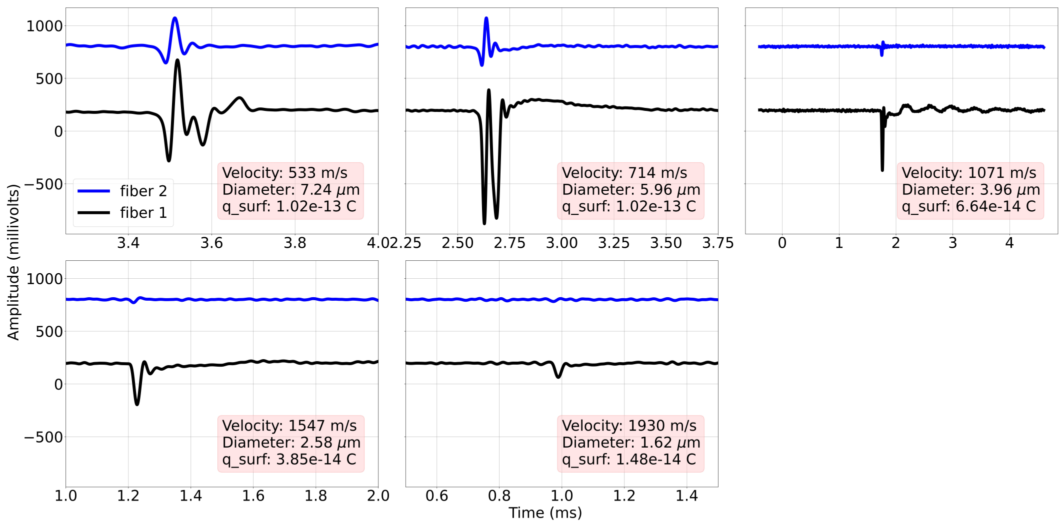

Figure 6-6: Piezoelectric fiber raw CSA output (no pulse shaping). At lower velocities, classic piezoelectric ringing observed, building confidence in an acoustic detection

and is a source of possible charge plasma. Meanwhile, the piezoelectric fibers are suspended 1 mm on top of this fabric. Thus, we believe that the piezoelectric fiber is behaving as a bimodal sensor - detecting impact predominantly via acoustic effects in lower momentum regimes and via electromagnetic effects in higher momentum regimes.

One limitation we underscore about this facility is that mass and velocity regimes are correlated and restricted. This was conveyed in Figure 6-1 - at 10km/s for instance, particles typically do not exceed 100nm, and require extended campaigns to reach 200-300nm at any statistical significance. Hence, it is possible that more massive particles would continue to show acoustic effects even in the velocity regimes probed.

So, we have established via an illustration in the time domain that the piezoelectric fibers are dominated by acoustic sensitivity at low velocities, and potentially by charge sensitivity at higher velocities. Next, Figure 6-8 shows charge yield data across the full 500m/s to 25km/s regime, presenting impact velocity as a function of q/m as is standard (e.g. see [34]). This yield is computed using each channel's maximum peak. A q/m fit proportional to $v^{2.43}$ fits this full velocity range. Referring back to Table 6-4, this fit is only weakly

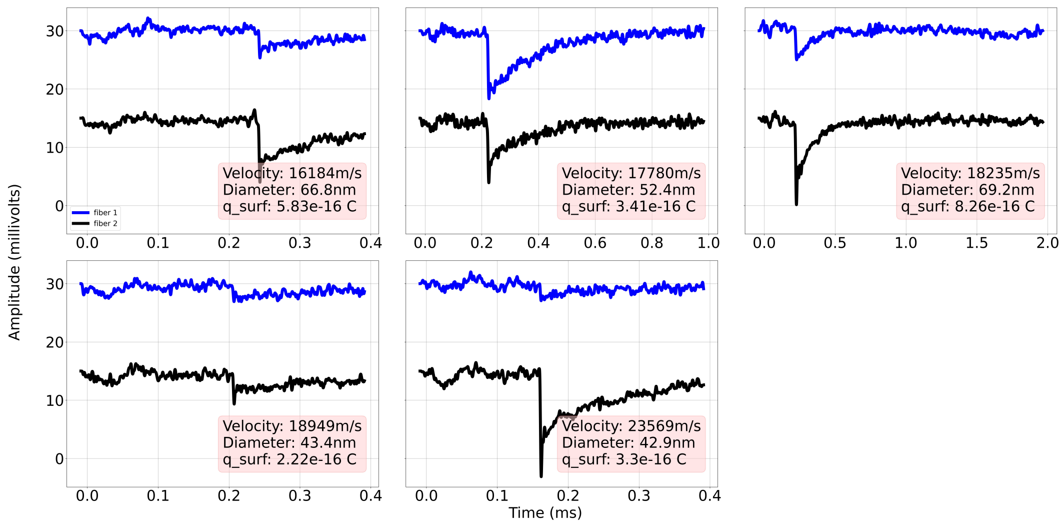

Figure 6-7: Piezoelectric Fiber raw CSA output (no pulse shaping). At higher velocities, pulses are observed that may correspond to electromagnetic rather than acoustic signatures.

velocity dependent compared to previous measurements.

How much of this signal is due to the goldized fabric backing, vs. plasma charge from impact on the fiber's SEBS cladding, vs remanent acoustic signatures? To find out, we proceed now to a direct study of fabric-based impact plasma charge detection.

6.6. Exploring Pile Fabric ('fur') as Charge Sensor

As thermally drawn fiber is sensitive to charge, we move to studying charge released from a gold-sputtered Beta fabric target, omitting the piezoelectric fiber for the next several trials.

In particular, we explore the capacity for an electrically conductive pile fabric ('fur') topology to detect this impact plasma charge. Owing to significant increases in surface area compared to a single-wire or planar conductor, pile fabric will be shown to outperform planar and wire substrates in sensitivity. In addition, the angular dependency of detection is studied. Conceptually, the purpose of this experiment is also to take a first step towards mating sophisticated and creative fabric design with an experimental physics objective.

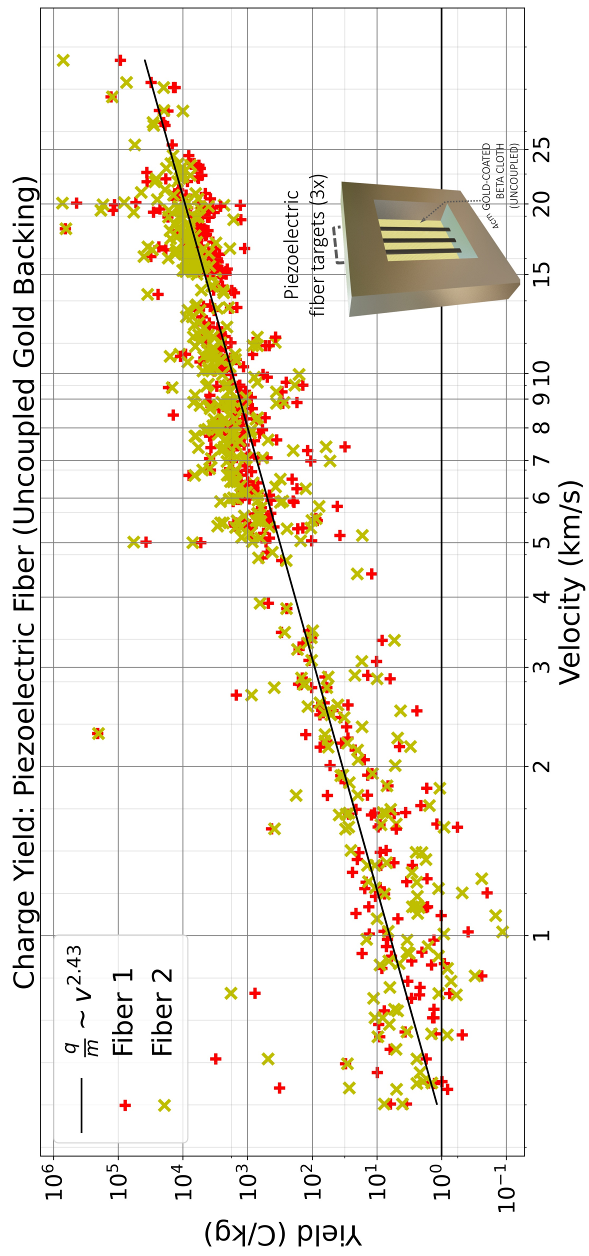

Figure 6-8: Charge Yield for Piezoelectric Fibers with goldized fabric backing

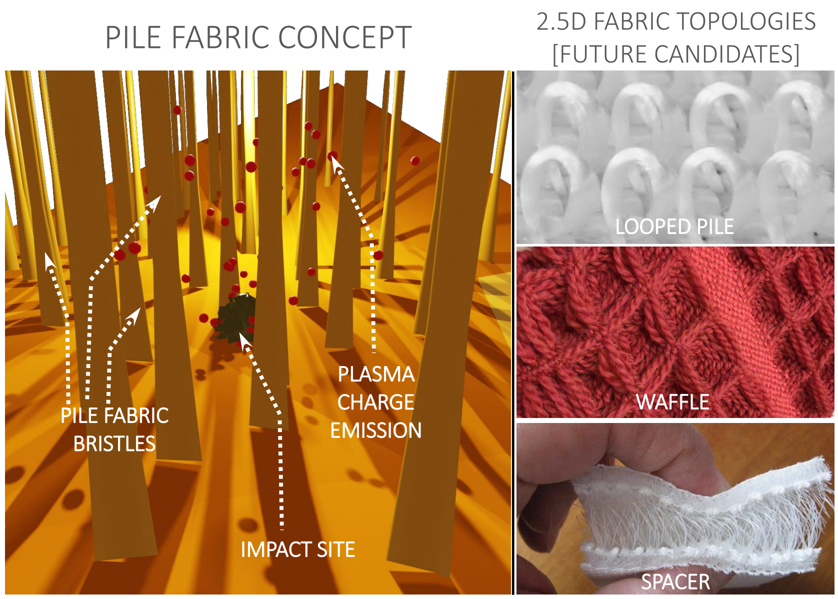

Figure 6-9: Pile fabric concept: increased surface area and unique geometry for sensing impact plasma charge. Other possible interesting fabric topologies are also shown.

This experiment is intended to inspire more such design proposals from a diverse set of researchers.

6.6.1. Prior Art in Plasma Charge Anisotropies

Some brief context is provided on our understanding of impact plasma charge. The amount of generated impact charge is a function of impact velocity, angle of incidence, particle mass, and spacecraft material.

In Figure 6 of [18], Crawford et al. show substantial variability in charge ejection angle for mm-scale aluminum projectiles incident at a constant 0° (ie orthogonal) on carbonate targets, with maximum charge between 30-40° for the 3-5km/s velocity regime. And in 2014, Collette measured variations in impact charge yield on MLI and silver as a function of incident angle and found modestly greater charge yield at 40° incident, shown in [17]. To summarize - in the former experiment, incident angle is fixed, and charge shown to vary by angle, and in the latter experiment, incident angle is swept and charge is reported as a single, modestly varying yield measurement.

These effects have also been studied in simulation. For instance, in [26], Close et al. simulated plasma production from hypervelocity impact and found a plasma plume density highest at 45° to the right for an impactor incident at 45° from the left, rapidly expanding away from the planar target at speeds up to the incident particle velocity.

Thus both in simulation and experiment, the charge production in hypervelocity impact is believed to be anisotropic. There are two separate effects at play - the charge distribution intrinsic to a plasma plume and independent of angle, and the variation of this charge distribution as a function of incident angle.

While mirror charging effects will induce current on all nearby conductors, the induced charge will scale with distance and quickly fall off for charge ejected at angles. For direct capture of charge on a surface, we will need additional surface area extending beyond the flat sensor. (See artistic sketch in Figure 6-9 for intuition. Bringing to bear the landscape of available fabric topologies, how about pile fabric ('fur')? Fur is not the only possible architecture. Other future possibilities I have conceived include waffle type fabrics, microinflatable arrays, and other designs, some of which are also shown in Figure 6-9. In fact, we believe an interesting work could attempt to correlate fabric topology to charge sensor performance. For our immediate purposes, fur has the advantage of maximal surface area and tightly controlled sparsity. We also find the notion of a 'furry spacecraft' brings some curious appeal that will help inspire future work in the area. As a personal aside, while conducting our multi-day Van de Graaff impact campaign, the fur first provoked the curiosity of several students and professor passersby, and then sparked technical conversation. I sensed that I had fulfilled my duty as a Media Lab student - to shepherd an unusual, early-stage, and crosscutting concept into an advanced experimental physics facility !

6.6.2. Experiment

Fur is constructed using brushed silvered Vectran stitched onto a flat conductor and mounted on a rotating plate inside the UHV chamber (to allow for

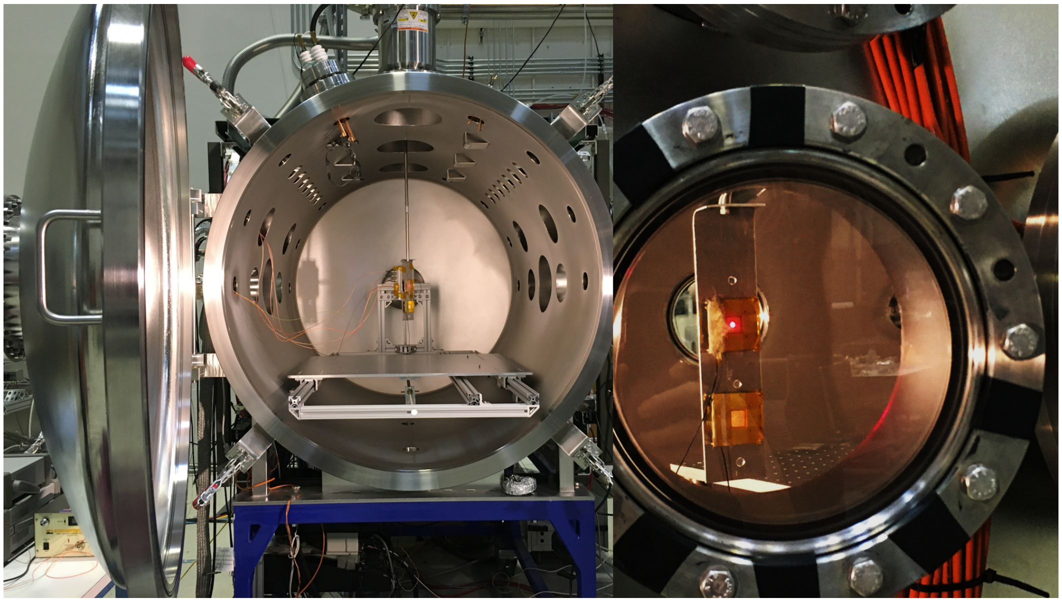

Figure 6-10: Pile Fabric targets shown mounted inside UHV chamber at beamline. An alignment laser illuminates target.

variation in impact angle) as shown in Figure 6-10. A series of experiments are conducted with the following free parameters:

- Fabric Topology (Pile vs Planar)
- Conductor Potential (Biased to +100v vs Grounded)
- Impactor Angle of Incidence (0,25,50°)

Figure 6-11 is a key result. These plots show a comparison of biased pile and planar fabrics across 3 incident angles. This data represents 12 independent accelerator runs, and demonstrates that a pile target detects one order of magnitude more charge than a planar target. Estimating the total surface area of the pile detector on the basis of individual surface area of 5000 bristles as $2\pi \cdot 30\mu\text{m} \cdot 3\text{cm} \cdot 5000 = 283\text{cm}^2$ in comparison to the 8cm^2 surface area of a planar conductor, we are not too far off in anticipating one order of magnitude greater charge collection. Recalling the method of [17] for capturing charge, which involves a secondary grid biased to -120V to repel plasma charge back to the sensor target, I believe this modified scheme using biased fur is allowing a 2.5D fabric sensor to do something similar in order to capture most or all of the charge.

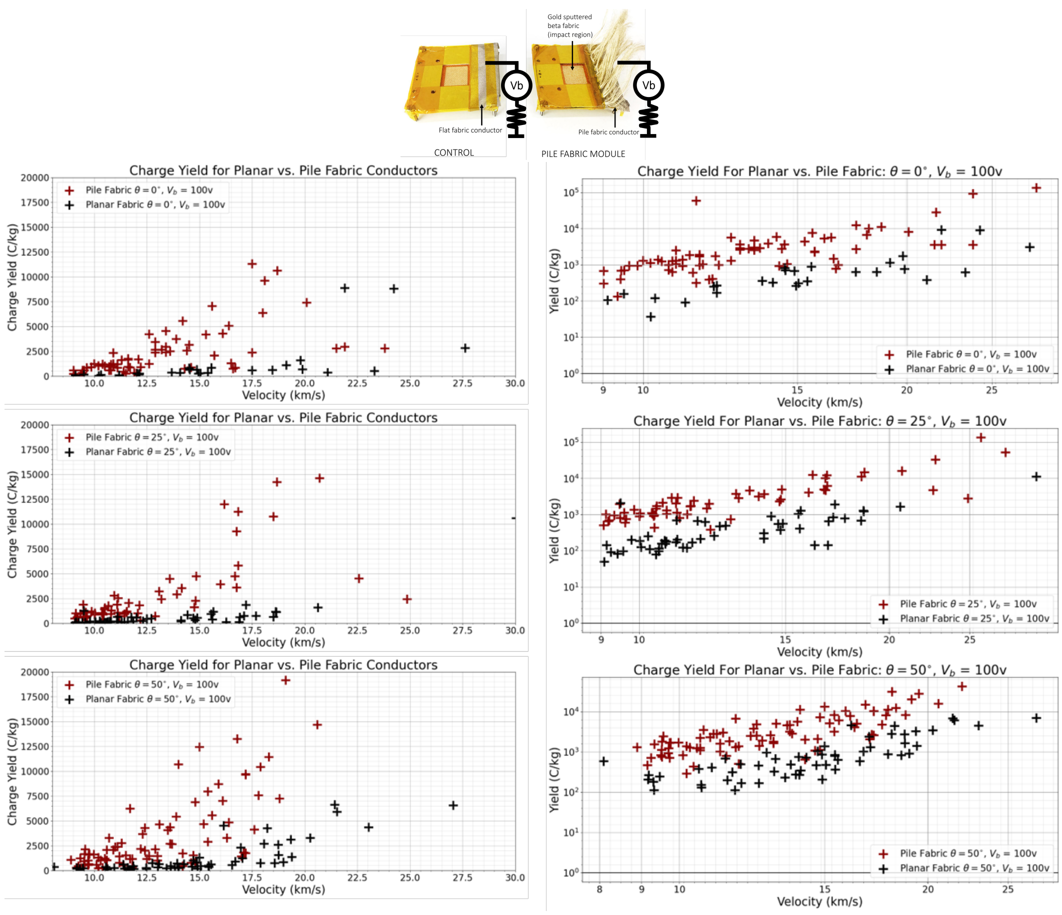

Figure 6-11: Pile fabric is more sensitive to charge at 0, 25, and 50°

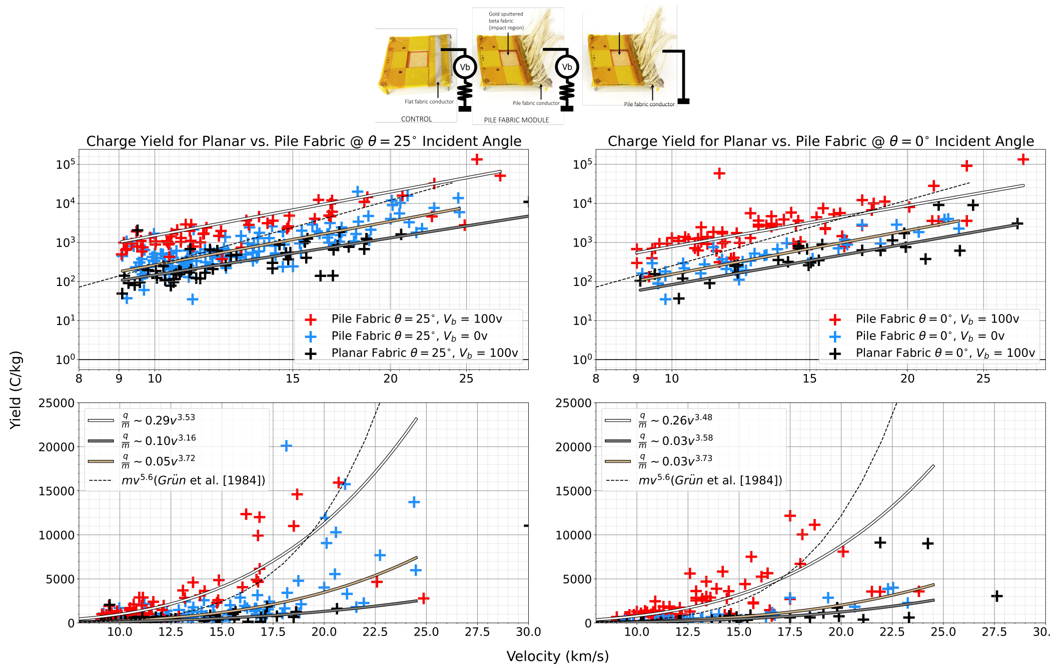

Figure 6-12: Biased pile fabric outperforms unbiased pile fabric and biased planar fabric in charge sensitivity at 0° and 25°

These results also enable us to crosscheck charge production order of magnitude. Note that the charge reported here is the yielded plasma charge Q_p, (distinct from the surface charge of the incident particle.) Referring again to Figure 6-4, in the e.g. 10 km/s regime, a gold target is expected to produce 30x more charge than an MLI target (a 1pg projectile mass is assumed). Referring to Figure 3 in [17], the MLI charge yield at 10km/s is on the order of 10^2. With an assumption that the 30x factor holds across the femtogram-scale mass regimes tested, the charge yield for a gold target is expected to be on the order of $3 \cdot 10^3$ C/kg. And indeed, we measure the correct order of magnitude. The previously reported fit (by Grun et al.) or a gold target is plotted as a dotted line in many plots showing results.

Next, Figure 6-12 additionally plots pile fabric at 0° bias and shows evidence that unbiased pile fabric even notches out 100v biased planar fabric in performance. Figure 6-12 also plots Grün's power law fit for gold targets, finding reasonable agreement particularly with biased pile charge magnitudes.

Due to increase capacity for direct charge capture, we anticipated that fur might outperform planar conductor in angular sensitivity, under an assumption that the charge plume's spatial density varies. On the one hand, for a biased target, Figure 6-11 shows no angular dependency - attractive forces from a biased target may significantly influence charge trajectories. However, 6-12 shows some potential angular dependency for an unbiased target. As an unbiased target would be preferable for spacecraft walls, additional data collection for unbiased targets would be useful to either confirm or deny this possibility.

Finally, regarding dependency of incident angle on measured charge, no significant effect is observed in the 0-50° regime on biased pile fabric. A slight effect may be observed comparing unbiased pile at 0° and 25°, especially at velocities >20v, which would seem in line with our suspicion that at more oblique angles, unbiased piles are superior performers. These results are shown in Figure 6-13. These measurements are unlikely to be explained by differences in the overall magnitude of charge produced by angle, based on angular charge magnitude results by [17] for MLI and silver. Instead, any possible variation on an unbiased target would be explained by variations in the charge density of the plasma.

Whereas pile fabric is likely directly capturing the released charge, planar fabric measurements are explained by mirror charging effects. The electric field strength, and induced charge, is expected to scale as $1/R^2$. A electron traveling 2cm at a 25° angle will be 1cm away from the target. At 1cm, mirror charging effects will be 100x weaker than at 1mm distance.

One apparent feature of this experiment setup is the explicit separation between target and sensor. While logical for this initial test, on a genuine fabric, conductive pile would need to be incorporated directly (and with well-tuned sparsity) into goldized Beta cloth.

Thus, we seek an opportunity to perform additional unbiased target measurements at a later date, including collection of a larger dataset under the current conditions (which would increase statistics at higher velocities) as well as a reliable control dataset for unbiased planar fabric targets, which is not included in the current analysis. Finally, we seek to electrically couple the goldized Beta

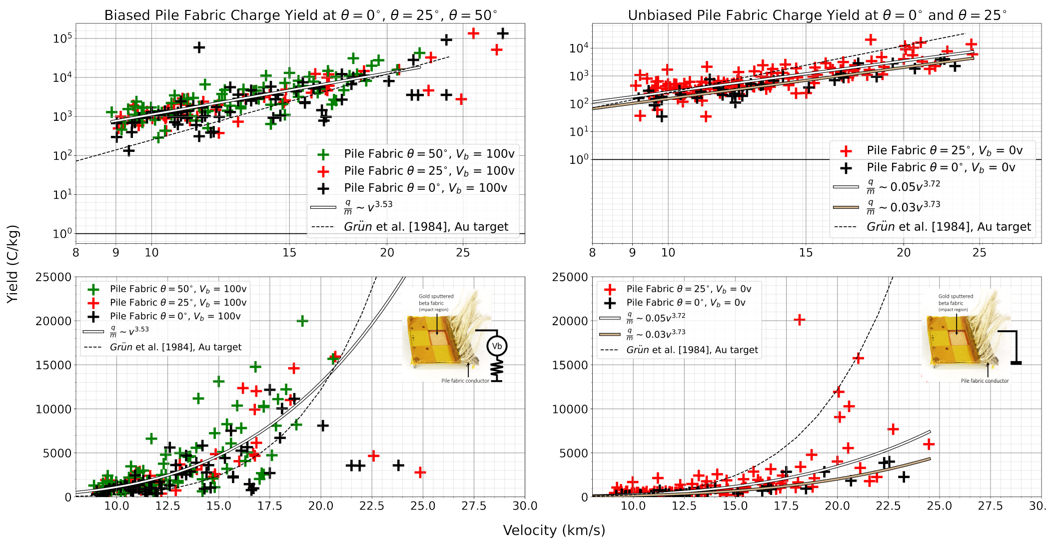

Figure 6-13: Figures on the left show, for a BIASED pile fabric target, no sensitivity to incident angle (0°,25° ,50°). Figures on the right show, for GROUNDED pile fabric, possible angular dependence. More data is necessary for statistical significance.

fabric to the planar/pile conductors as a secondary control, explicitly merging impact site with sensor.

6.7 . Fiber Sensor and Pile Fabric

We have shown that pile fabric outperforms planar fabric in sensitivity. We have also shown that piezoelectric fiber stacked on top of a gold target (with a few mm of spacing) likely senses induced plasma charge. On the one hand, designing a fabric that accommodates this gap would be an interesting design challenge. On the other hand, can we now demonstrate operation of a multi-modal sensor on a single piece of fabric, without spatial gaps needed.

Figure 6-14 shows these two sensor modalities (electromagnetic, acoustic) working in tandem. Due to mirroring effects, the fur can predict the onset of a particle due to its positive surface charge with around 40μs notice. In the illustrated case, the impactor particle contains 12.46fC of surface charge, and is traveling at 1705m/s. With CSA gain of 1400mV/pC, a 12.46fC surface charge would generate 17.44mV, in line with the observed pulse height 20mV,

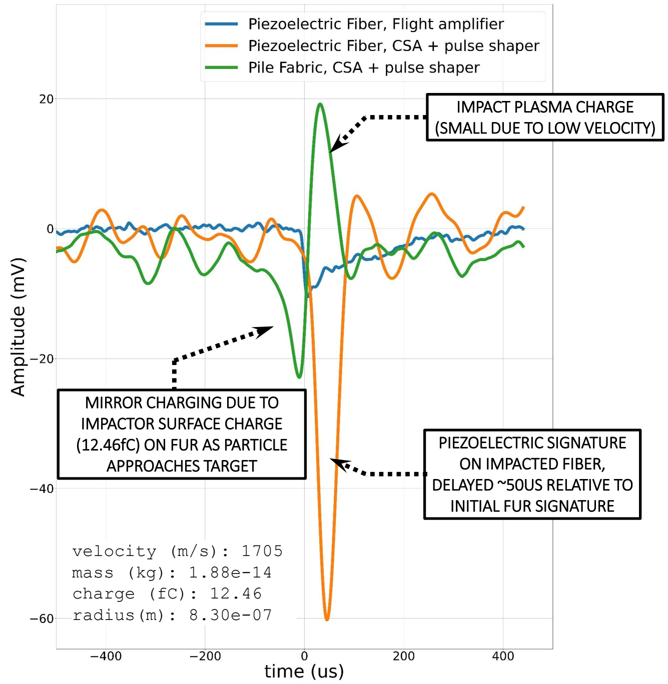

Figure 6-14: Multimodal sensing using both piezoelectric fiber and fur for 830nm, 1.7km/s impactor. Time delay shows arrival of particle.

which is bloated due to the 5mV observed noise floor). The 40μs time delay between pile fabric signal onset and piezo fiber signal onset corresponds to 6.8cm of travel distance. Given the fur bristle height of 5cm, this implies another advantage to fur - early detection onset on the order of 1-2cm from fur bristles, which are offset relative to surface.

Then, the piezoelectric fiber is struck and might even show slight ringing (we are in a kinematic regime where ringing is possible, yet up against the noise floor). The charge produced in impact plasma is then detected by the fur as well as a second nearby piezoelectric fiber.

We are beginning to tell a story using only a fabric sensor.

Indeed, the three plots in Figure 6-15 suggest that even bare fiber (without goldized backing, and without pile fabric) is sensitive at speeds up to 15km/s. However, the addition of even an unbiased pile fabric increases sensitivity by an order of magnitude! As there are differences in the reported fits across trials, each of three trials is reported independently, and more data is preferred.

6.8 . Conclusion/Key Takeaways

- Piezoelectric fiber shows sensitivity dominated by acoustic effects down to impactor scales of 2μm, and sensitivity dominated by electromagnetic effects down to impactors scales of 40nm or less.
- Goldized fabric enhances charge production
- Electrically conductive pile fabric increases charge sensitivity threshold, especially when biased
- No sensitivity to impactor angle are observed when biased pile fabric is used. Weak/uncertain sensitivity is observed for unbiased pile fabric targets (more data needed)
- The goldized beta cloth coating is left floating in these trials, and is discrete from the conductive fur. In a genuine space sample, the fur bristles would be dispersed throughout the fabric medium, and the potential of the goldized target substrate should be further investigated.

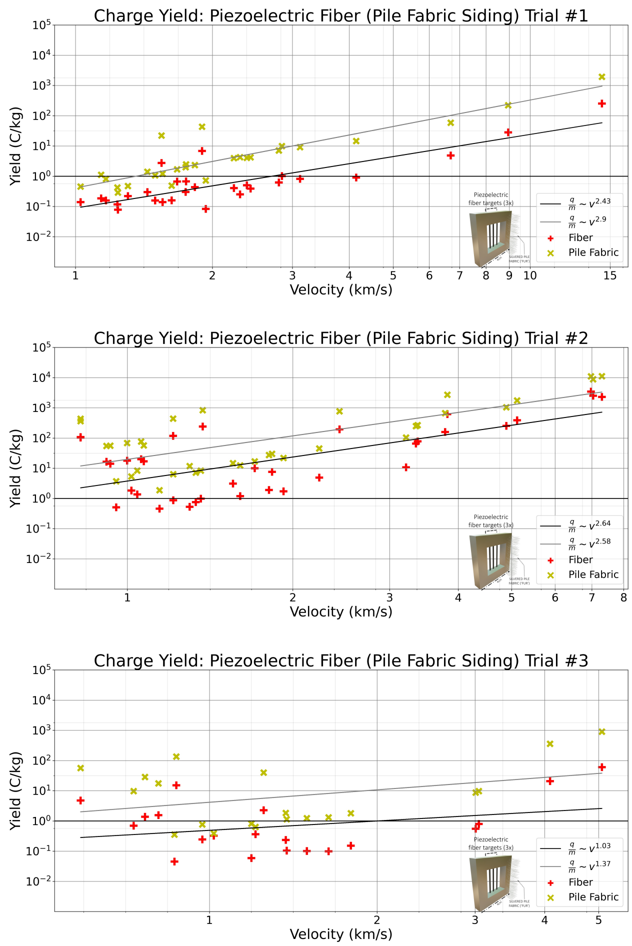

Figure 6-15: Charge Yield for Piezoelectric Fibers with pile fabric siding, 3x trials with variable fits. Therefore, we pay attention only to the consistent out performance of pile fabric over the wire in piezoelectric fiber for sensing charge.

CHAPTER 7

To Low Earth Orbit - Material Performance

At this point, I have reiterated many times the key observation that inspired the current work: that large area, protective fabrics have decades of flight heritage, yet have remain quietly passive. I have also motivated the development and ground testing of electrically active fabric samples.

Now, to Low Earth Orbit! I have sent the first electronic textile sensor to space.

In this milestone for advanced textile development, I begin by addressing prior art in augmented multi-layer insulation (MLI) and spacesuit concepts.

7.1 . Prior Art in Augmented MLI

7.1.1. MLI Passive Functionality

Prior work incorporating passive functionality into a spacecraft's MLI include the Toughened Thermal Blanket, which introduces a layer of Nextel ceramic cloth just behind the top of the thermal blanked cover for added robustness, [16] and the Stuffed Whipple Shield, which offers additional radiation protection to an impact shield [15].

7.1.2. Active Fiber Functionality

The I-Suit from ILC Dover back in 2003 integrated pressure sensitive textile switches into the glove of a spacesuit for rover control, and in the shoulder for helmet lighting control [27]. It is the only known conceptual exploration of the integration of active sensors into the outermost aerospace-grade textile material. Otherwise, two projects are known that propose to embed thin film sensors *inside* MLI: the SanSEc project proposed substituting an open circuit thin film resonant sensor as an MLI inner layer for damage detection [71], and the previously described CLOTH project from JAXA. Space tethers are also electrically conductive.

We, in contrast, are working with textiles rather than thin films, and flying fabric containing a complex internal fiber sensor topology in Low Earth Orbit.

7.2 . Experiment Objectives

The first objective for this space-based exposure experiment is to perform observational and functional testing of piezoelectric fiber sensor components after 1+ years of deployment, including comparison between two different weft-insertion methods for the thermally drawn fiber. Of secondary importance is a study of micrometeoroid impactor sites, which can provide detail on the damage to targets in the kinematic regime of a genuine space dust particle. We can estimate the hit count on fabric using the metal frame, and confirm that no conclusive damage is identifiable on the fabric target. Of tertiary importance is a general comparison between commercial Beta cloth and modified forms. For example, fiber-level Teflon coating rather than textile impregnation, and integration of additional fibers like Teflon spray-coated Liberator liquid crystal conductive yarn.

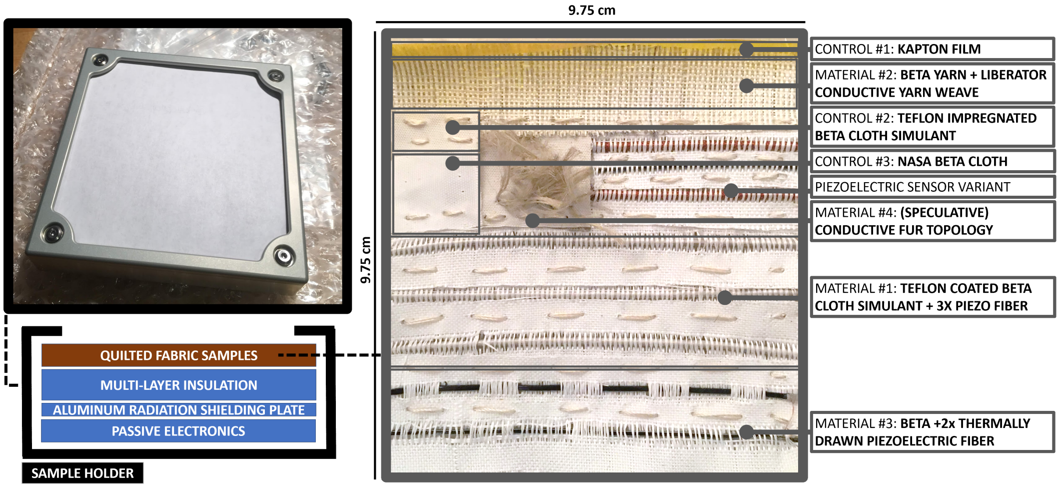

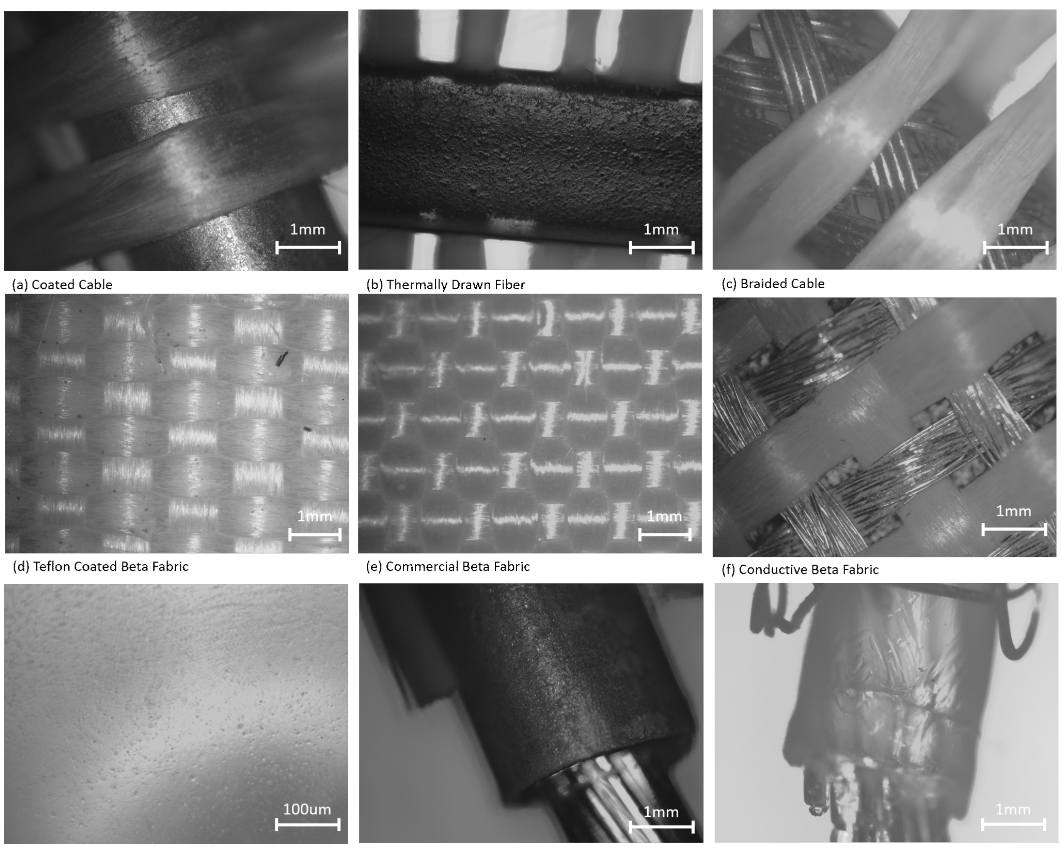

(a) Coated Cable
(b) Thermally Drawn Fiber
(c) Braided Cable
(d) Teflon Coated Beta Fabric
(e) Commercial Beta Fabric
(f) Conductive Beta Fabric
(g) Aluminized Mylar (MLI)
(h) Coated cable tip
(i) Braided cable tip

A summary of the samples tested are shown in Figure 7.2. For additional context, optical microscopy images are shown in Figure 7.2. These swatches are loosely stitched together using fiberglass yarn, intended for straightforward disassembly. Discrete metal frames were originally considered to house each sample, but ruled out since at the time there was still a possibility for a battery-powered launch (and no guarantee yet for a subsequent electrically active launch). As such, maximizing exposure area was deemed a priority in the planning phase over the organizational benefits of discrete frames.

Also shown in Figure 7.2 are the interior layers of the payload. Passive electronics were indeed included, mainly as a contingency against an active launch opportunity. Finally, a thin layer of Teflon was sprayed on top of the fabric as a means to shield silvered material from direct exposure and accommodate a JAXA regulation.

7.3 . Qualification of Payload for Spaceflight

7.3.1. Material and Load testing

The sample is required to pass a load testing qualification, typically at 1.5 lbf across a .0598in diameter surface area. The application of even a small load across 0.056 in diameter surface (slightly less than required .0598 inch surface area) was found to cause perforations in the fabric. In our counter-proposed load test, A clamp was used to apply a minimum 125 * 1.5 lbf = 187.5 lbf force to the sample. The clamp was secured around a desktop, an analog scale, and the sample and was shown to produce no visual damage to the fabric when applied in the region of the coated cables. This method and a corresponding short report were approved by JAXA.

In addition, substantial technical detail on all base materials included in the payload were requested by JAXA and reported to the team.

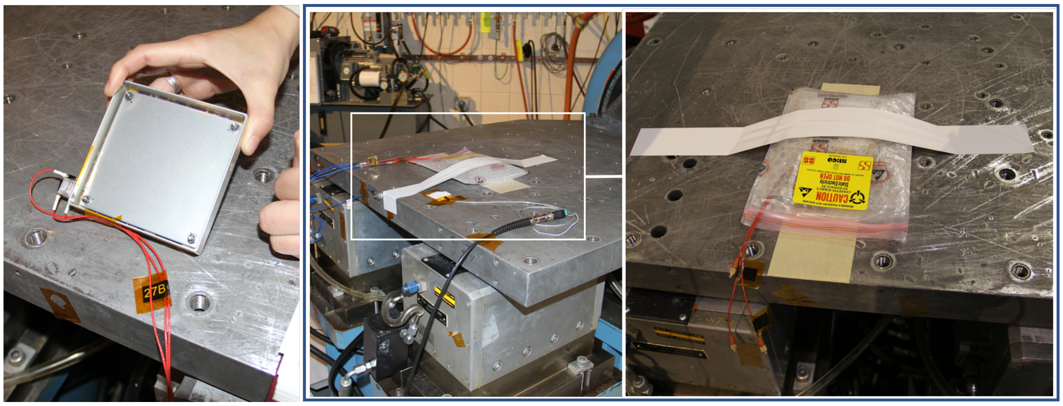

Figure 7-1: Vibration testing of passive payload at MIT Lincoln Laboratory

7.3.2. Vibration and Shock Testing

The sample was required to pass a vibration and shock qualification test, which was conducted at MIT Lincoln Laboratory, with significant support from technical staff member Kelly Beattie.

The sample (fabric + multilayer insulation + metal plate + circuit board + backplate) was placed in the aluminum sample holder and screws were tightened to the requisite torque and marked. A triax accelerometer was mounted on the sample holder. The sample was placed inside bubble wrap provided by JAXA/SpaceBD and taped to the test bed.

The following vibration profile was applied along 3 axes (x, y, z) in order to meet JAXA's qualification requirements.

Freq (hz)	g^2/Hz
20	.04
120	.062
230	.062
1000	.009
2000	.0026

In visual inspection following the test, the sample was not damaged and remained mounted to the sample holder. The screws remained appropriately torqued, as indicated by visual markers.

Finally, prior to assembly, fabric swatches were dehydrated at 60° under vacuum. Data from this shock and vibration test (including actual vibration profiles and a series of detailed photographs) were delivered to JAXA. The material was approved, clearing the sample for spaceflight.

7.4. Journey to Space

This small box did quite a lot of traveling (certainly more traveling than most of us were doing during the earliest stages of 2020's quarantine!)

In April, 2020 the sample was mailed from Boston, MA to Space BD Inc. in Tokyo, Japan. In conjunction with JAXA, several qualification tests were performed, at which point the sample was repackaged and shipped to Wallops, Virginia during the summer of 2020. The payload then launched to Space on October 2nd, 2020 on board Cygnus NG-14 and arrived at the Space Station on October 5th, 2020. In late Oct '20, astronauts inside ISS mounted the payload onto the RAM-facing side of a holder and moved it through the airlock. The Kibo robotic arm then mounted the holder onto the RAM-face of JAXA's Exposed Experiment Handrail Attachment Mechanism (ExHAM) facility on the Station's exterior walls. Between October, 2020 and January, 2022 the sample orbited Earth approximately 7000 times over 15 months, experiencing temperature swings, as an extreme estimate, from -94 °C to 80 °C. In early January, 2022, the sample was brought back into the Station's interior, and on January 24th, 2022 the sample was returned to Earth onboard SpaceX-24, making a splash landing off the coast of Panama.

In February, 2022 the sample was shipped by mail back to MIT. This journey is summarized in Figure 7-2 and the deployed sample is shown in Figure 7-3.

7.4.1. Videography

On three occasions during the first year of sample exposure, we had the opportunity to conduct real-time videography sessions, coordinated by Space

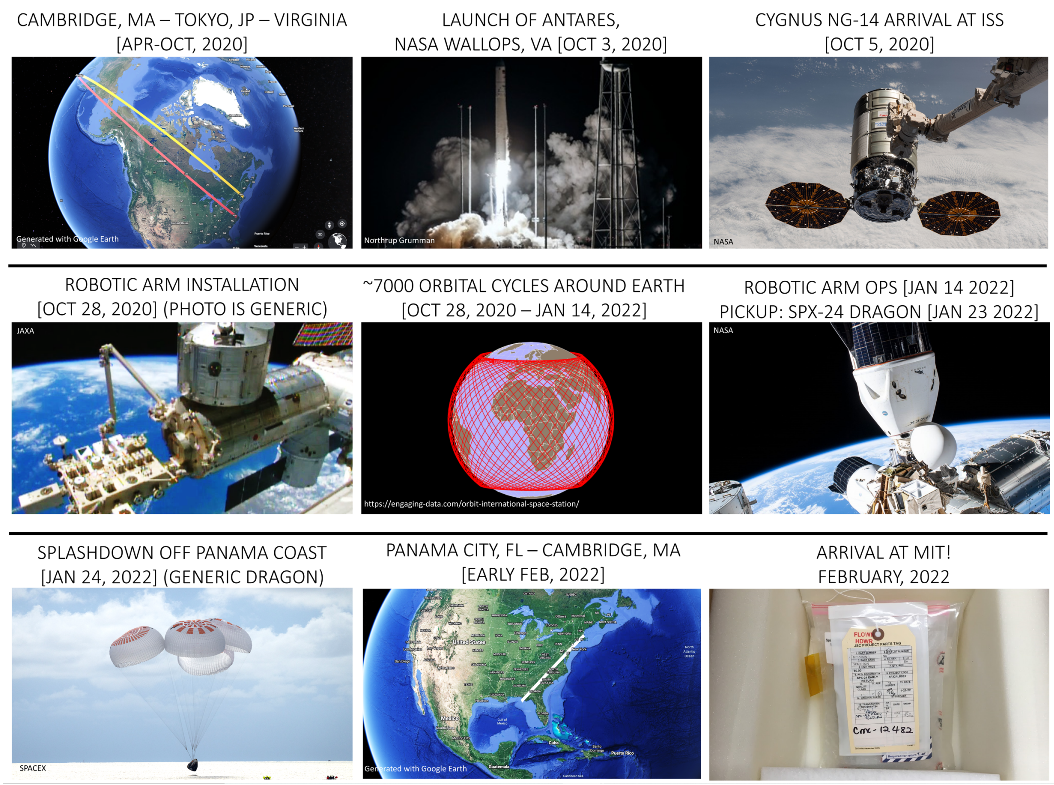

Figure 7-2: Quarantine travel of passive sample

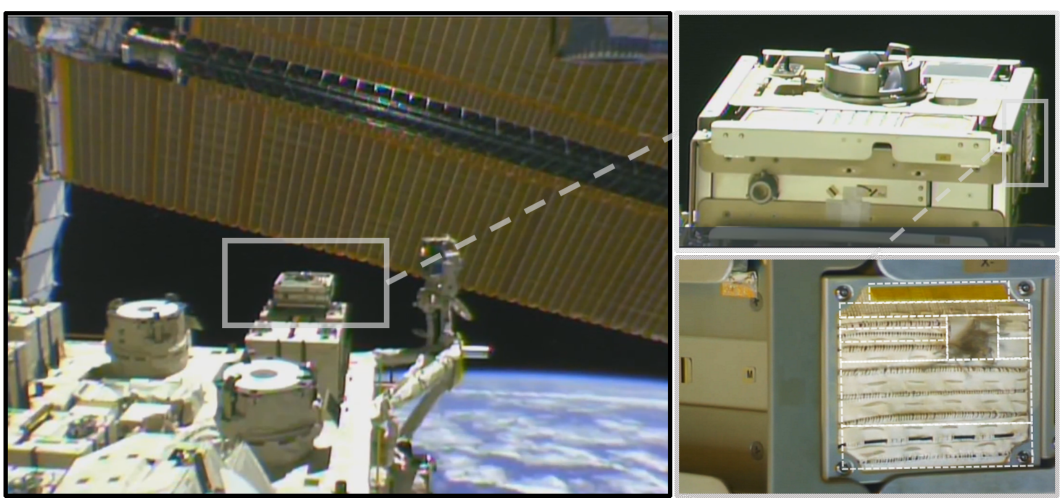

Figure 7-3: Sample deployed on Japanese ExHAM facility

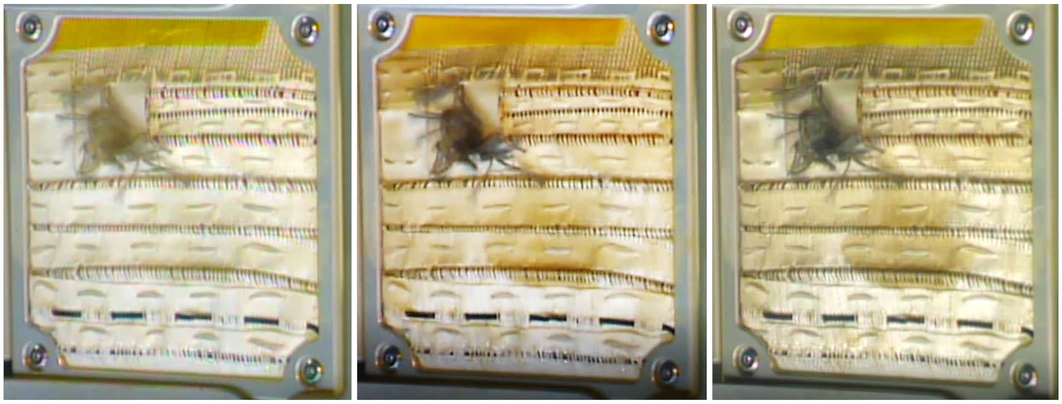

Figure 7-4: Images (excerpted from video) showing gradual discoloration of sample, and kinking of thermally drawn fiber

BD and JAXA. These sessions were used to track damage or any other visual changes to the sample, as well as to generate promotional content for the project.

Figure 7-4 shows the sample's degradation during three real-time videography sessions. While an attempt is made to match lighting condition and coloration in excerpted stills, for more nuance it is best to review the full video, capturing the sample under a wide range of lighting conditions.

By visual inspection, the following observations are made. First, the addition of a Teflon coat may have delayed, but did not prevent, the oxidation of silver present in the Liberator yarn used as fur, plain weave, and as an elastomeric outer conductor for piezoelectric cables. In future evaluation, a more robust protective coating is necessary (such as the white epoxy thermal coating already selected and evaluated in ground tests - see Section 7.7). Otherwise, an alternative conductive metal should be used - the Liberator product line includes bulk, custom-orderable copper or nickel cladding (whereas silver was available in small-batch order). In this way, we benefit from the advantageous properties of Vectran as a base yarn.

Second, there is a gradual local discoloration in the central region of the quilt. Upon sample return, it became clear that erosion extended through the fabric and to the aluminized Mylar backing. As shown in 7-6, this aluminum ero-

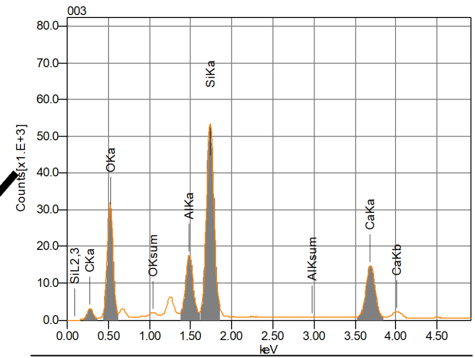

Chemical Formula	Mass%
F	36.37
O	26.94
Si	21.10
Al	5.87
Ca	9.72

Figure 7-5: Elemental analysis of discoloration shows presence of calcium and aluminum

sion trends along the axis of one of the silvered cables, and the beginnings of some erosion underneath one of the thermally drawn fibers is also visible in the erosion shape, including weft yarn patterning. As the piezoelectric fibers would depole long before aluminum melts, we believe that the aluminum was scratched off via friction effects by induced thermal expansion and contraction of the fibers. The fibers may evidently have become hotspots on the fabric's surface. These aluminum particles may also be responsible for the discoloration region, as free aluminum flecks will tend to penetrate the fabric over time and then oxidize.

This region was further studied using elemental analysis, and results shown in 7-5. In addition to fluorine (from Teflon coating) and silica (from fiberglass), aluminum and calcium oxides are detected. Indeed, this measurement provides evidence for our suspicion that aluminum from the aluminized Mylar backing leeched onto the fabric's surface after friction removal. The presence of calcium, however, is suggestive of a contaminant. Is it possible that a contaminant substantially influenced the thermal expansion/contraction of the fabric in this regime?

Material	$\alpha(\frac{mm}{mm\cdot{}^\circ C})$	k $(\frac{W}{m\cdot K})$
$BaTiO_3$	$\sim 10^{-6}$	1.3 to 6
SEBS	$16 \cdot 10^{-5}$	0.46 – 0.66
CPE	$7 \cdot 10^{-5}$	0.3-0.8
PVDF	$6.6 \cdot 10^{-5}$	0.181

Table 7.1: Thermal expansion coefficient α and thermal conductivity k for key materials inside thermally drawn piezoelectric fiber. Note that thermal conductivity can vary with temperature

Bearing in mind this explanation for the discoloration, why would this region of fabric have been preferentially affected? In the same region, an additional clue is a defect observed in the sparsely woven 10cm long thermally drawn fiber, shown clearly in Figure 7-6. Evidence from shadowing in real-time videography footage indicates that this defect was present even in November, 2020. We strongly anticipate this to be a buckling effect induced by variation in the thermal conductivity and thermal absorption of the internal layers of the piezoelectric fiber. Although thermal expansion coefficients and thermal conductivity of CPE, PVDF, and $BaTiO_3$ are comparable (Table 7.1), the internal CPE layer's black color will tend to concentrate solar absorption in the internal layer, and will tend to make it heat significantly more than the optically transparent SEBS cladding. Refer to our thermal absorption measurements (Figure 7.1. Kinking of the fiber suggests a local hotspot in this region of fabric. As the sample layup was under compression, it's possible that the compressive force was greatest in this region, creating elevated friction in this region.

On the other hand, no kinking is observed in the densely weft-inserted fiber, despite being subject to the same harsh conditions. Hence, we now have a material-driven justification for plain weave, as this buckling would affect twill, satin, and basket weaves alike. (An additional possibility is to trial the previously referenced external white thermal coating).

Figure 7-6: Images taken of sample returned to Earth, showing kinking of thermally drawn fiber and erosion of aluminized Mylar internal layer below the primary discoloration region

Fiber	C_p cap. meter (pF/cm)	C_p RCL (pF/cm)	R_P (MOhm)
Flat Fiber	18.9	18.4	51
Kinked Fiber	14.4	17.2	1.9
Ground Ref. 1	15.8	N/A	7.1

Table 7.2: Capacitance and series resistance measurements for thermally drawn fiber

7.5. Electronic Characterization

Briefly, a basic resistance measurement suggests that the silver elastomeric conductive coating on the 10cm coated cables remains $\ll 50\ \Omega \cdot m$. The Teflon coating does not appear to have shielded from erosion, yet conductivity remains high.

From here, we focus our efforts on the thermally drawn fiber. First, a qualitative test confirmed that both fibers preserved at least some sensitivity to an acoustic impulse (ie a clap). It was another good moment during this project's lifecycle, shared with Grace Noel and Henry Cheung. The thermally drawn fibers survived 15 months of RAM-facing spaceflight and are operational!

Quantitatively, Table 7.2 shows minimal loss of capacitance, though potentially significant loss of resistance in the kinked fiber. The good news is that any change in these material properties does not seem to have significantly influenced fiber sensitivity (order of magnitude) in the crucial frequency range below 5kHz. Performance was assessed collaboratively with fellow RA Grace Noel by measuring transfer function for each fiber in a dedicated tabletop acoustic testbed at the MIT RLE built by Fibers@MIT masters student Henry Cheung and shown in Figure 7-7. The fibers were mounted on a 25 μm Mylar membrane suspended in an aluminum frame and subject to pure tones adjusted to a constant 70 dB Z (SPL). A dedicated condenser microphone is used for sound pressure measurements. There may have been some shifting of resonant peaks, but the general sensitivity level appears consistent. The data is also shown in Figure 7-8 in Log-Log scale.

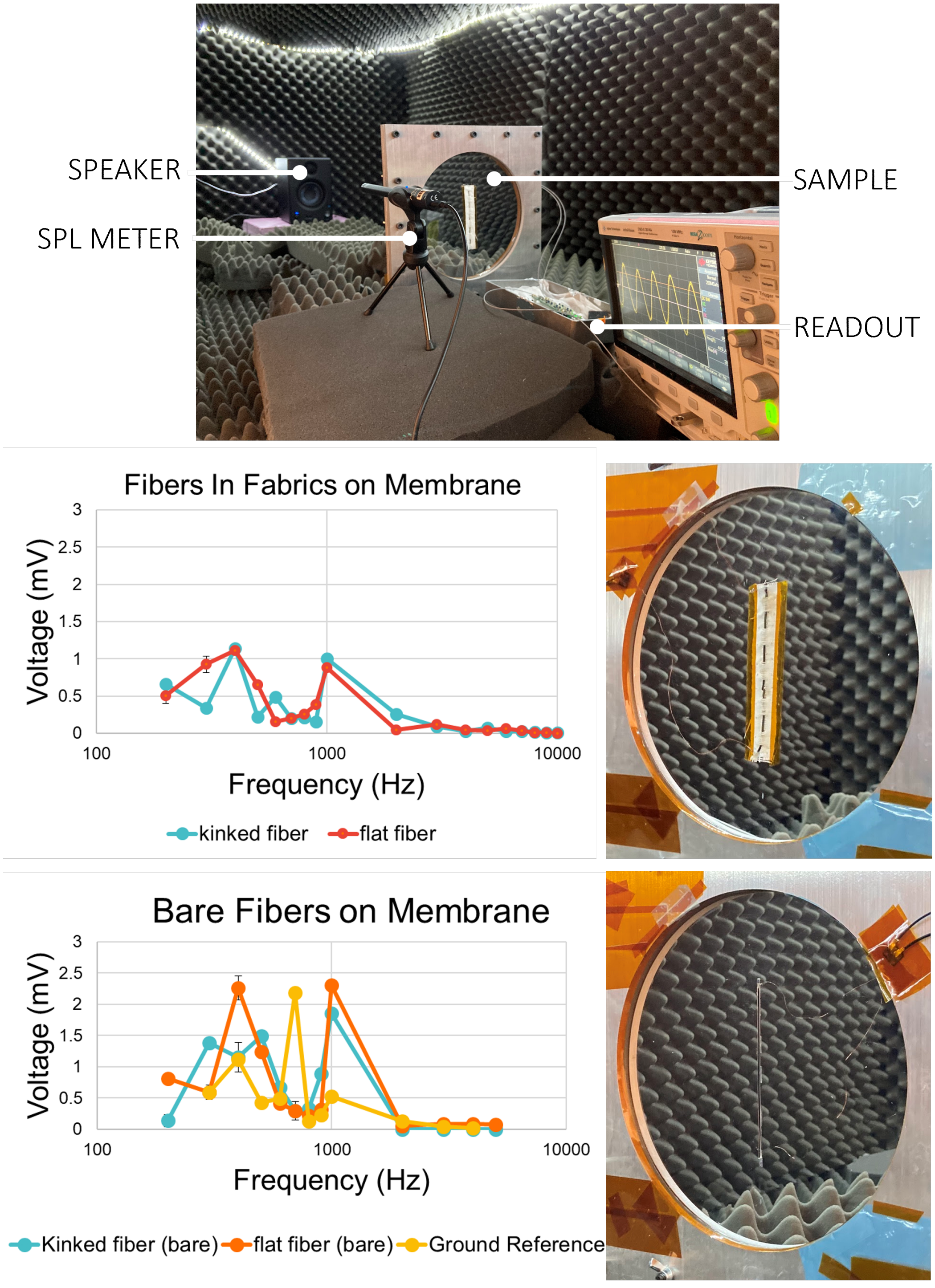

Figure 7-7: Comparison of acoustic transfer function between kinked and flat flight samples against a ground reference

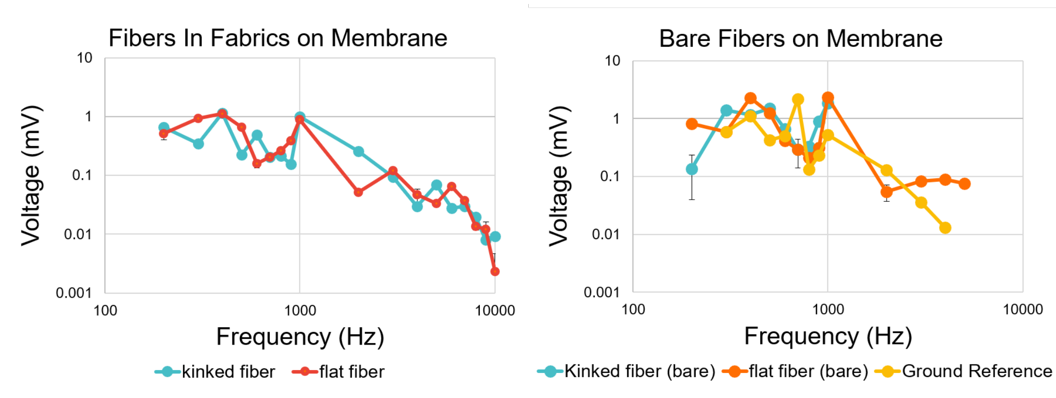

Figure 7-8: Log-Log comparison of acoustic transfer function between kinked and flat flight samples against a ground reference

7.6. Cratering

Here we review the final objective for passive sample deployment - a study of cratering to assess the extent of any damage from genuine space dust.

A gallery of craters detected on the aluminum frame are shown in Figure 7-9.

Prior art includes empirical rules for constraining particle density, velocity, and impact angle, based on these geometric crater properties. Cratering sites can be characterized in terms of a central crater diameter (D_p) and a conchoidal fracture zone (D_{co}) defining the full radial extent of damage. In the current sample, conchoidal fracture zone extends to ~ 150 μm, and central crater size ranges from 10μm-50μm, indicating μm-scale particles incident on the frame. Sample #4 is likely a manmade debris particle such as a paint fleck, and samples 6 and 7 are likely particles incident at highly oblique angles. In the interest of coarse estimates, we turn to a simpler analysis that relies on central crater diameter and crater depth for impactor size and energy estimates.

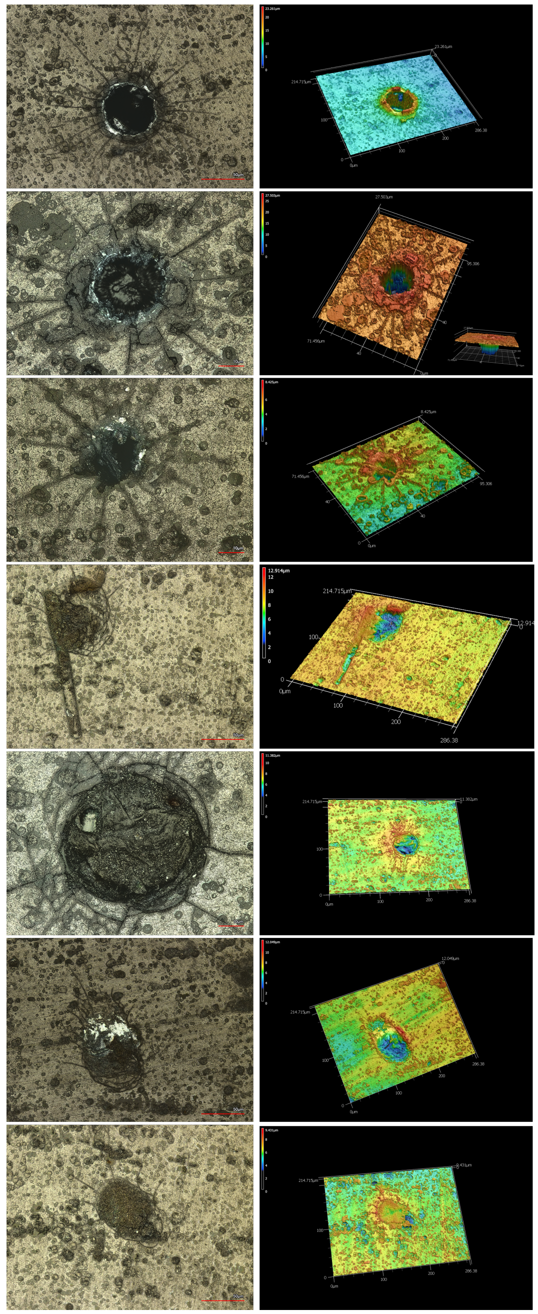

Figure 7-9: Summary of optical and confocal microscope images of strong impact candidates on aluminum frame of sample

Imp. Diam (μm)	RAM Flux (1/yr)	Frame (pred.) (#)	Frame (detected)
>100	0.18	.0435	0
10-100	14	3.38	5
1-10	70	17	2

Table 7.3: RAM facing particle flux by size, in units of 1/year (column 2 reprinted from [41]). Column 3 specific to current experiment, and column 4 is concluded from Table 7.4 to follow

7.6.1. Size Dependent Impact Flux

I refer frequently in this section to [41], which also studies impact cratering on an ExHAM deployed payload of the same dimensions as the on under consideration. Table 7.3 shows estimated RAM-facing flux per year, as well as for the aluminum frame of the current experiment. The exposed aluminum frame, represents 20% of the total exposure area, and the total deployment time was 14.5 months.

By summing the third column, we estimate therefore approximately 20 craters on the aluminum frame. The exposed aluminum frame, which represents 20% of the total exposure area, was manually scanned using confocal microscopy for evidence of cratering. It is substantially easier to identify craters on a rigid target like aluminum, as the damage tends to be one order of magnitude larger than the impactor. Figure 7-9 shows the set of seven impactors identified on the aluminum frame that correspond to high confidence interval impact sites (radial fracturing and crater depth both apparent.)

Hence there is a **factor of 3** delta between observed an estimated values. Not too bad - it's plausible that some micron-scale impactors were omitted, produced weaker signatures, or did not produce radial fracturing, in which case they were not included as strong candidates.

Next, I note in [41] Figure 7, left) that projectile diameter is shown to relate linearly to crater diameter by a factor of $\tilde{3}$ (by contrast, other works suggest one order of magnitude difference, but for the current analysis we rely on this factor of 3 estimate). Equation (4) in this prior work also suggests that crater volume scales with impactor energy by a factor of 0.3. We therefore coarsely estimate impactor diameter and impactor energy for each crater in Table 7.4

	Crater			Impactor Estimate	
Crater #	Diam (μm)	Depth (μm)	Vol. (μm^3)	Diam (μm)	En (mJ)
1	50	23.3	.00098	16.7	3.27
2	20	27.5	.00018	6.7	0.60
3	15	8.4	.00003	5.0	0.10
4	60	12.9	.00078	20	2.60
5	40	11.4	.00031	13.3	1.03
6	70	12.1	.00099	23.3	3.30
7	55	9.4	.00048	18.33	1.60

Table 7.4: Crater properties on aluminum frame, and estimated impactor size/energy

7.6.2. Expected impact sites on fabric

Based on impact statistics on the alumninum frame, we estimate therefore a minimum of 28 micron-scale particles incident on the fabric surface, (or 35 total on the sample). For comparison, JAXA's TURANDOT model predicts 86 particles per 12 months $> 1\mu$m incident on a RAM-facing panel of this size, or 104 over the 14.5 months of the space fabrics exposure [41].

However, on soft materials, the damage site is more likely to scale with the size of the impactor. This, combined with laboratory dust sources adhered to the fabrics and fibers, means that no smoking gun impact sites were identified.

I turned to Van de Graaff laboratory samples to understand what craters on fabric might look like. At one extreme, larger candidates were found via SEM EDX imaging, to be copper and potassium sources. At the other extreme, ripples around small candidates in the SEBS cladding are suspected to be due to a residual optical effects (Both examples are included as an appendix).

We conclude that damage sites on fabric are no greater than 15 microns (the minimum damage site successfully detected on aluminum), as none were conclusively identified.

7.7 . Thermal Performance Considerations for Future Design

7.7.1. Thermal Absorption & Emissivity

We have seen evidence, which we can certainly anticipate, that bare fibers are subject to increased heating. We seek to generally understand the thermal properties of our modified Beta fabric, and to quantify the additional thermal absorption of the fiber. An ET100 emissometer with a 0.520-inch sampling port was used to compare commercial Beta cloth's thermal performance to bare Beta cloth replicas and to a Beta cloth replica with a single piezoelectric fiber inserted. The measurements confirm good agreement between commercial Beta cloth and our Beta cloth simulant in terms of their thermal properties when unmodified. In the case of modified samples, the inserted sensors occupied 25% of total aperture. The introduction of 25% silvered cable fiber by area increased diffuse absorption by around 70%, and the thermally drawn fiber more than doubles thermal absorption. Meanwhile, of heat that is absorbed, commercial Beta cloth will emit up to 92%, and modified samples remain within 10% of this value.

In sum, the fiber samples absorb quite a bit more heat, and emit up to 10% less heat. Because the thermal conductivity of fiberglass is very low ($.04\frac{W}{mK}$), the satellite is likely to develop hot spots at the insertion regions. Since the main operational role of a thermal blanket is to prevent a spacecraft from overheating, there is incentive both to minimize the number of sensors introduced and to apply a white coating with appropriate elastomeric and antifracturing properties. In the case of Beta cloth with metalized Vectran, absorption is only 16% increased, yet emission is substantially reduced - it's possible that a heat sink would be needed in some mission contexts if this material were to be used. I thank MIT Lincoln Laboratory for support in conducting these measurements. Results are summarized in Table 7.5.

	Thermal Absorption		Thermal Emissivity		
	α_{diff}	α_{spec}	ϵ_{20°	ϵ_{40°	ϵ_{60°
Commercial beta cloth [Benchmark]	0.19	1.0	0.92	0.89	0.87
Beta cloth simulant, no sensor	0.18	1.0	0.92	0.89	0.86
Beta cloth + silvered sensor	0.32	1.0	0.86	0.85	0.80
Beta cloth + thermally drawn sensor	0.51	1.0	0.89	0.87	0.82
Beta cloth + silvered Vectran	0.22	1.0	0.58	0.57	0.58

Table 7.5: Absorption and Emissivity for representative samples

7.7.2. Conformal Thermal Coating

A coating must be identified that meets the following criteria: (1) thermally emissive (2) sufficient mechanical flexibility to minimize fracturing (3) sufficient ad- hesion to SEBS & silvered ink fiber claddings.

To ensure that application of a thermal coating is feasible on a flexible material, following discussions with technicians in the aerospace industry, epoxy and silicone based coatings were favored for their mechanical flexibility. Initial tests performed by AZ Technology already indicate that either the AZJ-4020 (epoxy-based) and AZ-83 (silicone-based binder, new product line) are compatible with the thermally drawn fiber, with no chipping, flaking, and good adhesion by visual inspection. In the case of the coated cable, discoloration was observed when coated with AZJ-4020, (indicating a reaction) so AZ-83 is preferred. I applied AZ-83 via dip-coating in a fume hood. The coating is cured in air. Photographs of both fiber types with coating applied are shown in Figure 7-10. These coatings will improve fiber mechanical resiliency in future space-based experiments.

7.7.3. Temperature Dependence of Capacitance

Capacitance will also scale with ambient temperature, and to the extent that there was any reduction in capacitance after spaceflight, might be explained by a hysteretic effect following 7000 orbital cycles. A measurement of this

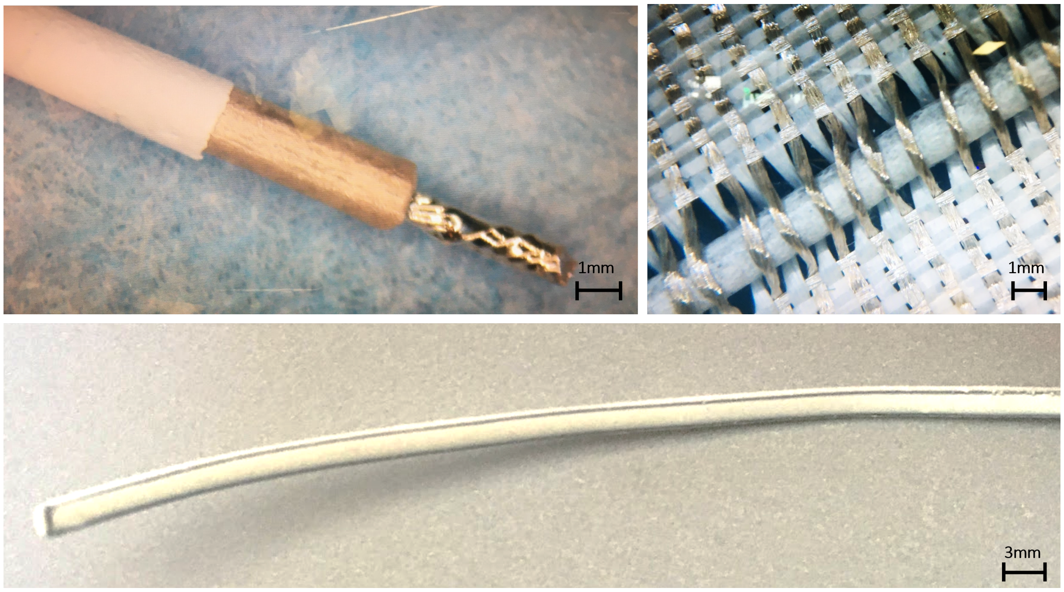

Figure 7-10: (Top) Visuals showing AZ-83 thermal coating on piezoelectric cable. (Bottom) AZ-83 applied to thermally drawn fiber

effect is shown for the thermally drawn fiber in Figure 7-12. Note small error bars. Repeat trials are also shown separately for completely.

7.8 . Conclusion

Referring back to the primary objectives for this passive in-space testing campaign, we identify the following key conclusions:

1. After 14.5 months of RAM-facing exposure to the space environment, the thermally drawn fibers continue to function with the same order of magnitude sensitivity
2. Owing to their thermal properties, the fibers are hotspots on the fabric, undergoing thermal expansion and contraction. Weft insertion as plain-weave helps to minimize buckling relative to other weave patterns. The identified thermal coating will help minimize internal heating in future campaigns.
3. The quilted fabric array was struck by a bare minimum of 28 hypervelocity impacts in space, and no damage in the regime $> 10\mu$m is observed
4. A study of material properties, including thermal emissivity and ca-

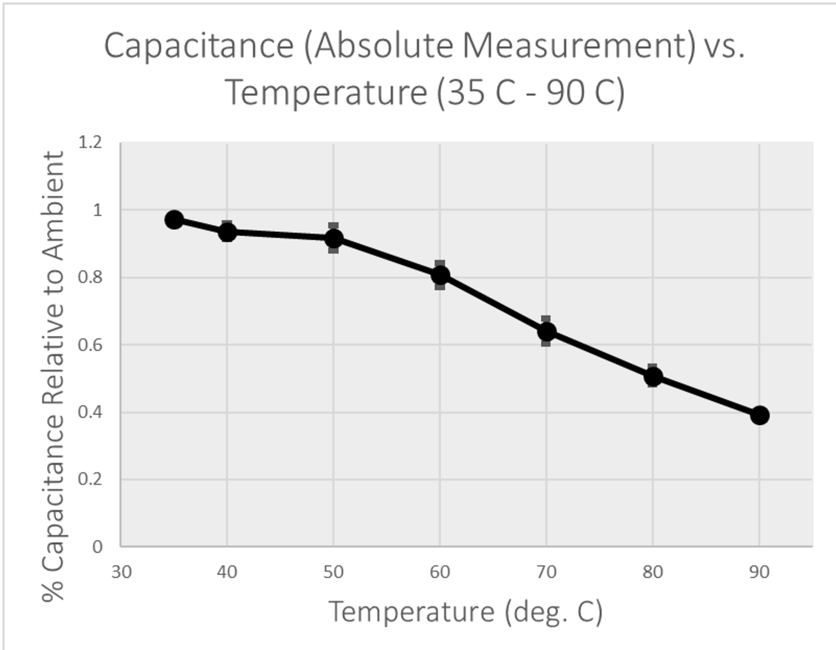

Figure 7-11: Temperature dependence of thermally drawn fiber capacitance

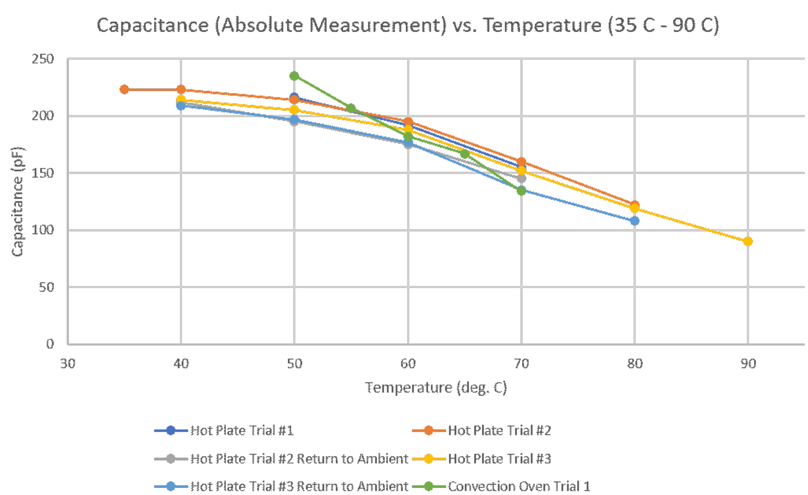

Figure 7-12: Temperature dependence of thermally drawn fiber capacitance (independent trials shown)

pacitance variation by temperature, helps to inform our analysis of the passively deployed samples.

CHAPTER 8

Electrically Active Testing on the Space Station: From Experiment Setup Through Launch

8.1. Objectives

An in-space technology demonstration is underway on the MISSE sample exposure facility. This opportunity came about as a result of a successful grant proposal I submitted to the ISS US National Laboratory. Launch preparation was supported by Aegis Aerospace.

Our principal objective for this exposure period will be to demonstrate space-exposed, piezoelectric fabric as a viable architecture for balancing protective and sensing capabilities in a textile substrate. We will achieve this research objective by periodically characterizing the sensor performance of a modified Beta cloth textile during short term environmental fluctuations in LEO (thermal cycling, solar charge activity) and in response to gradual material degradation effects (atomic oxygen (AO) erosion, outgassing).

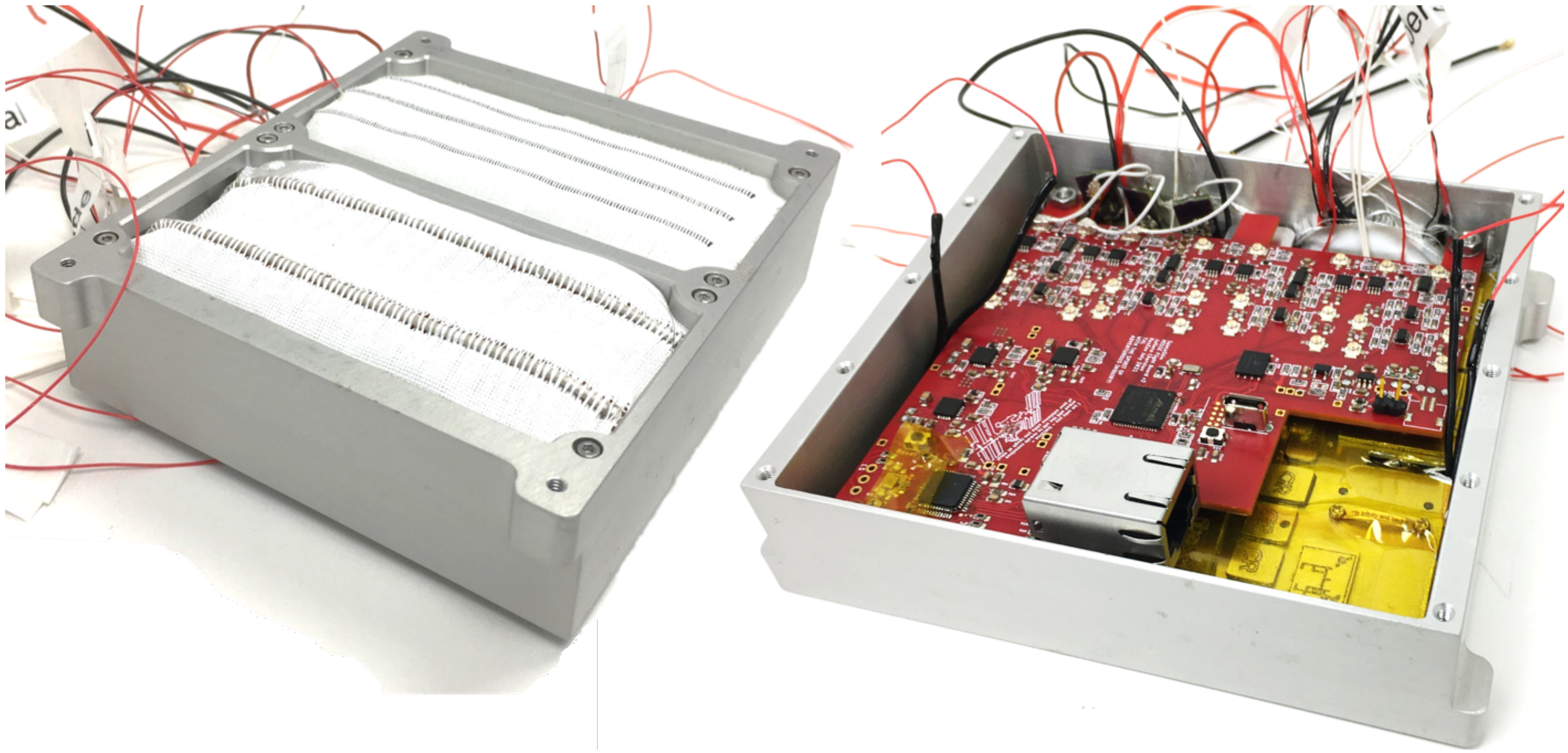

Figure 8-1: Flight Hardware. (left) 2x fabric samples ready for exposure to the space environment. (Right) Backside of sample. Backplate is removed, exposing flight electronics and alumininum shielding

Space deployment is necessary in order to (1) expose the system to all effects of the space environment simultaneously (2) accurately evaluate electronics performance in the relevant charge / noise environment. I reiterate that this deployment is intended as a **technology demonstration**. Should all go as planned, our stretch goal is to then attempt to conduct real science by detecting hypervelocity impactors which, in LEO, fall in a mass-velocity regime that cannot be simulated using ground facilities.

Currently, the project is at NASA technology readiness level (TRL) 4. Namely, as has been described in prior chapters, a Beta cloth substrate containing sparsely weft-inserted piezoelectric fibers and ultra-low power readout electronics has been shown in a laboratory setting to detect micron-scale impactors, with voltage signatures scaling as a function of velocity and as a function of impact offset from the sensor. In addition, certain material resiliency tests have been conducted, including thermal emissivity and low vacuum off-gassing measurements. These ground-based material resiliency measurements are complemented by in-space data from the one-year electrically passive material deployment.

Through an active sensor launch on MISSE, we seek to raise the system's readiness to TRL 7 – that is, 'system prototype demonstration in a space environment', achieved by actively operating sensors in the relevant context over an extended period.

8.2. Experiment Setup: Overview

Two 5cm x 10cm x 2.5cm sensate fabric samples and supporting electronics are deployed for a six-month time duration on the MISSE exterior testing facility. The final flight hardware is shown in Figure 8-1

A custom anodized aluminum sample holder was designed in conjunction with engineers at Alpha Space. The holder has dimensions 10cm x 10cm x 2.5cm and contains two space-exposed windows with a small lip and a divider. A corresponding backplate is mounted with 10x m2 screws and contains a DB9 D-SUB electrical passthrough. Each fabric sample then is secured via: (1) a

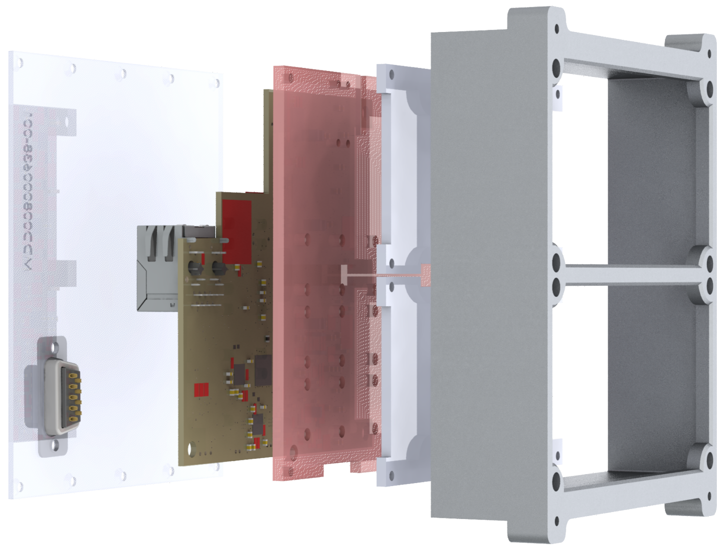

Figure 8-2: Principal structural elements in mechanical assembly of active space fabric hardware

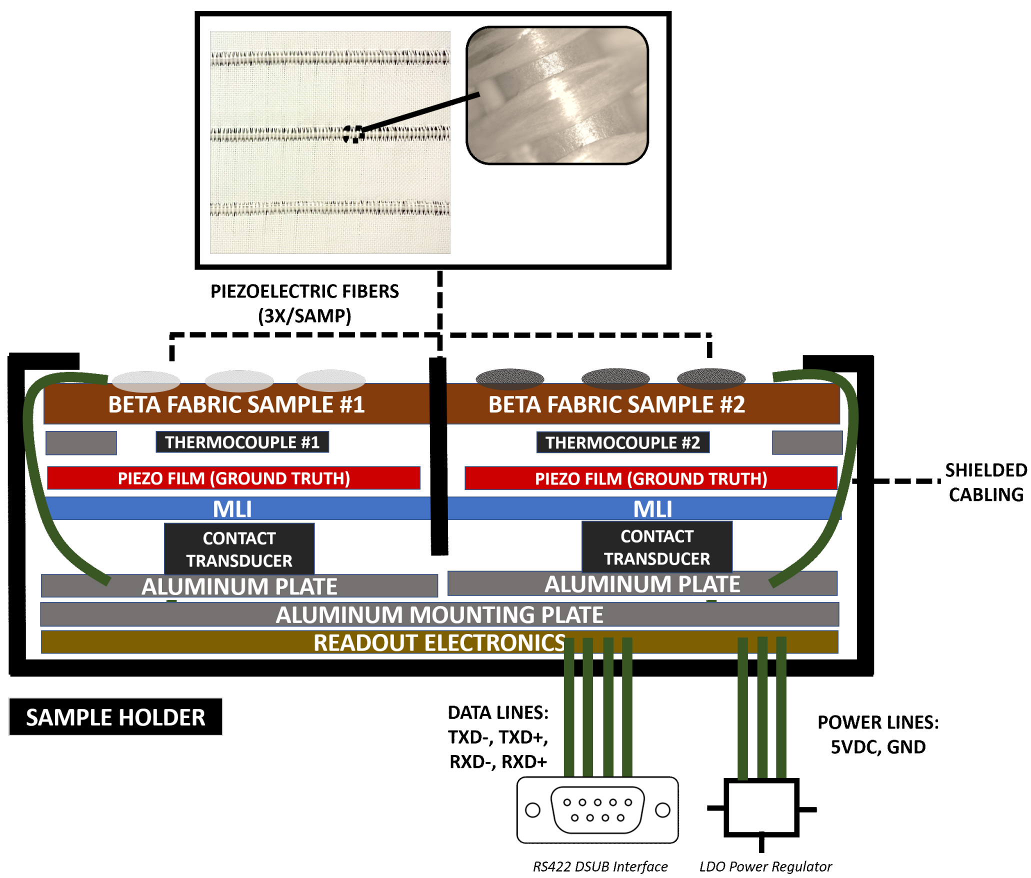

Figure 8-3: Cartoon schematic of internal structure of payload

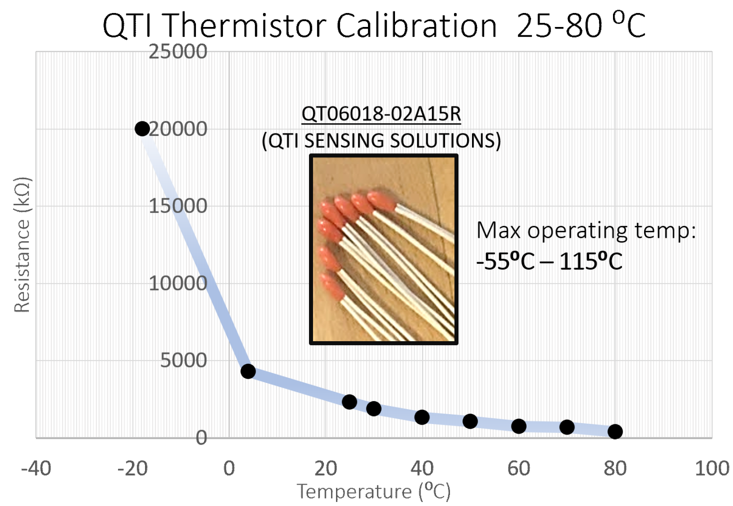

Figure 8-4: Space Qualified Thermistor Calibration

'picture frame style' 3-sided metal frame (2) a half-size backplate with electrical passthroughs. A fullsize plate is then used as a structural backing for the custom readout electronics. These key structural elements of the assembly are rendered in Figure 8-2. Piezoelectric film ground truth references were custom fabricated by PolyKTech.

8.3 . Experiment Setup: Slow Control

Slow control sensors are used for monitoring of hardware that is not time-critical. In this experiment, whereas the fabric sensors and ground truth piezoelectric film must collect data at sufficiently high rates to capture transient impact events, the instrument is also equipped with 3 additional sensing modalities. They are:

8.3.1. Temperature

Part #QT06018-02A15R, an NTC thermistor that is part of a package that is space-qualified, was donated by QTI sensing solutions for use on this instrument. These thermistors are secured to the back of each fabric sample with a thermal adhesive in order to gain a more accurate measurement of the fabric exposure temperature. These measurements are to be cross-referenced with

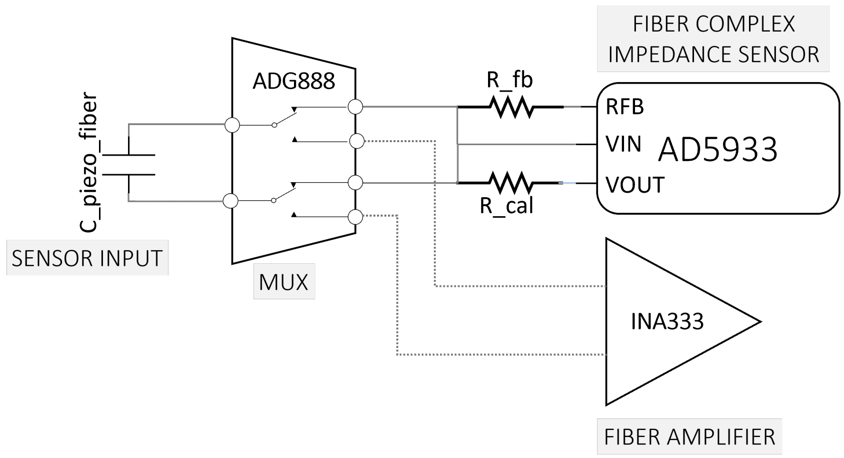

Figure 8-5:

temperature sensors on-board the MISSE facility. These sensors are analog and nonlinear, so ground calibration is required.

We conducted ground calibration using a laboratory refrigerator @4C, a laboratory freezer @-18C, and a hot plate at 4C - 80C. Thermistor resistance measurements are shown in Figure 8-4.

8.3.2. Complex Impedance:

Measurement of the fiber's complex impedance allows for estimates of its resistance and capacitance. Fluctuation in these parameters have been shown to correlate with piezoelectric depoling effects, and would also generally be influenced by any material degradation effects in space.

The AD5933 from Analog Devices is a chip-scale, high precision complex impedance measurement system [1] that is stationed on the primary processor board, shielded by MLI. It excites a source with a known frequency sweep and then uses on-board ADC and DSP engine to compute real and imaginary components of the source's impedance. One of each variation of piezoelectric fiber has been mux'ed to the input of these chips, as shown schematically in Figure 8-5. When the slow control measurement routine is executed, the multiplexer is switched. R_{cal} is factored out of the response.

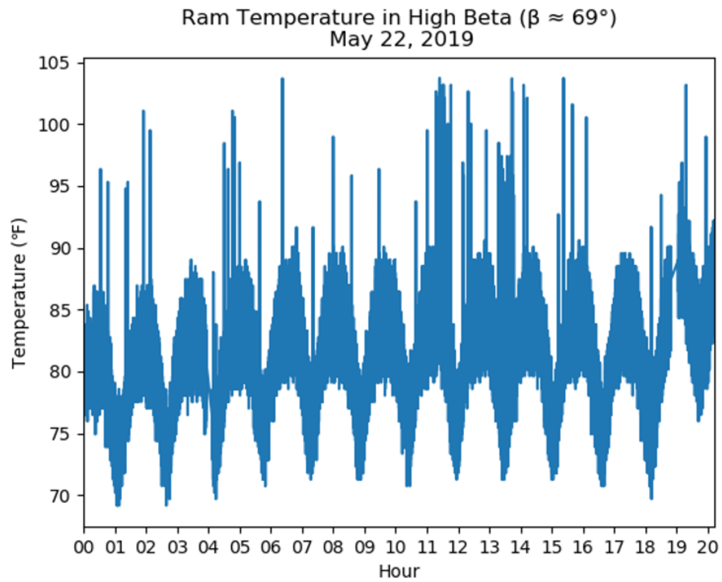

Figure 8-6: Temperature measurements on MISSE RAM face from 2019, provided by Aegis Aerospace as reference

For accurate performance, appropriate calibration impedance and excitation voltage must also be selected. Some key results from our characterization experiments are now summarized.

First, the input capacitance must be known. The piezoelectric cable is spec'ed at 600 pF/m at ambient condition. The 10cm sample used on the flight hardware would thus be expected around 60pF at ambient condition, and indeed is measured at 65pF $\pm$ 15pF. The thermally drawn fiber is measured at 158pF at ambient condition. Additionally, temperature dependence of capacitance was previously reported, offering a sense of the expected modest capacitance swing on MISSE, where temperatures fluctuate from only $20^{c}irc$ to $38^{c}irc$ (Figure 8-6.

Then, I took the following procedure: first I experimented with a leaded capacitor mounted on an AD5933 commercial development board in the range of the fiber samples until identifying a suitable approximate range. Then, I calibrated the flight board using a piezoelectric tab. From the raw |Z| output at a given frequency, capacitance is estimated via $C\ 1/(2\pi f Z'')$ (These results are omitted for brevity).

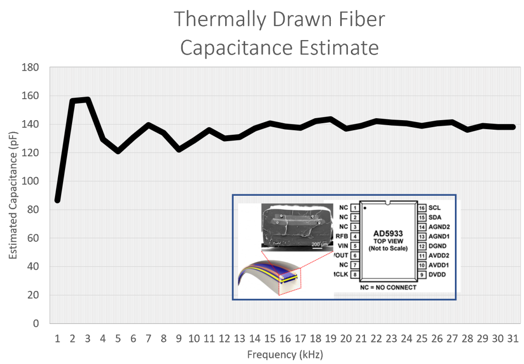

Figure 8-7: Capacitance estimates for thermally drawn fiber using AD5933 complex impedance sensor with 225kOhm calibration resistor

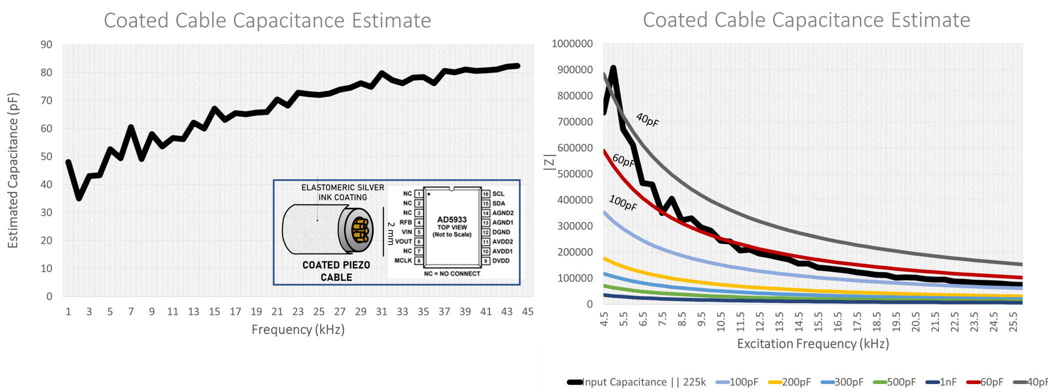

Figure 8-8: Capacitance estimates for coated cable using AD5933 complex impedance sensor with 100kOhm calibration resistor

Finally, the piezoelectric fibers and flight board are directly calibrated with sufficient results obtained using a 225kOhm calibration resistor for the thermally drawn fiber and a 100kOhm calibration resistor for the coated cable. There is some drift in the coated cable owing to its low capacitance. See Figures 8-7 and 8-8.

8.3.3. Haptic Motor Interrogation

Finally, to ensure that the fibers continue to operate, a motorized vibration profile is used as an interrogator.

Initially, a push-pull solenoid was a leading option for this interrogator as a

Fiber	C_s (pF)
Left	157.2/158.2/157.7
Middle	158.8/157.62/157.8
Right	196.6/197.1/197.1

Table 8.1: C_s Ground Measurements for 3x 10cm long Thermally Drawn Space Fibers. (Note that C_p, R_s, R_p are also available but omitted)

method to apply an impulsive force to the fabric. Following inquiries with three manufacturers (Moog for part SDH-.5 XA, Shindengen for part 191, and Ledex/Johnson Electronics for part 50-STA-Mini 1/2″ x 1/2″) two weaknesses were identified to this overall approach. First, all parts would require some mechanical modification to the rod to fit in the maximum 1 inch depth of the payload housing. Second, many parts would require replacement of internal lubricant to a low offgassing variety, a manual process that generally created risk for the motor breaking in space.

A better alternative was then identified - newly available TDK small form factor piezoelectric motors marketed for applications in haptics. This line of parts has several advantages for as an interrogation device. Notably, its small form factor (9mm x 3.75mm x 1.4mm) allows for easy integration. Second, since it is piezoelectric, there are no major moving mechanical parts as in a conventional motor (and, if stored behind MLI, its exposure temperature will remain modest). One downside is that unlike a push-pull solenoid, the force applied to the soft fabric will be predominantly in the transverse direction, and a continuous sinusoid rather than an impulse.

For an 8cm fiber mounted on Mylar in a plastic frame, An 8cm long thermally drawn fiber is mounted on a thin ∼50 micron mylar membrane. Each tip is secured with EpoTek-301 epoxy, and the structure is held in a plastic frame. This test was conducted with no amplification, and suggested that even at lower drive voltages of 10-20V, the motor produced sufficient vibration for detection. Our main takeaway from this early series of experiments was that there was a fair amount of liberty in selecting where to place the motor in the final experiment setup (as one would certainly hope if these fibers are meant to detect such minute impactors !) This experiment is summarized in Figures

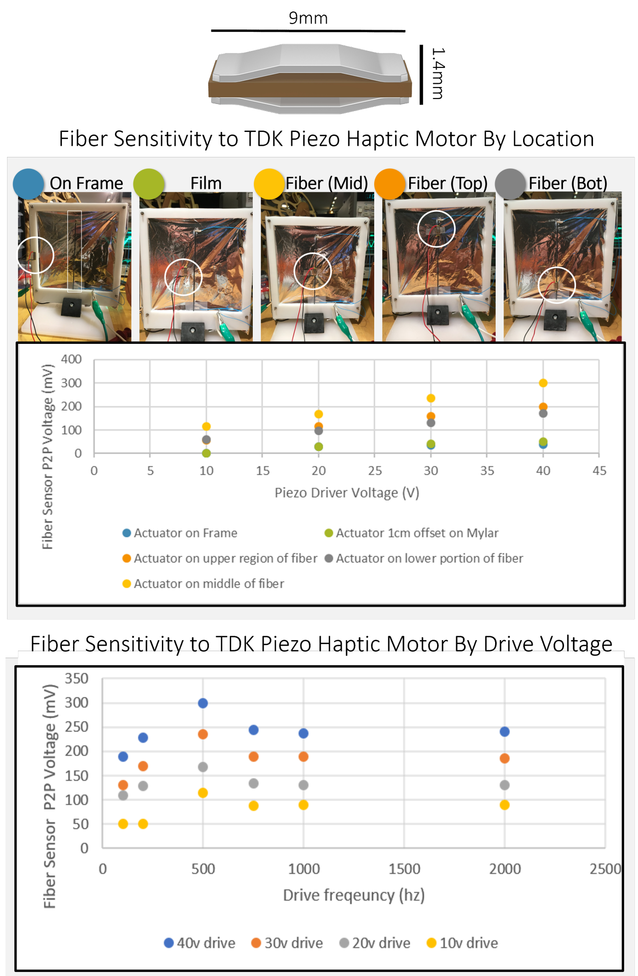

Figure 8-9: The placement of the motor in the chassis is flexible. Ultimately, it was therefore placed behind a layer of MLI.

8-9. In the final flight sample, the motors were mounted just behind a layer of MLI, and interrogated at 6 frequencies and two drive voltages.

8.4 . Thermal Vacuum Testing

A thermal vacuum testing campaign was conducted to verify nominal performance of motors and fibers from -50C to 50C. This test was conducted at the MIT Space Systems Laboratory. I thank Rebecca Masterson, Rakesh Dubey, and others at the MIT SSL for sharing equipment and basic training. I also thank fellow ResEnv RA Fangzheng Liu for joining me in conducting this

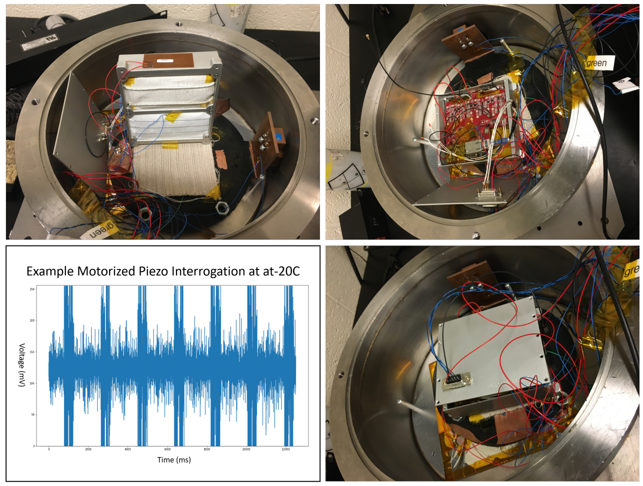

Figure 8-10: Gallery and representative plot from thermal vacuum testing campaign.

test.

Resistive heaters and RTDs were used, along with a bang-bang feedback loop, in order to monitor and control the temperature of the internal PCB and the external fabric.

In brief, this test confirms basic operation of the fiber sensors and motors. At the very end of this sequence of experiments, I pushed the limit and increased temperature to 80C. At this point, we experienced abnormal behavior with one of the coated cables. At the time, I was intending to send a conductive Beta cloth (with silvered Vectran in the weave), which would have served as an ambient charge sensor. However, upon venting the chamber and examining, this issue was traced to shorting between a stray filament of this conductive fabric to the conductive coating applied to one of the piezoelectric fibers, held at half the supply voltage.

In this late stage of the game, I made a decision that the conductive weave was presenting too elevated a risk of electrical shorting to the mission. I swapped this sample out for a sample that contained only fiberglass. However, the fiber sensors in this spare did not have thermal coating applied. It was a trade-off, and a decision made with days left until hardware delivery.

8.5. Reading out Data

8.5.1. Sampling Rate Requirements

Whereas earlier prototypes designed around the TI MSP430FR5969 processor (MSP-430 with ferroelectric RAM), the flight board ultimately pivoted to using a SAMD51 processor for better development support.

For the present application, 8 sensor channels (5x fiber, 2x piezo film, and 1x spare) must be sequentially sampled at rates high enough to allow basic time domain and frequency domain analysis of transient hypervelocity impact signatures. Given that: (1) the analog front end filtering network's cutoff frequency is 20 kHz, (2) spectral content is expected up to around 15kHz, and (3) expected impact signal duration is on the order of 1ms, a bare minimum per-channel sampling rate of 35kHz was chosen as a benchmark. With a Nyquist frequency equal to a maximum 17.5kHz, the system will just barely resolve up to this max frequency of interest. (In practice, it is wise to sample at 3-5x the maximum signal frequency - in this minimum viable criterion, this would be met for spectral content $<$ 10 kHz, where most spectral density lies). Further, a 1ms duration impact signal will contain 100 samples in the time domain, just sufficient for coarse time domain analysis.

8.5.2. Direct Memory Access

To transfer data at the required rates from analog input to Ethernet, direct memory access is required. Direct Memory Access (DMA) bypasses the CPU when digitizing and streaming sensor data. Thus, data is moved directly between memories and peripherals, and faster transfer speeds are achieved. DMA is an advanced feature that requires significant custom configuration. Further configuration requirements include DMA sequencing (which involves CPU-free increment of the sampled ADC channel), two linked lists of circular descriptors (which blends this increment of ADC channels with block memory transfer once the memory block is full) and pingpong buffering (in which half of the DMAC's data transfer bus is filled with new data as the other half is transferred). Code configuring DMAC descriptors, painstakingly adapted from [44], is excerpted below.

Once the Direct Memory Acccess Controller (DMAC) in the SAMD51 is operating, transfer descriptors set by the user are fetched sequentially from the SRAM and stored in the internal memory of the active DMA channel, which then executes the specified transfer.

```
  DMAC->BASEADDR.reg = (uint32_t)descriptor_section;                         // Sets location of descriptors
  DMAC->WRBADDR.reg = (uint32_t)wrb;                                         // Sets location of write back descriptors
  DMAC->CTRL.reg = DMAC_CTRL_DMAENABLE | DMAC_CTRL_LVLEN(0xf);               // DMAC peripheral enable

//**************************************************
  DMAC->Channel[2].CHCTRLA.reg = DMAC_CHCTRLA_TRIGSRC(ADC0_DMAC_ID_SEQ) |     // ADC0 DMAC completed sequence triggers DMAC
                               DMAC_CHCTRLA_TRIGACT_BURST;
  descriptor.descaddr = (uint32_t)&descriptor_section[2];                    // loop descriptor: descaddr points to the next descriptor
  descriptor.srcaddr = (uint32_t)inputCtrl + sizeof(uint32_t) * (16);
  descriptor.dstaddr = (uint32_t)&ADC0->DSEQDATA.reg;                        // INPUT CTRL IS WRITTEN
  descriptor.btcnt = (16);                                                      // Configures beat count
  descriptor.btctrl = DMAC_BTCTRL_BEATSIZE_WORD |                            // Beat size is WORD (32-bits) [HWORD?]
                    DMAC_BTCTRL_SRCINC |                                     // source address is incremented
                    DMAC_BTCTRL_VALID;                                       // Descriptor is valid
  memcpy(&descriptor_section[2], &descriptor, sizeof(descriptor));           // descriptor is copied to descriptor memory address


//**************************************************
  DMAC->Channel[3].CHCTRLA.reg = DMAC_CHCTRLA_TRIGSRC(ADC0_DMAC_ID_RESRDY) |  //ADC0 result triggers DMAC
                               DMAC_CHCTRLA_TRIGACT_BURST;                   // DMAC burst transfer
  DMAC->Channel[3].CHINTENSET.reg = DMAC_CHINTENSET_TCMPL;
  descriptor.descaddr = (uint32_t)&linked_descriptor[2];                      // Set up a circular descriptor
  descriptor.srcaddr = (uint32_t)&ADC0->RESULT.reg;                          // ADC0 RESULT register is read
  descriptor.dstaddr = (uint32_t)adcResult + sizeof(uint8_t) * (1248);           // Move this result to the adcResult array
  descriptor.btcnt = (1248);
  descriptor.btctrl = DMAC_BTCTRL_BEATSIZE_BYTE |                           // Beat size is HWORD (16-bits)
                    DMAC_BTCTRL_DSTINC |                                     //  destination address is incremented
                    DMAC_BTCTRL_VALID |                                    // Descriptor is valid
                    DMAC_BTCTRL_BLOCKACT_INT;

  memcpy(&descriptor_section[3], &descriptor, sizeof(descriptor));           // descriptor copied to descriptor memory location
//**************************************************
  descriptor.descaddr = (uint32_t)&descriptor_section[3];                    // Circular descriptor configuration
  descriptor.srcaddr = (uint32_t)&ADC0->RESULT.reg;                          // ADC0 RESULT register is copied
  descriptor.dstaddr = (uint32_t)&adcResult[1248] + sizeof(uint8_t) * 1248; // .... and moved to adcResults1 array
  descriptor.btcnt = 1248;                                                     // Beat count
  descriptor.btctrl = DMAC_BTCTRL_BEATSIZE_BYTE |                           // Beat size is HWORD (16-bits)
                    DMAC_BTCTRL_DSTINC |                                     // Destination address increment
                    DMAC_BTCTRL_VALID |                                      // Descriptor is valid
                    DMAC_BTCTRL_BLOCKACT_INT;
  memcpy(&linked_descriptor[2], &descriptor, sizeof(descriptor));            // Copy the descriptor to the descriptor section
```

8.6. UDP Protocol / Ethernet Streaming

A WIZNet W5500 Ethernet controller streams data over Ethernet to the MISSE spaceflight computer.

For streaming over Ethernet from the payload to the MISSE flight computer, a

User Datagram Protocol (UDP) is implemented. Unlike Transmission Control Protocol (TCP), UDP prioritizes speed over any sort of handshaking between sender and receiver. As such, packet loss risk must be mitigated. Each packets contain 1248 bytes, both even divisible by 8 (the number of high speed sensor channels) and also below the Ethernet protocol's standard Maximum Transmission Unit (MTU) of 1500 bytes. A bit depth of 8 is selected, which trades amplitude resolution for minimization of packet loss. It was found that an ADC MUX ground reference must be sampled after each sensor read to eliminate sensor crosstalk, halving the effective data rate. It was decided to accept this halved data rate in exchange for preserving signal integrity.

All considered, 480 packets/second is achieved (as measured in WireShark), which, when eliminating ground samples, corresponds to a throughput of 3 MBps = 37.5kHz per each of 8 channels, at 8-bit depth.(For reference, 16-bit depth data, with no crosstalk suppressing ground sampling, achieved 28.8 kHz rates. In other words, inferior signal crosstalk and data rate in exchange for higher resolution. I opted for the former).

Our understanding from discussion with Alpha Space technical team is that this data rate, while modest by Ethernet protocol's standards, is nevertheless tremendously higher than any previous active MISSE payload, and we have now demonstrated the flight computer system to be capable of handling these higher rates without meaningful packet loss. In the future, this rate could be doubled even within the current configuration by eliminating crosstalk between neighboring channels in the ADC's sample and hold circuit.

8.7 . Triggering

Every several minutes, the slow control routine is triggered. DMAC is disabled, and temperature + complex impedance measurements are taken for each sample. then, DMAC is reenabled and the motor interrogation sequence is initiated.

Otherwise, the sample remains in standby mode, waiting for possible external vibration sources (such as impact) to trigger a data write sequence.

Because there is unknown background in the data that will be collected in space (including ambient background and transients), a decision was reached early on in the process to focus on transferring as much data as possible out of the flight payload box and into the external flight computer, where a software trigger can pass or reject data. This decision is justified because: (1) code on the flight computer can be more easily adjusted from the ground, affording more flexibility through the duration of the experiment (2) Access to a more continuous data stream allows a better overall sense of the experiment status, including noise sources. By contrast, an alternative design would have involved a triggering system built into the payload, with a circular buffer to allow sending data just prior to a trigger threshold being met.

8.7.1. Calibration

First, when the payload is first turned on, a calibration routine is run. For k 1248-byte packets, either the mean or the max-min are computed per packet. Recall that the packet is composed of sequenced data from 8 channels. If master channels [m,[...],n] are assigned (such as if one or more channels are defective) then only every mth and nth element is kept in this calibration routine. The average is then computed across k packets. This routine is summarized in Figure 8-11.

8.7.2. Triggering Routine

Once the system is calibrated, the main program routine commences. A set of packets are read in and ground samples are first removed. Then, the list is reduced by user-configured factor for time saving during the triggering operation. By default, 1 out of every 100 samples are kept.In the time domain, this corresponds to sampling 1.6μ s of data out of every 160 μ s. Then, either the mean or the max-min of the remaining measurements are taken, and compared against the previously calibrated `local_threshold` and `transmit_threshold`.

The described trigger routine is kept as simple as possible in order to minimize downtime, as the BeagleBone Black used on the MISSE facility is a single core

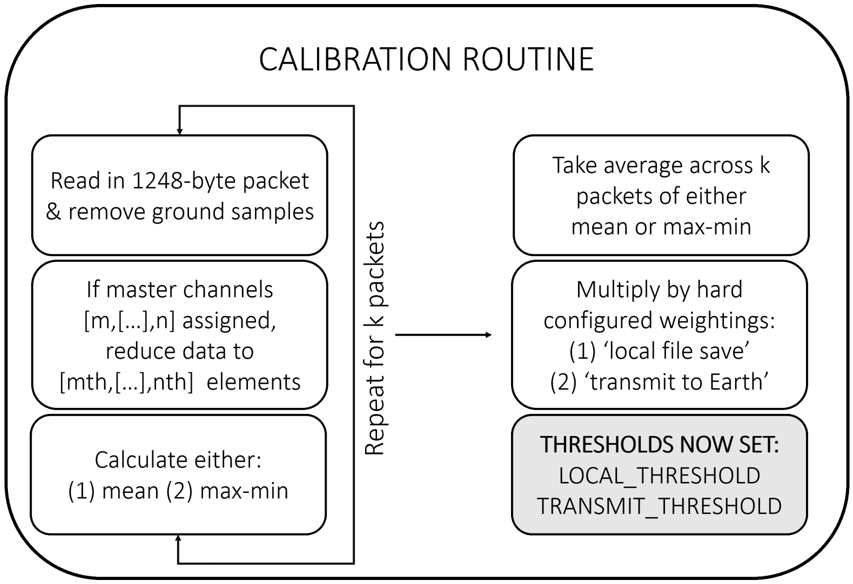

Figure 8-11: Summary of calibration routine for setting triggering thresholds for local file save and remote data transfer to Earth

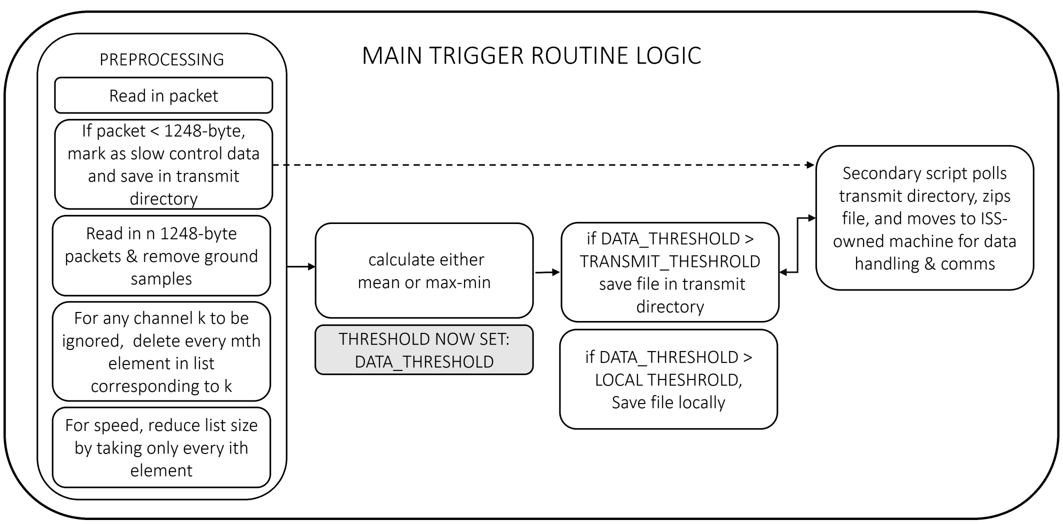

Figure 8-12: Summary of triggering logic on flight computer

processor and cannot support multithreading. Timing operation are used to study the effectiveness of the implemented speed ups.

Finally, if at any point more than 85% of disk space is used, the oldest file is deleted, and if at any point no data streams for 3 minutes, the UDP socket times out.

Once the system is calibrated, the main program routine commences. A set of packets are read in and ground samples are first removed. Then, the list is reduced by user-configured factor for time saving during the triggering operation. By default, 1 out of every 100 samples are kept.In the time domain, this corresponds to sampling 1.6μ s of data out of every 160 μ s. Then, either the mean or the max-min of the remaining measurements are taken, and compared against the previously calibrated `local_threshold` and `transmit_threshold`.

The described trigger routine is kept simple in order to minimize downtime, as the BeagleBone Black used on the MISSE facility is a single core processor and cannot support multithreading.

Finally, if at any point more than 85% of disk space is used, the oldest file is deleted, and if at any point no data streams for 3 minutes, the UDP socket times out.

Files that meet either a local save or transmit to Earth threshold are saved to appropriate file locations. For transmission to Earth, Aegis Aerospace is responsible for moving data from the MISSE flight computer to the ISS central computer, where the data is then queued for transmission. Figure 8-13 summarizes the principal stages of this data pipeline.

In summary, the implemented design choices yield more flexibility and a more holistic understanding of the state of the experiment.

8.8 . Payload Delivery, Launch & Installation

I hosted a preliminary design review for the broader project team in late December, 2020, where I shared CAD renders, high level electronic schematics,

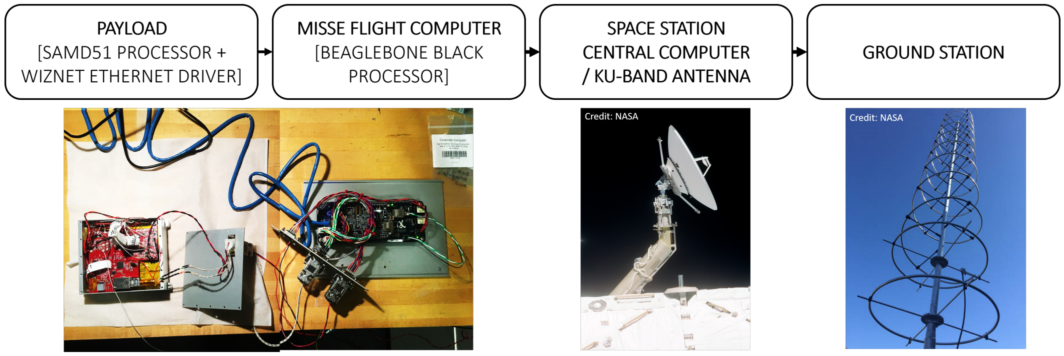

Figure 8-13: Summary of Data Transfer

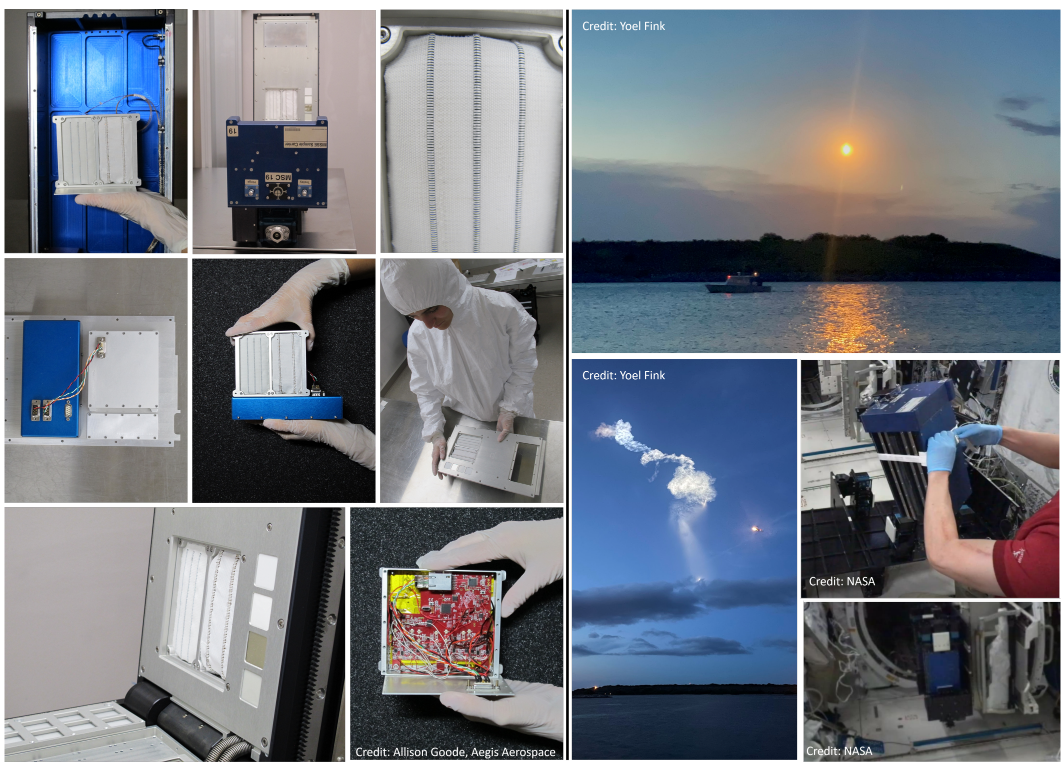

Figure 8-14: Gallery of photographs installing sample into MISSE Carrier, launch, and astronaut mounting in airlock

quantitative assessments (ie/estimated power & data budgets), and preliminary part selection. Payload engineering took place from January, 2021 - September 2021. Two PCB revisions were designed in Eagle and manufactured by MacroFab. A third could not be manufactured in time due to major part shortages in 2021.

The payload was delivered in person to Aegis Aerospace in Houston during September, 2021. The last 1-2 months of development were crunched and expedited. I spent one week in Houston working with Aegis engineers to iron out various kinks, including issues with the space fabrics payload bootup routine, a power issue with the Aegis flight computer interface that required a late stage resistor swap to their machine, and refinement of cabling. Work in Houston also included interfacing with the MISSE computer system, testing the full data pipeline with an ISS computer ground reference, and finally, installation of the payload in the MISSE Flight Carrier. While it was a high-intensity part of the process and more time for testing would have been ideal, the final installation of the payload into the MISSE flight carrier was a celebratory moment. (Sincere thanks to Allison Goode and JC for positive energy and technical support.)

The carriers later underwent thermal and vibration testing at Aegis, and were checked by Aegis only for nominal power consumption during bootup. We do not have confirmation that the payload continued to function nominally from a scientific standpoint following these tests.

On December 10th, the carriers were handed over to NASA. The launch was originally scheduled for 2/19/2022 on board NG-17, and would have been installed in June, 2022. On January 14th, 2022, MISSE-16 was bumped to SpX-25 due to an NG-17 oversubscription, still with a scheduled June, 2022 installation. Due to a series of technical difficulties involving fuel, SpX-25 launch was delayed, and ultimately took place on July 14th. Photos from launch were captured by committee member Yoel Fink and included in the gallery! (Figure 8-14.

On July 27th, Astronauts unpacked and installed two MISSE carriers into the airlock. on July 31st, samples were installed via robotic arm onto the Space

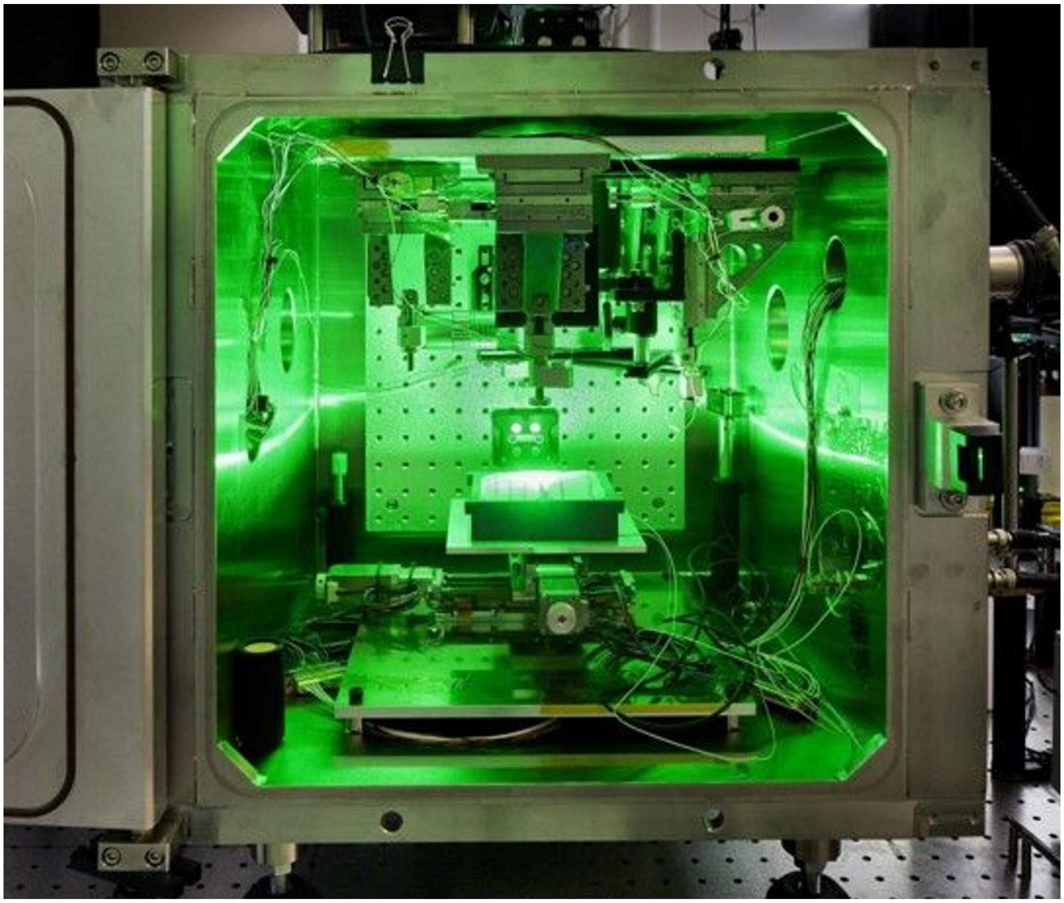

Figure 8-15: Flight Spare mounted in LIPIT vacuum chamber. Laser is pulsed with chamber door open to capture photograph

Station exterior facility. System check is scheduled for August 8th, and first operation occurred on August 10th. Again, a photo gallery of these exciting milestones is shown in Figure 8-14

Figure 8-15 shows the flight spare mounted in the LIPIT chamber.

8.9. Attempt to operate payload in Space

On August 10th (two days before my PhD defense) an attempt was made to apply power to the payload in collaboration with Aegis Aerospace. I prepared a thorough operations flow chart in order to facilitate communication with the Aegis control room (this chart was advised by committee member Prof.

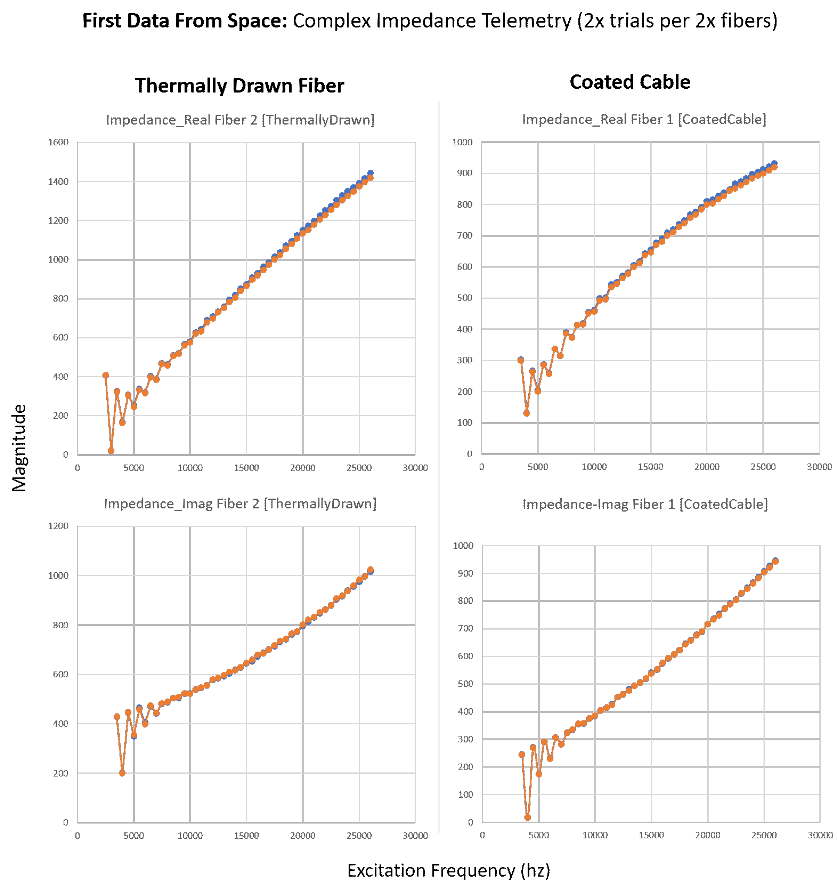

Figure 8-16: From walls of Space Station- complex impedance data (top - real; bottom - imaginary) during 20 minutes of in-space active operation of payload on Aug 10th, 2022.

Yano).

After around 6 hours of technical debugging on Aegis side, we managed to apply power to the payload. Current draw was nominal, and 20 minutes of active operation were achieved. During this time, complex impedance and temperature telemetry were obtained. Some complex impedance data is shown in Figure 8-16, received for one coated cable sensor and one thermally drawn fiber sensor, a symbol for the first data captured from an electronic textile in space.

It remains for Aegis to open the carrier (allowing for photography and for direct space exposure). It also remains to attempt primary high speed data taking, as only slow control telemetry data has been received.

CHAPTER 9

Stitching Everything Together: Conclusions

In this chapter, I will be synthesizing all the information in the preceding results chapters as well as the introductory context into some main takeaways - the grandest conclusions of this work! Plus takeaways for the future.

9.1 . Key Contributions of This Work

I first reprint for easier reference the 'map' of this work.

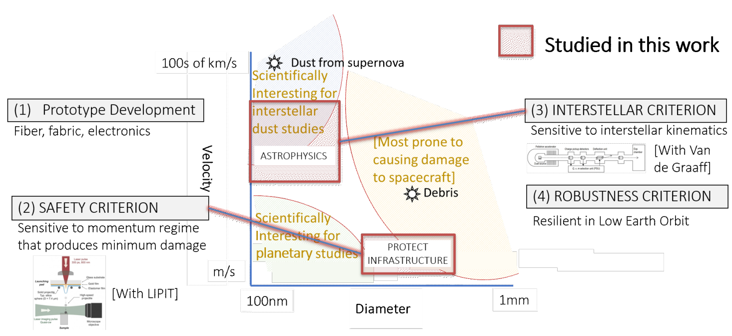

Figure 9-1: Annotated map showing overview of key objectives of this work

I have shown two sensor prototypes - one that leverages the R&D state-of-the-art with regard to materials-level fiber engineering (‘thermally drawn fiber), and one that leverages the commercial state-of-the-art. (‘coated piezoelectric cable’), which will provide an easily distributed tool for allowing designers to experiment.

9.1.1. Conclusion #1:

The Fabric System is Sensitive to Damage at 1cm Weft-Spacing The first key conclusion of this work comes from data taken at the LIPIT accelerator. For both impact on fiber and impact on fabric, the minimum damage-inducing kinematics were first identified (in each case around 300 m/s for a 30 micron steel impactor). Then, sensitivity was shown in this kinematic regime for direct impact, as well as impact 1cm offset relative to the weft-inserted sensor.

Because the fabric system is sensitive to the minimum damage-inducing momentum regime at 1cm weft spacing, we have built confident that *all* damage-inducing impacts would be detected at this weft spacing.

9.1.2. Conclusion #2:

Multimodal Acoustic/Charge Fabric System Can Detect Interstellar Dust

In the low velocity (few km/s) regime, acoustic effects have been shown to likely dominate in the thermally drawn fiber. The presence of an acoustic signature implies greater likelihood of a high mass / low velocity impact signature, or the presence of an ambient/transient noise source, and is thus helpful in discriminating interstellar particles from other impactors.

As acoustic effects roll off, charge sensitivity (mirror charging effects on the fiber’s internal wire conductors) dominates, allowing sensitivity weakly extending to at least 25km/s + 40nm particles.

In a noise prone environment, SNR will be weaker (in comparison to a well-shielded UHV chamber. In a curious extension to the project, I have shown that sensitivity to charge is enhanced by one order of magnitude when adding conductive fur to the target (in comparison to a planar conductor), owing to increased surface area and as well as the fur's 2.5D geometry.

Further, charge production is increased by 1-3 orders of magnitude when using a *goldized* Beta cloth target. Hence, although acoustic wave propagation is less likely in interstellar momentum regimes, electromagnetic effects, which are further enhanced by goldized targets and furry collectors, create a continuous sensing surface for interstellar dust.

9.1.3. Conclusion #3:

(a) Thermally Drawn Fiber Sensor Survives 14.5 months of RAM-facing exposure in Low Earth Orbit

Following extended exposure to environmental conditions in Low Earth Orbit, Fiber sensitivity remains the same order of magnitude, indicating that no or minimal depoling occurred. Some peak shifting in the transfer function is possible, though may be an artifact of acoustic measurement setup.

(b) Plain weave structure and protective coatings help to minimize buckling of the thermally drawn fiber.

The thermally drawn fiber (absent a white thermal coating) creates hotspots in the fabric and likely experiences substantial thermal fluctuation. As a result, without the counter force of warp yarns, buckling occurred. By contrast, fully weft inserted fiber did not buckle. A thermal coating will minimize thermal fluctuations and thus reduce buckling effects.

9.2. Where we go from here

9.2.1. 'Angular sensitivity' challenge

Angular sensitivity is a crucial aspect to a 'textile telescope'. I wish to unite interested designers, physicists, engineers specifically around this challenge. While a dual layer sensor separated by a cm-scale gap is one possible method for achieving angular sensitivity, the challenge I propose is to do so on a single layer, skin-like material that would be more readily adapted on a spacecraft skin. To achieve these simpler designs on a single planar substrate, we must creatively mate fabric form with this desired function. As one example, weak angular sensitivity on an unbiased pile fabric target may have been observed (owing to anisotropies in the impact plasma plume) but more data would be necessary to confirm.

9.2.2. Deepdive into the Astrophysics

I will be doubling down on building awareness in the astrophysics community for the notion of a 'textile telescope', 'fiber-enhanced telescope', and 'fabric astrophysics experiment'. This work will necessarily include continuing to build a stronger quantitative basis for the requirements to discriminate anomalies in the interstellar dust flux, a question squarely in the domain of astrophysics.

9.2.3. Increase appeal to operational and aerospace engineers

We seek to broaden the suite of applications for advanced fabrics in space, ranging from temperature to regolith adhesion, etc.), which will be attractive and inspirational to aerospace and systems engineers during the mission planning phase.

9.2.4. Active Deployment / CubeSat Bonanza

An electrically active deployment is just beginning on the space station. It is too soon to draw meaningful conclusions from this deployment (so far, only 20 minutes of basic telemetry data have been obtained). It is possible that this experiment would need to be repeated. One option for scaling in-space testing of this system is to contact 10-20 CubeSat teams and request 1U of deployment area along with basic power and data. A benefit of our ultra-low power design and essentially flat payload structure is that we might easily fit on a CubeSat.

9.3 . Summary

Have any readers made it here, all the way to the concluding sections of this dissertation? (Shoot me an email at jmc1228gmail.com to make my day!) It's late at night, and I am working through the final night of the post-defense revision of this work. The other day, my fellow ResEnv RA Irmandy suggested adding my favorite quotes or images or sci-fi style narratives to this document. I'd advocated that a narrative even become a requirement for Media Lab theses! So, lightly in this spirit, I wanted to a quote from the walls of my home for the last 10+ years, taken from Zen and the Art of Motorcycle Maintenance by Robert M Pirsig: "The gumption-filling process occurs when one is quiet enough to see and hear and feel the real universe, and not just one's stale opinions of it. That's what I like about the word. In nondualistic maintenance, gumption isn't a fixed commodity. It's variable, a reservoir of good spirits that can be added to and subtracted from. If you have got it and know how to keep it, there is absolutely no way in this whole world that motorcycle can keep from getting fixed... the making of a painting or the fixing of a motorcycle isn't separate from the rest of your existence!" This PhD journey, for me, has been in equal parts a question of my technical growth as an engineer, and my personal growth as a Zen practitioner, and this excerpt reminds me of something I have felt regularly through this process to be true - that there is an equivalency between these two forms of growth. Engraved on the active space-deployed hardware's radiation shield is: "I am learning."

In this work, I have built out a prototype, shown sensitivity to the minimum amount of impactor damage, shown sensitivity to interstellar dust kinematics, shown an understanding of resiliency to the space environment. Just a few weeks ago, when we applied 30 minutes of power to this fabric system and collected basic telemetry data, our project **successfully deployed the first Electronic Textile in space!**

CHAPTER 10

Feeling Through Spacesuits and Crawling on Space Webs: A Bold Future for Space Textiles

In this chapter, I share a much broader vision for the future of advanced textiles in space. While my primary personal interest lies in tools for fundamental physical inquiry, I also wish to increasingly blur the lines between infrastructure for science and infrastructure for human experience. In this chapter, I share a suite of concepts that each leverage advanced textiles. Development stage ranges from basic concept to simulation to early prototype. Each is a 'tool for humoring the universe'[1]

10.1 . Textiles + Crawlers on Low Gravity Bodies

The following sections are excerpted from two of my publications. For more detail, see [13] and [10].

[1]As phrased by my design mentor Neri Oxman.

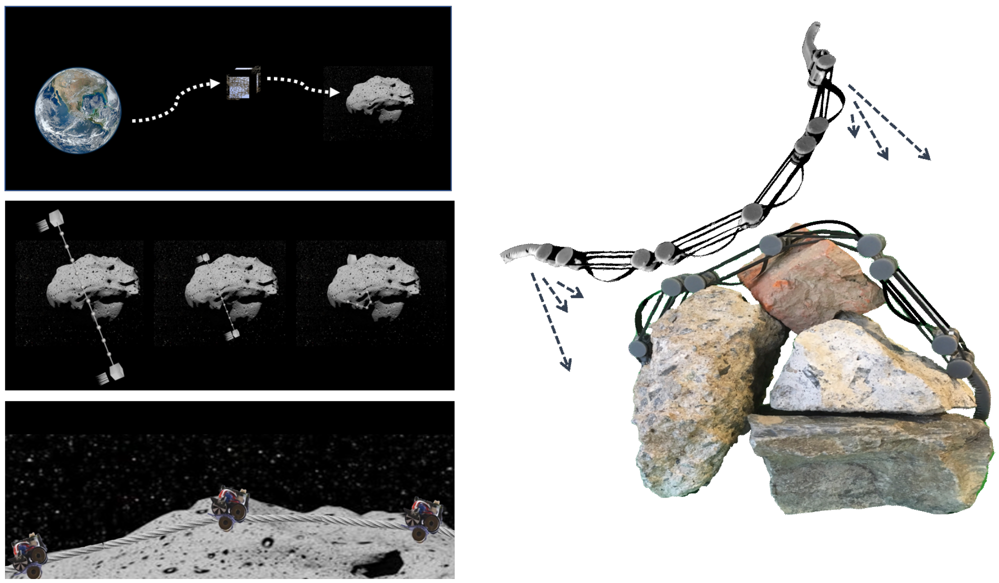

Figure 10-1: Left: concept of operations for net-like lander. Structure is stowed in small satellite, launched at body of interest, and once adhering to structure can serve as foundational infrastructure for e.g. crawling robots. Right: Concept of operations for Grapplers: arrays of bistable pinching elements scattered sparsely or densely around the net are able to pinch to local features in the terrain.

Suppose, thinking beyond advanced textiles on spacecraft, we imagine a sparser mesh that envelopes a low gravity body (Figure 10-1). This net also serves as infrastructure for a network of tiny crawlers that move across the net's surface for applications in in-situ distributed sensing and far-future industrial manufacturing. The 'Space Webs' concept was submitted as a NIAC proposal in 2017 and received a 'green' rating.

When considered as a low-gravity foundational infrastructure, mesh landers are loosely inspired by the use of *geotextiles* on Earth - large-scale permeable fabrics woven into the ground to strengthen soil, armor sand dunes, or allow planting on steep slopes. They are integrated into the soil or root systems of vegetation in a textile-and-Earth combination, preserving existing fragile landforms and creating entirely new landscapes. It is now common practice for civil engineers to include geotextiles in city design, and the scale of these functional textiles is often enormous [47]. While geotextiles are designed with Earth's gravity-driven environmental effects in mind, the general principle of facilitating surface development using a textile-based structural support layer remains provocative.

10.1.1. Crawler with Multispectral Imaging Payload

Development Stage: EARLY PROTOTYPE

Testing notes: [preliminary tested with genuine meteorite samples]

As an initial application area, I considered deploying a network of distributed spectrometers across the surface of an asteroid for high spatial resolution material characterization. I developed a first prototype for a rope crawling mechanism, a cousin to fabric crawlers developed in Responsive Environments. I also conducted a study of a new-to-market chip-sized spectroscope as a candidate sensing payload for the crawlers. I gained access to a collection of genuine meteorite samples from Harvard and MIT's collections, scanned these samples with the candidate spectral imager, applied a set of spectral endmember selection algorithms and unmixing algorithms, and found some evidence for the sensor's ability to discriminate between high-iron and low-iron genuine meteorite samples obtained from Harvard and MIT collections.

Sensor	Spectral Range	Size (mm)	Price**
Texas Instruments NIR Spectrometer	1824 bands in 900-1700 nm range	33 × 29 ×10	$999
Ocean Optics Spark-DET-VIS	~80 bands in 380-700 nm range	18 x 10 x 0.3	$309
Hamamatsu C12880MA Micro Spectrometer	~288 bands in 340-850 nm range	20 x 13 x 10	$245
PixelSensor	8 bands in 425-850nm range	46 x 21 x 5	$195
Nano Lambda NSP32	4 products: ~20-40 bands in (390-760nm, 600-1000nm, 850-1050nm, 400-1000nm)	18 x 7 x 6	$148
AS7263	**6 bands from 610 - 860nm**	**5 x 5 x 2.5**	**$8**

**Prices quoted for sensors, not for dev kits

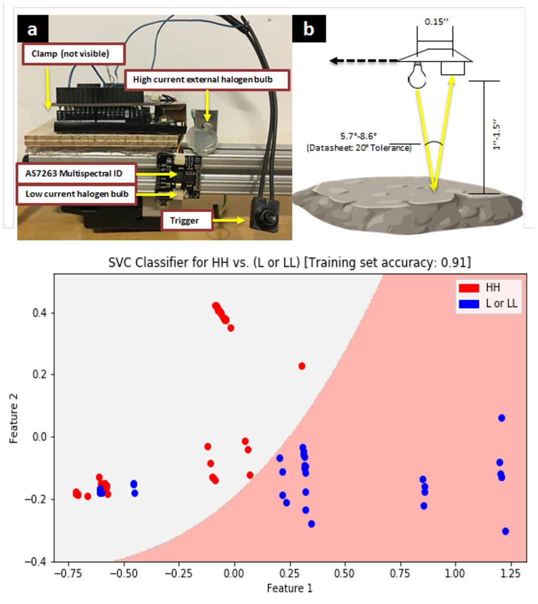

Figure 10-2: New-to-market chip-scale spectrometer payload shown to discriminate between meteorites with high and low iron content.

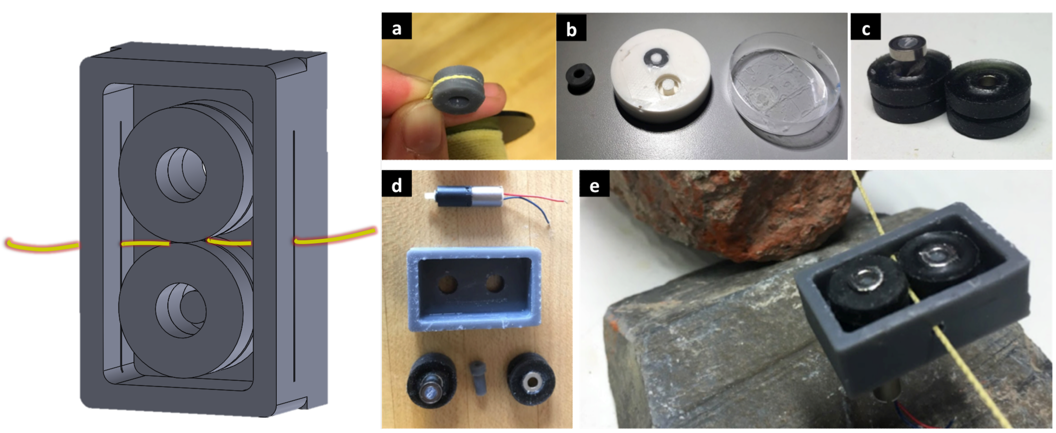

Figure 10-3: Rope Crawler Prototype

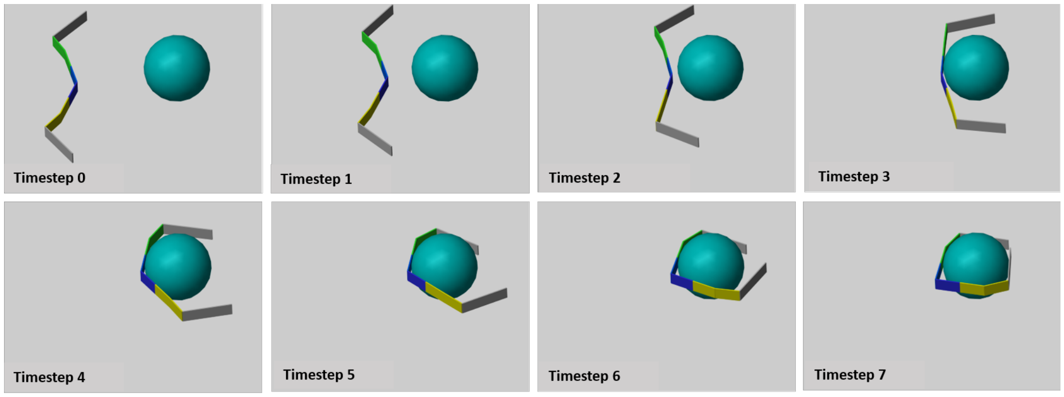

Figure 10-4: Three pinching elements, end effectors (note that an asymmetric impact point causes grappler element responses that are asymmetric in time)

10.1.2. Bistable arrays for low gravity adhesion

Development Stage: SIMULATION, EARLY PROTOTYPE

Testing notes: [preliminary microgravity flight testing. Paul Strohmeier contributed to this work]

Whereas prior art focuses primarily on anchoring and hopping mechanisms, my work also evaluates a novel mission architecture in which chains of bistable pinching elements called grapplers are used to adhere net-like infrastructure to low gravity bodies. Unlike single-point-of-contact landers, a net that is successfully adhered to an asteroid may serve broad and flexible use in the exploration of small bodies. For example, it may constitute infrastructure to enable locomotion of a swarm of distributed crawling sensors and actuators for high resolution study of the body's interior structure and surface properties. It may also serve as a foundation onto which larger scale sensing and communication structures can be built over time. Finally, it may serve as a series of hand holds used by astronauts to maneuver around the body.

Microgravity flight testing[2] of a representative Grappler prototype demonstrates the tolerance of a bistable chain to variable impact conditions and ter-

[2] This flight was organized and supported by the MIT Space Exploration Initiative, during the earlier phases of my degree.

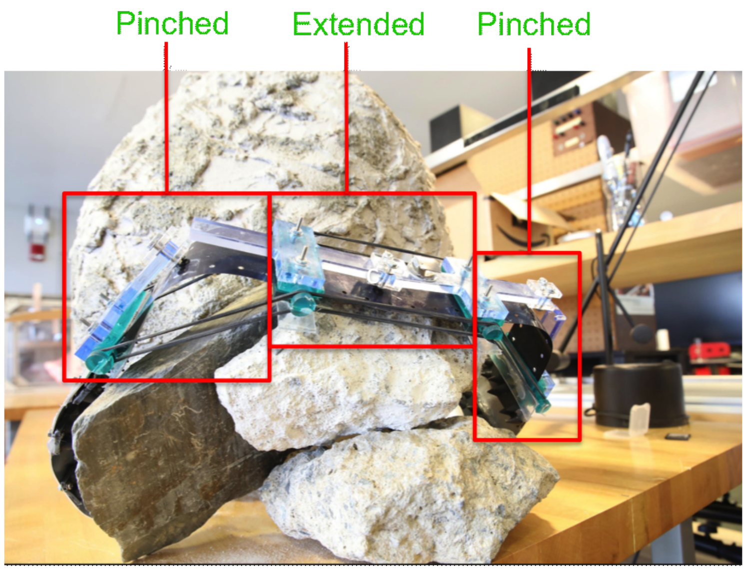

Figure 10-5: Primary Grappler prototype with n=3 bistable elements and curved end effectors

rain contours owing to the inherent adaptivity of the chain's pinching configuration- for a chain of n bistable elements, 2^n pinching configurations are possible. These pinching elements can be integrated sparsely or densely into net-like infrastructure. I also developed a supporting computational model in Simulink.

10.2 . Advanced Textiles for Feeling Through Spacesuits

Development Stage: CONCEPTUAL PROTOTYPE

Testing notes: [Basic ground testing with robotic arm. Syamantak Payra, Irmandy Wicaksono, and Valentina Sumini contributed to this work]

This section is excerpted from a publication that I conceptually spearheaded, and to which I was a contributing author. For more detail, see [57].

The direct engagement of explorers with their proximate environment is crucial for promoting both maximum situational awareness and vivid sensory feedback. However, the protective pressurized spacesuit worn by astronauts creates a thick boundary between the wearer's biological skin and the suit's space-exposed surface, isolating and impeding the wearer from engaging with

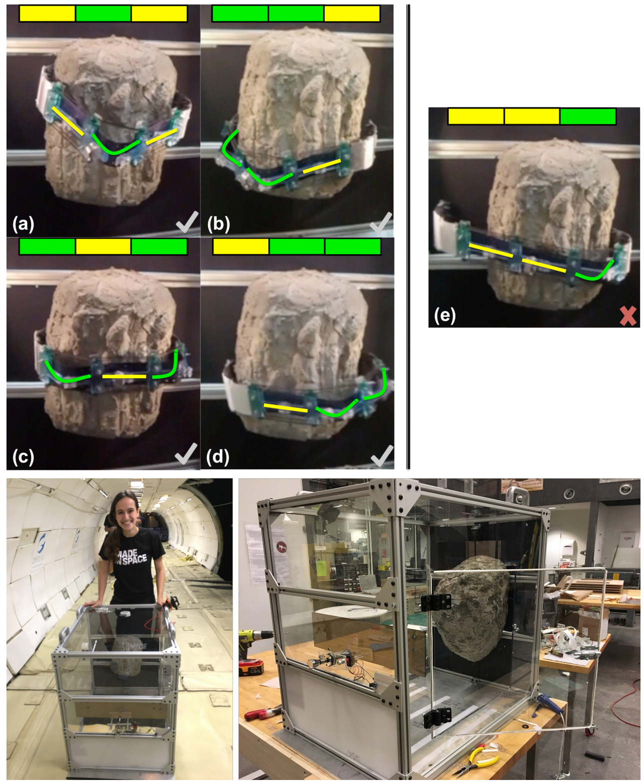

Figure 10-6: Results from five grappling trials conductive in micro-gravity conditions. Green overlay is used to indicate pinched nodes, and yellow overlay is used to demarcate flat notes. (a)-(d) constitute successful grappling configurations whereas (e) constitutes failed grappling. Also shown are photographs of the experiment apparatus onboard a microgravity airplane.

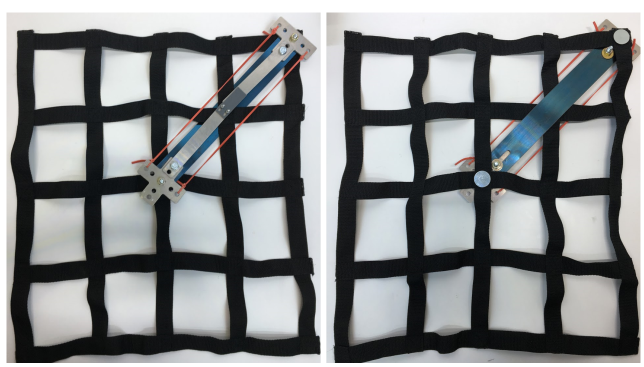

Figure 10-7: Single grappler element incorporated in net. (Left) Top view. (Right) Bottom View. Pinching elements can be incorporated at any scale, including materials-level. They can be sparsely or densely distributed.

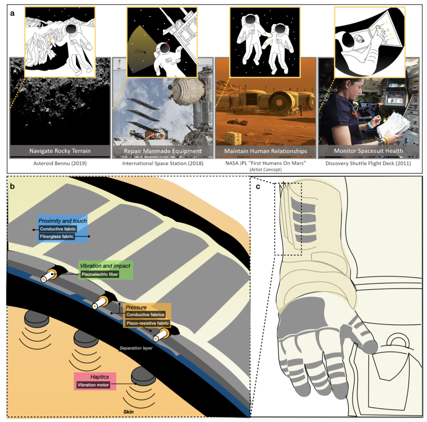

Figure 10-8: (a) Representative environments encountered by astronauts informing the current study, and b,c) exploded view of multi-modal e-textile spacesuit skin. Sketches by Irmandy Wicaksono

the intuitive sensory and tactile functions of human biological skin.

SpaceTouch is a conceptual application area for fabric sensing on the spacesuit exterior. An implementation overview and a set of broad potential use cases for this concept are summarized in Figure 10-8a. This spacesuit composition enhances the safety of pressurized suits while reinstating a biological sense of touch. To do so, touch input from the protective suit's exterior layer is detected, identified, and mapped to a haptic feedback system on the wearer's biological skin, 'conducting' sensory data from the exposed skin to within the spacesuit.

As illustrated in Figure 10-8b-c, the SpaceTouch multi-modal design consists of three main layers: an outer proximity and touch sensing layer containing conductive patches integrated onto a base fiberglass fabric, vibration and impact-sensitive piezoelectric fibers woven into channels in the fiberglass fabric, and multi-layer pressure-sensitive piezoresistive fabrics just below the outer layer. Capacitive coupling between an object as a virtual ground and charged conductive patches reflects touch and near-proximity. An intermediary foam layer separates the aforementioned layers from the inner layers of the spacesuit. An actuation layer that is coupled to the skin can provide closed-loop haptic feedback based on the sensor data. Our fully-textile-based sensor design and integration will enable future realization of single-layer capacitive, piezoresistive, and piezoelectric e-textiles that can sense and respond simultaneously to a variety of stimuli.

To evaluate this design, textured end-effectors on a robotic manipulator are brought in contact with the fabric sensor suite in order to qualitatively assess that actionable environmental data can be collected and eventually transmitted through haptic interfaces to wearers. This test setup is shown in Figure 10-9, along with a representative result comparing piezoresistive and piezoelectric sensor signatures. UROP Syamantak Payra led this work, supervised by me.

10.3 . Plasma RF Sensing

Development Stage: QUANTITATIVE ASSESSMENT + LIT REVIEW

This work is excerpted from one of my publications. For more detail, please see [12] As an extension beyond plasma charge sensing (introduced previously in our Van de Graaff studies), we now consider integrating an antenna into a spacecraft skin for sensing hypervelocity impact plasma RF emission. At speeds above 18 km/s, the plasma substantially ionizes and will have a tendency to expand until collisionless (at lower velocities, recombination will be favored). In this >18 km/s velocity domain, radio frequency emissions have also been detected, with detection rates approaching 75% as impact speed approaches 72 km/s. However, at speeds below 18 km/s, recombination dominates and RF emission is rarely detected. These velocity regimes are summarized graphically in Figure 10-10.

This RF emission phenomenon was first observed by Bianchi et al, and the pulses generated by dust impacts were first discovered using electric field measurements in the vicinity of Saturn's ring plane by the Voyager spacecraft. There is no firm consensus on the physical mechanism for this RF emission, and some discrepancy in the literature regarding conditions required to produce it, though it appears to require substantial ionization of the plasma and may require a electrically biased target object. The emission is presumably related to charge motion in the plasma, and some type of instability only present under certain conditions. According to Close et al., the RF emission is thought to present once the collision frequency and plasma frequency are equal, at which point surface electrons are able to separate from the plasma and oscillate significantly in-phase.

To detect RF emission from plasma at 315 MHz, we first consider integration of an array of patch antennas into the blanket. In the domain of wearable communication, designers often opt for patch antennas due to tolerance to bending, isotropic antenna response in the exposed semisphere, and ease of textile integration. For example, [43] provides a reference on designing all-textile patch antennas with microstrip feeds that can tolerate a bending radius on the order of 40mm. This antenna is manufactured using plated yarn conductive fabric as a ground plane and woolen felt as a spacer. In our case, Beta cloth itself, with dielectric constant 2.6, can be used as the antenna's substrate and conductive yarn can form the antenna's ground plane.

Using equations and design guidelines provided in [5], a 315 MHz antenna requires a patch geometry of 30cm x 35cm x 0.2cm. Traditionally, patch antennas are not used at such low frequencies due to size constraints. To assess size constraints in this application area, we must estimate required antenna spacing.

To coarsely estimate this parameter, the expected antenna receive power must be compared to the estimated antenna sensitivity. First, to relate electric field strength to RF signal strength, we extrapolate from the previously cited measurement of 1.9 v/m field strength at a distance of 30cm from impact for a 1.4e-15 g iron particle traveling at 40km/s. Based on the relation:

$$\frac{P_T}{(4\pi d^2)} = \frac{E^2}{Z_o} \tag{10.1}$$

where Z_0 is the characteristic impedance of vacuum: d is distance from signal emission point, E is electric field strength and P_t is transmitted power, the transmit power can be calculated as 10.8 mW for the given impact conditions. Assuming that power falls off as d^2, and, very speculatively, that each antenna can detect 1mW signals once the noise floor is considered, then **antenna spac-**

ing of about 1-2 meters can be tolerated for the given particle mass and velocity. However, this calculation is not explicit about the dependence of antenna aperture on frequency.

So, more generally, we derive the following relationship between receive power and distance from impact for a narrowband antenna as a function of distance. Beginning with:

$$E \quad \frac{kq}{d^2} \tag{10.2}$$

and using an estimated mv$^{3.8}$ power law relationship for charge production, we can write:

$$E \quad \frac{kmv^{3.8}}{d^2} \tag{10.3}$$

The Friis transmission formula is then used to relate power to frequency and distance from source:

$$P_R \quad \frac{P_T G_T G_R c^2}{(4\pi df)^2} \tag{10.4}$$

Finally, power is related to electric field strength via Equation 10.1. Using the above relations, we write receive power as a function of mass, velocity, distance from impact, and frequency:

$$P_R \quad \frac{k^2 m^2 v^{7.6} G_R c^2}{(4\pi)^3 d^8 Z_0 f^2} \tag{10.5}$$

This equation can be used as a general relationship between antenna receive power and distance from aperture for the plasma RF emission from an impactor.

Based on these approximate calculations, a 30cm x 30cm patch antenna is likely tolerable, as antenna size antenna spacing. However, a smaller antenna design can be achieved by using a 1/4 wave trace meander antenna, which for instance could be embroidered onto Beta Cloth using conductive yarn, though bending sensitivity would have to be taken into account. Simple models and antenna patterns were generated in MATLAB for each antenna type and showing in Figure 10-11. Because both the plasma origin and receive antennas will be on approximately the same plane, it is most important is to ensure reasonable antenna sensitivity at low angles relative to the x-y plane (though the plasma may continue to emit RF as it travels). The antenna receiving pattern for a patch antenna design is fairly isotropic in its space-exposed semisphere, and a gain of approximately 0 to 5 dbi can be expected at small angles. Conversely, the gain of a meander antenna is likely to range from -15dbi to -5dbi for small angles.

10.4 . 'Skin and Eyes' Actuation Scheme

Development Stage: CONCEPT

Once damage is detected on a spacecraft skin, an actuation scheme is needed for further analysis and initiation of repair scenarios. I propose a coordinated response between a LEO spacecraft's outermost skin and a suite of free-flying proximity imagers that further assess damage. A spacecraft or habitat thus self monitors, with fabric-based crawlers subsequently tasked for repair jobs. This intuitive concept was inspired by my work at the time on wafer-scale satellite engineering in conjunction with Prof. Dave Miller and MIT Lincoln Laboratory. (On this project, I primarily contributed to the development of electronics for an RF-beacon payload for atmospheric sensing). The 'Skin and Eyes' concept was also submitted as a NIAC proposal in 2018.

In brief, a habitat's protective thermal blanket is redesigned to simultaneously operate as a dense sensate skin. Following an impact event, the skin strategically summons optical nodes for further characterization of damage. This aerospace architecture emulates the coordinated nature of a biological pain response in the sense that we reflexively mitigate uncertainty in what is felt on our skin by summoning the attention of our eyes. Like neurons in the finger tips and retina, salient features are then extracted by the habitat's skin and eyes before routing data to a centralized processor.

This work existed predominantly in conceptual phase, with some early prototyping around rope crawer mechanisms. Fellow ResEnv RA Fangzheng Liu now realizes space resilient crawling robots in the AstroAnts project.

10.5 . Summary

We have summarized preliminary work conducted on advanced space fabrics for (1) foundational net-like infrastructure on asteroids (2) net crawling bots (with emphasis on spectroscopy) (3) haptics systems on spacesuits. We have also summarized some lighter explorations extending the primary spacecraft skin concept, including (4) ‘Skin-and-Eyes’ and (5) Fabric antenna for RF impact plasma charge sensing.

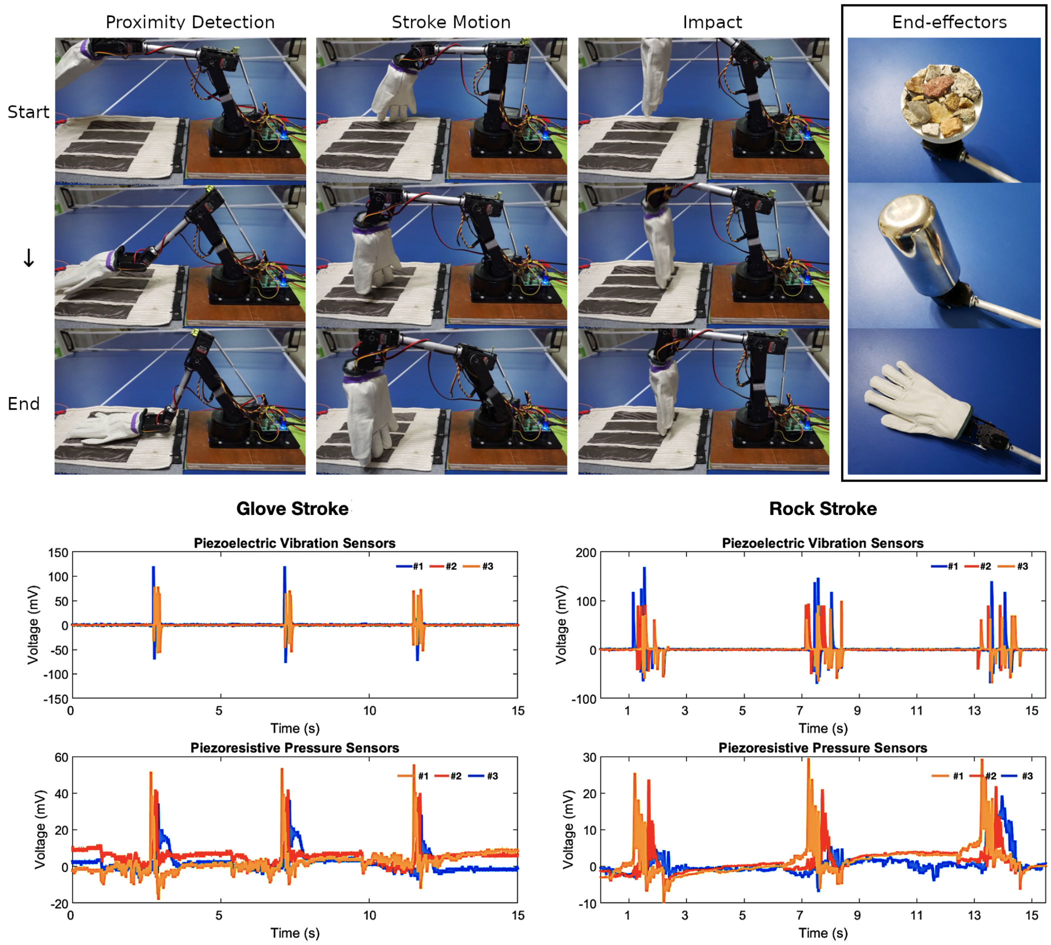

Figure 10-9: (Top) The robotic test setup with glove arm motions (left) and end-effectors (right). (Bottom) Comparison between piezoelectric and piezoresistive response for a glove stroke motion vs. rock stroke motion. While the piezoresistive data is qualitatively similar, the rocky surface induces longer duration piezoelectric ringing.

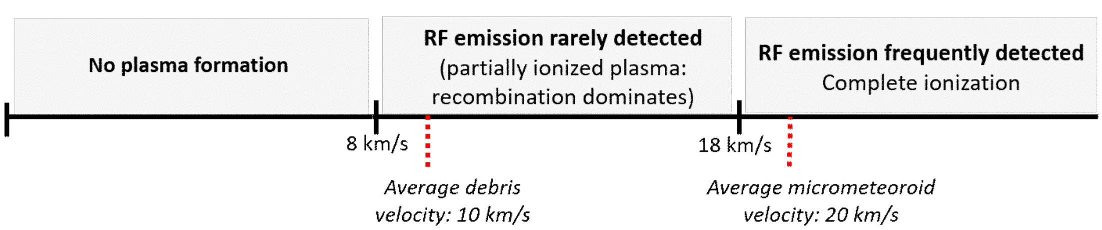

Figure 10-10: Simplified schematic showing velocity regimes in which RF emission has been detected, with average debris and micrometeoroid impact velocity labeled for reference

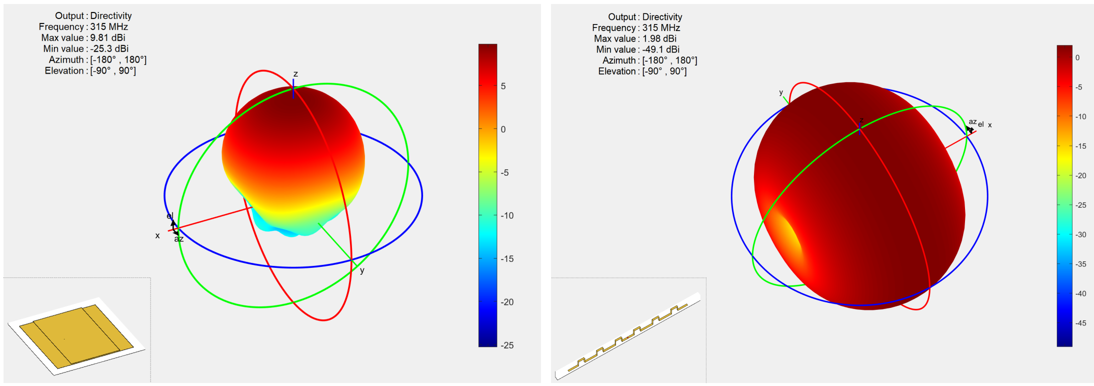

Figure 10-11: (Left) 315 MHz patch antenna receive pattern (Right) 315 MHz meander antenna receive pattern

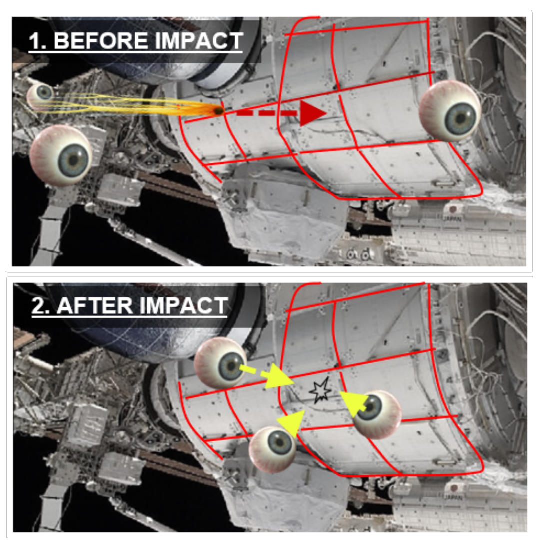

Figure 10-12: Comic showing ‘Skin and Eyes’ concept for proximity wafer-scale satellite actuators coordinating with advanced spacecraft skin, analogous to the coordination between human skin and eyes.

APPENDIX

A

Phase Alignment Measurements

For a period of 6 months, I worked on studying methods to pole bare, commercially available PVDF fiber. The measurements below show quantitative analysis of this commercial fiber that I conducted in order to prove that it has the correct crystalline alignment to behave as a sensor. However, over time, this work was put aside in favor of the commercially poled cable design used in this work.

Figure A-1 shows X-ray diffraction images of the yarn, which allows for qualitative evaluation of phase distrbutions. The peak at $2\theta = 20.26$ s related to the diffraction of β phase at (110) and (200) crystal planes. Meanwhile, the peaks at 18.3 nd 26.5 re indicative of alpha phase at (020) and (021) crystal plane, respectively. No indication of gamma phase alignment (2θ $18.5, 19.2, 20.0$) are present in the data.

Fourier Transform Infrared Spectroscopy (FTIR) is used to quantify the distribution of phases in the material. Results are shown in Figure A-2. Assuming that absorption follows the Lambert-Beer Law [49], the following derived relation is commonly used to calculate the relative fraction of beta phase in PVDF:

$$F(\beta)\ \frac{A_\beta}{(K_\beta/K_\alpha)A_\alpha\ A_\beta} \tag{A.1}$$

Where A_β is the absorption at 840nm, A_α is the absorption at 766nm, and K is the absorptivity at the respective wave number. Averaging across five FTIR images for unpoled PVDF samples, we calculate a beta phase concentration of approximately 78.5%. For comparison, PVDF thin films generally do not exceed 80% relative beta fraction [61]. See also [[8]] for a useful flowchart for deriving relative phase concentrations from FTIR data. Based on XRD and FTIR analysis, we conclude that this yarn has sufficient beta alignment for use as a sensor.

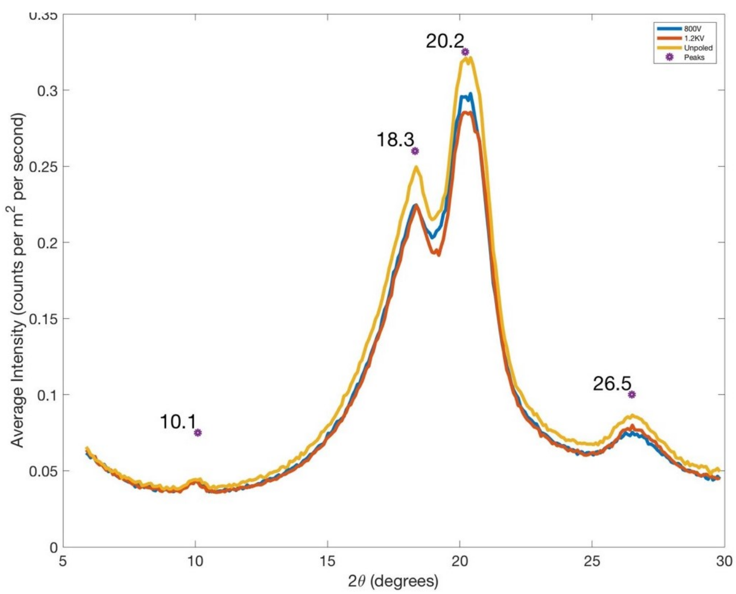

Figure A-1: X-ray diffraction image of unpoled commercial PVDF fiber. The peak at $2\theta = 20.26$ s related to the diffraction of β phase at (110) and (200) crystal planes. The peaks at 18.3 nd 26.5 re indicative of alpha phase at (020) and (021) crystal plane, respectively.

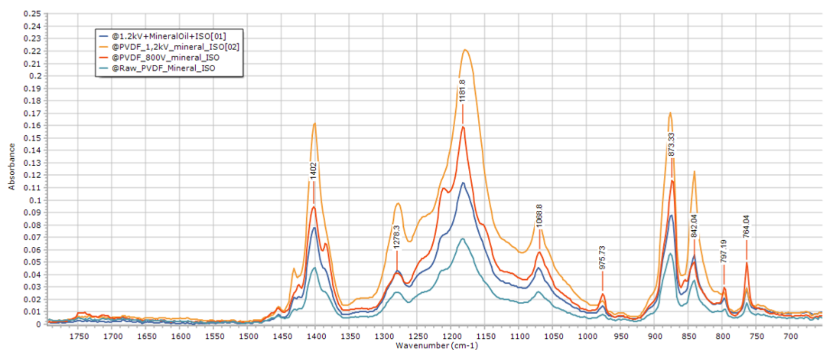

Figure A-2: Fourier transform infrared spectroscopy for PVDF yarn samples. Beta phase concentration calculated to 78.5%. Little change in spectral signatures when subject to a range of electric field strengths, suggesting that no additional beta alignment is induced from poling.

APPENDIX

B

Measurements of Fur + Charge Pulses Through wire

I experimented with simulating impact plasma charge in a crude way - by feeding pulses through a wire using a pulse generator. I built simple prototypes of conductive fur and flat conductor and positioned a wire at various distances and angles relative to each of these targets. Signals are read out using a Cremat CR-150 charge sensitive amplifier and a Cremat CR-160 pulse shaper.

The question being addressed is: how does induced voltage scale with distance for a fur target vs. flat conductor? How does the incident angle of charged particles relative to target influence this voltage profile? How might I imagine simulating this numerically in the future?

I managed to get an experimental setup up and running, and I was able to take some basic measurements to show fur outperforming a flat conductor in sensitivity. This confirms the sort of data I saw evolve out of my experiments in LASP's Van de Graaff accelerator.

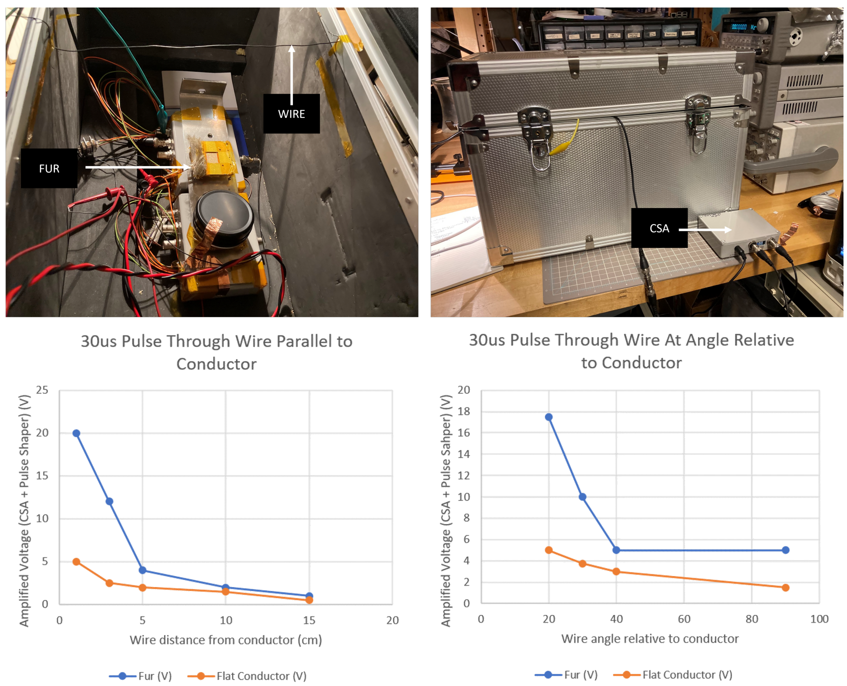

Figure B-1: Laboratory experiments with 30 μm pulses sent through nearby wire + 10k resistor

APPENDIX C

Excerpted Confocal, SEM, and EDX Microscopy

A small set of representative contamination and/or impact candidate cratering signatures are included in this appendix. These microscopy studies were extensive, and substantially more material is available on request. Imaging on spaceflight samples (fabric, fiber) and Van de Graaff accelerator samples (fabric, fiber) were conducted.

Our general objective was to search for evidence of cratering and/or iron on the sample, as iron was the sole particle type used at the Van de Graaff and is also one of the most common materials in micromteoroid samples. Late in the game, I learned from the lab manager that the resolution of the SEM-EDX available at the Institute for Soldier Nanotechnologies should not be trusted below a few μm. Therefore, it's possible that a different chemical analysis would be obtained at using a more modern machine.

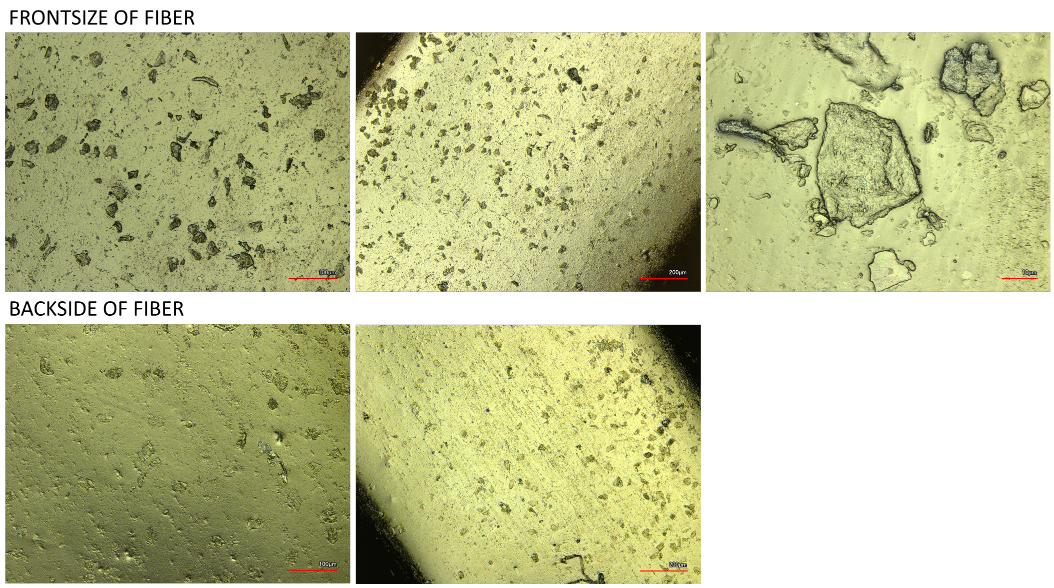

Figure C-1: Comparison between frontside and backside of thermally drawn fiber from LASP Van de Graaff studies. One side of this sample was exposed to order-of-magnitude 1000 nm-scale to few μm impactors, yet a comparison between front and back side is inconclusive.

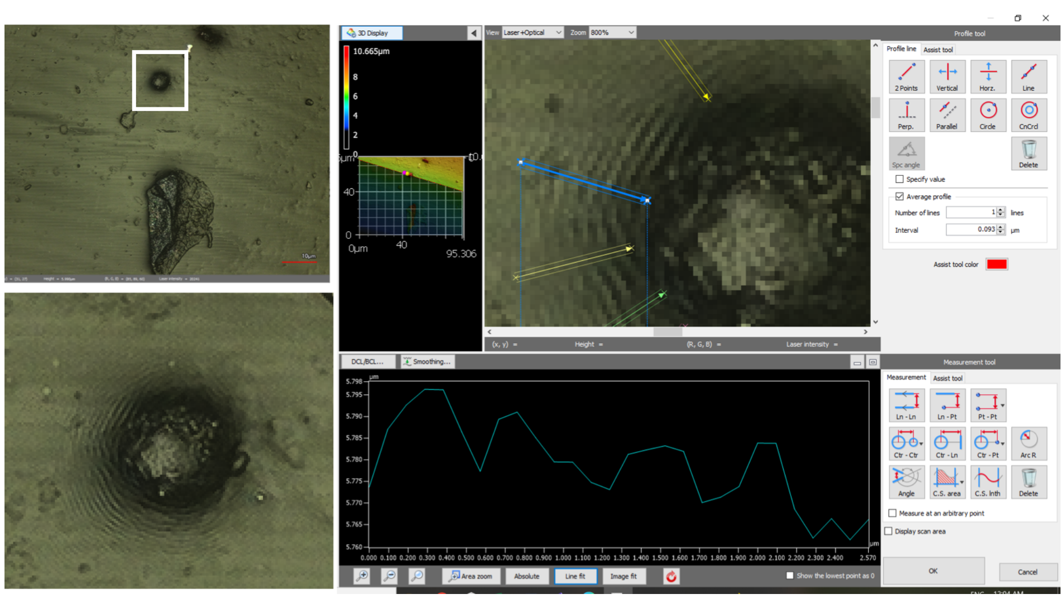

Figure C-2: Example of ripple pattern observed on the thermally drawn fiber (and measured as a slight surface roughness). This ripple pattern is ultimately believed to be an optical artifact from the confocal microscope

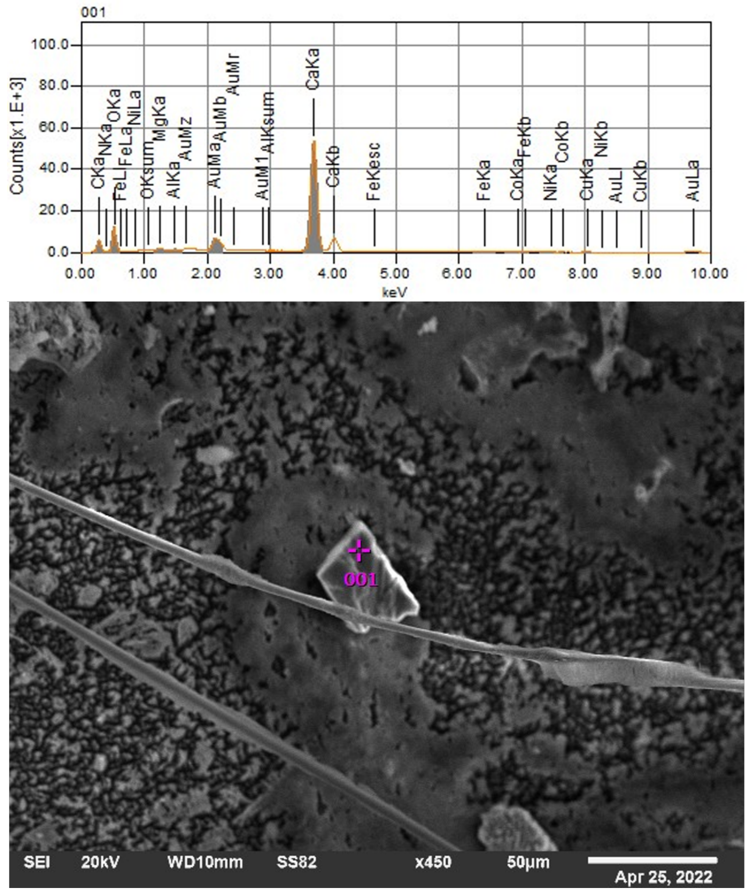

Figure C-3: Example of calcium-based contaminant particle on thermally drawn fiber from passive spaceflight (image with SEM EDX)

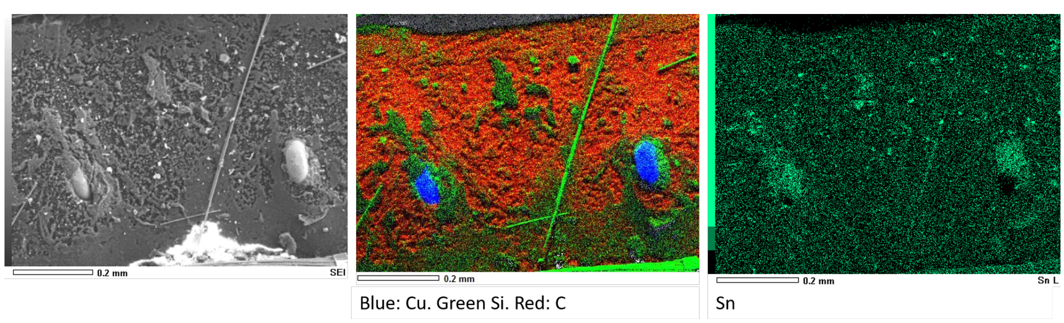

Figure C-4: Example of copper and tin-based contaminant particle (most likely solder) on thermally drawn fiber from passive spaceflight (image with SEM EDX). No iron detected. While copper might manifest in certain human-made space debris (such as from wires, PCB's, etc), it is uncommon.

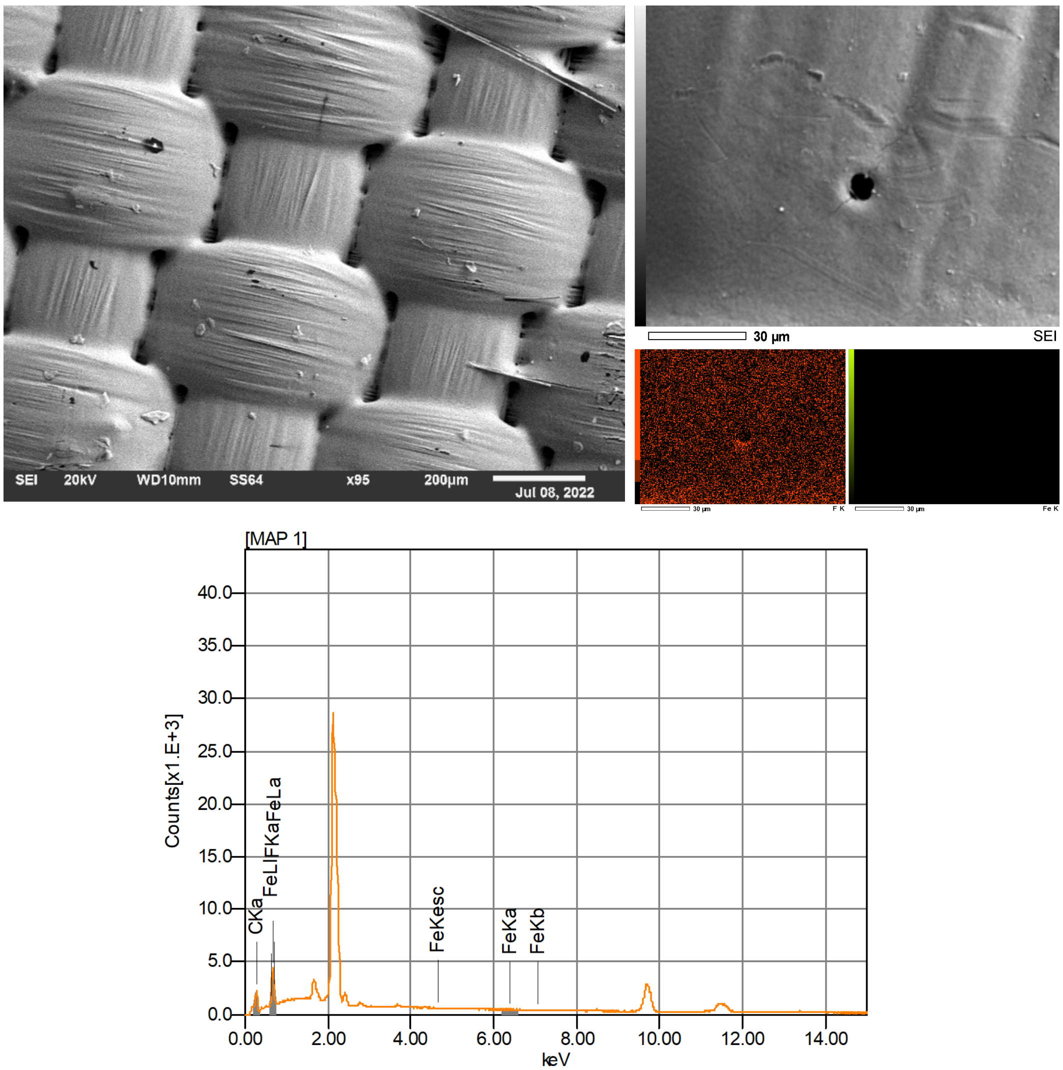

Figure C-5: Broad search on Van de Graaff goldized Beta fabric sample for iron and for cratering. Example crater shows evidence of fracturing, but may only be a defect in goldized coating.

APPENDIX

D

Additional Plots from LIPIT Campaign

Some additional plots from LIPIT. Raw data from the November, 2019 testing campaign showing thermally drawn fiber direct impact, 1cm offset impact, and 2cm offset.

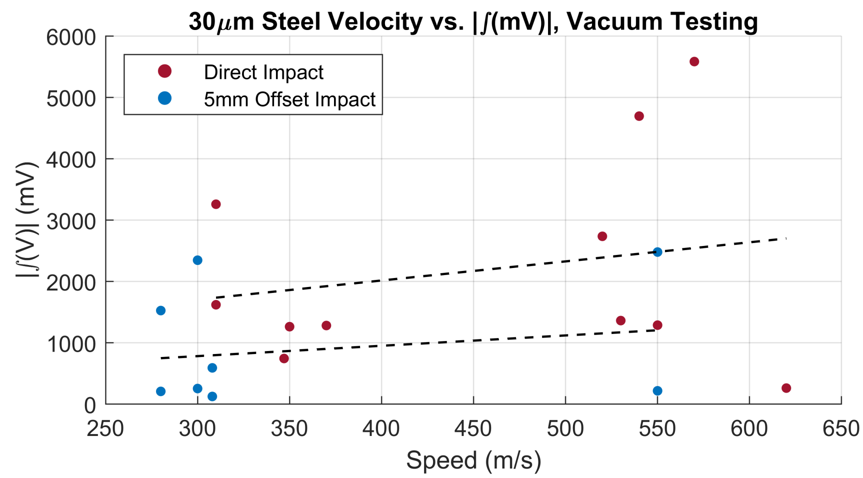

Figure D-1: Integrated signal for impact on silvered cable

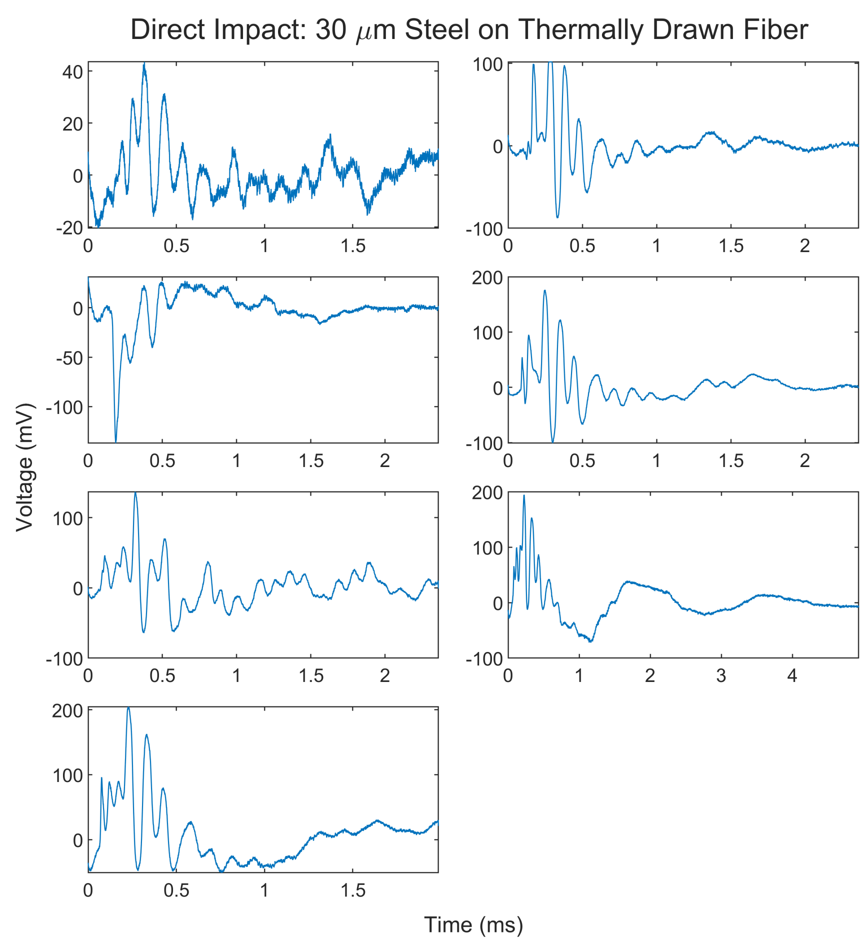

Figure D-2: Direct Impact on fabric near thermally drawn fiber

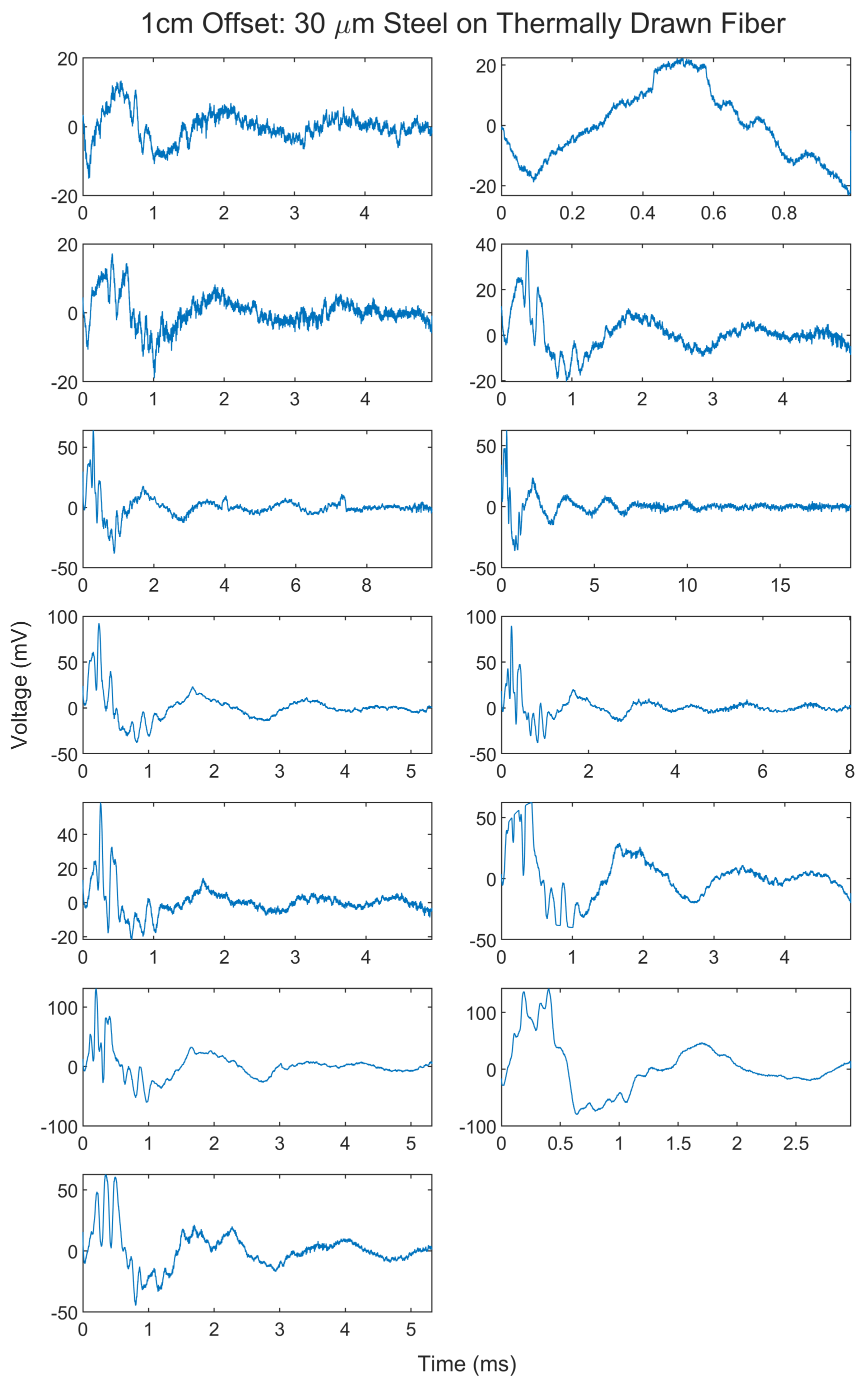

Figure D-3: 1cm offset impact on fabric near thermally drawn fiber

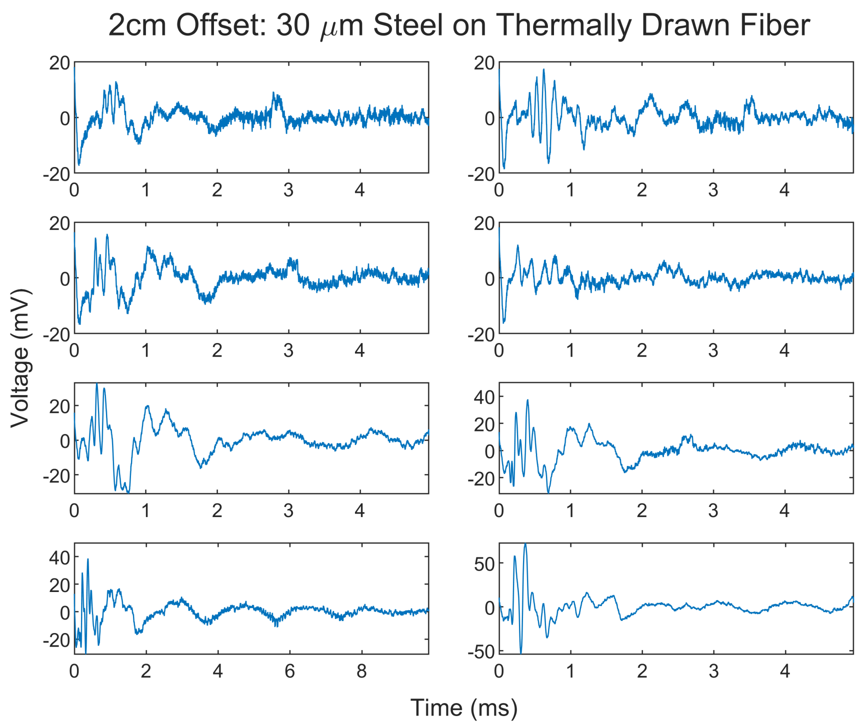

Figure D-4: 2cm offset impact on fabric near thermally drawn fiber

Bibliography

[1] . Analog devices ad5933 product web site., 2017. [Online; accessed July 7, 2022]. URL: http://www.analog.com/en/AD5933/productsearch.html.

[2] European Space Agency. Master model, 1999. URL: https://sdup.esoc.esa.int/.

[3] N Altobelli, Eberhard Grün, and M Landgraf. A new look into the helios dust experiment data: presence of interstellar dust inside the earth's orbit. *Astronomy & Astrophysics*, 448(1):243–252, 2006.

[4] Themis Athanassiadou and BD Fields. Penetration of nearby supernova dust in the inner solar system. *New Astronomy*, 16(4):229–241, 2011.

[5] Constantine A Balanis. Antenna theory: A review. *Proceedings of the IEEE*, 80(1):7–23, 1992.

[6] Claude Barbeau and Ross Cochran. Textile material for outer shell of firefighter garment, April 5 1994. US Patent 5,299,602.

[7] Martin G Broadhurst and G Thomas Davis. Ferroelectric polarization in polymers. *Ferroelectrics*, 32(1):177–180, 1981.

[8] Xiaomei Cai, Tingping Lei, Daoheng Sun, and Liwei Lin. A critical analysis of the α, β and γ phases in poly (vinylidene fluoride) using ftir. *RSC Advances*, 7(25):15382–15389, 2017.

[9] CERN. The birth of the web, 2020. URL: https://home.cern/science/computing/birth-web.

[10] Juliana Cherston and Joseph A Paradiso. Space webs as infrastructure for crawling sensors on low gravity bodies. 2017.

[11] Juliana Cherston and Joseph A Paradiso. Spaceskin: development of aerospace-grade electronic textile for simultaneous protection and high velocity impact characterization. In *Sensors and Smart Structures Technologies for Civil, Mechanical, and Aerospace Systems 2019*, volume 10970, pages 111–125. SPIE, 2019.

[12] Juliana Cherston and Joseph A Paradiso. Spaceskin: development of aerospace-grade electronic textile for simultaneous protection and high velocity impact characterization. In *Sensors and Smart Structures Technologies for Civil, Mechanical, and Aerospace Systems 2019*, volume 10970, pages 111–125. SPIE, 2019.

[13] Juliana Cherston, Paul Strohmeier, and Joseph A Paradiso. Grappler: Array of bistable elements for pinching net-like infrastructure to low gravity bodies. In *AIAA Scitech 2019 Forum*, page 0871, 2019.

[14] Juliana Cherston, David Veysset, Yuchen Sun, Joao Henrique Santos Wilbert, Hajime Yano, Keith A Nelson, Shobha Murari, and Joseph A Paradiso. Large-area electronic skins in space: vision and preflight characterization for first aerospace piezoelectric e-textile. In *Sensors and Smart Structures Technologies for Civil, Mechanical, and Aerospace Systems 2020*, volume 11379, pages 239–252. SPIE, 2020.

[15] EL Christiansen, JL Crews, JE Williamsen, JH Robinson, and AM Nolen. Enhanced meteoroid and orbital debris shielding. *International Journal of Impact Engineering*, 17(1-3):217–228, 1995.

[16] Eric L Christiansen and Dana M Lear. Toughened thermal blanket for micrometeoroid and orbital debris protection. *Procedia Engineering*, 103:73–80, 2015.

[17] A Collette, E Grün, D Malaspina, and Z Sternovsky. Micrometeoroid impact charge yield for common spacecraft materials. *Journal of Geophysical Research: Space Physics*, 119(8):6019–6026, 2014.

[18] David A Crawford and Peter H Schultz. Electromagnetic properties of impact-generated plasma, vapor and debris. *International Journal of Impact Engineering*, 23(1):169–180, 1999.

[19] AF Devonshire. Theory of ferroelectrics. *Advances in physics*, 3(10):85–130, 1954.

[20] H Dietzel, G Eichhorn, H Fechtig, E Grun, H-J Hoffmann, and J Kissel. The heos 2 and helios micrometeoroid experiments. *Journal of Physics E: Scientific Instruments*, 6(3):209, 1973.

[21] Bruce T Draine. Interstellar dust grains. *arXiv preprint astro-ph/0304489*, 2003.

[22] B.T Draine. Observed properties of interstellar dust, 2010. URL: `https://www.astro.princeton.edu/~draine/dust/Draine_IPMU_Lectures.pdf`.

[23] Eli Dwek. Iron: A key element for understanding the origin and evolution of interstellar dust. *The Astrophysical Journal*, 825(2):136, 2016.

[24] S Egusa, Z Wang, N Chocat, ZM Ruff, AM Stolyarov, D Shemuly, F Sorin, PT Rakich, JD Joannopoulos, and Y Fink. Multimaterial piezoelectric fibres. *Nature materials*, 9(8):643, 2010.

[25] Brian D Fields, John R Ellis, Walter R Binns, Dieter Breitschwerdt, Georgia A de Nolfo, Roland Diehl, Vikram V Dwarkadas, Adrienne Ertel, Thomas Faestermann, Jenny Feige, et al. Near-earth supernova explosions: Evidence, implications, and opportunities. *arXiv preprint arXiv:1903.04589*, 2019.

[26] Alex Fletcher, Sigrid Close, and Donovan Mathias. Simulating plasma production from hypervelocity impacts. *Physics of Plasmas*, 22(9):093504, 2015.

[27] David Graziosi and Ryan Lee. I-suit advanced spacesuit design improvements and performance testing. Technical report, SAE Technical Paper, 2003.

[28] Eberhard Grün, S Kempf, H Krüger, G Moragas-Klostermeyer, and R Srama. Dust astronomy. In *Proceedings of Meteoroids 2001, Conference*, pages 71–9, 2001.

[29] Eberhard Grün, Harald Krüger, and Ralf Srama. The dawn of dust astronomy. *Space Science Reviews*, 215(7):1–51, 2019.

[30] Ravi L Hadimani, D Vatansever Bayramol, N Sion, T Shah, Limin Qian, Shaoxin Shi, and E Siores. Continuous production of piezoelectric pvdf fibre for e-textile applications. *Smart Materials and Structures*, 22(7):075017, 2013.

[31] Takayuki Hirai, Michael J Cole, Masayuki Fujii, Sunao Hasegawa, Takeo Iwai, Masanori Kobayashi, Ralf Srama, and Hajime Yano. Microparticle impact calibration of the arrayed large-area dust detectors in interplanetary space (aladdin) onboard the solar power sail demonstrator ikaros. *Planetary and Space Science*, 100:87–97, 2014.

[32] WG IADC. Sensor systems to detect impacts on spacecraft. Technical report, tech. rep., Report No. IADC-08-03, 2013.

[33] ISSNL. Nickelodeon sends slime to space, 2020. URL: `https://www.issnationallab.org/blog/nickelodeons-slime-in-space-takes-off`.

[34] D James, V Hoxie, and M Horányi. Polyvinylidene fluoride dust detector response to particle impacts. *Review of Scientific Instruments*, 81(3):034501, 2010.

[35] AP Jones and N Ysard. The essential elements of dust evolution-a viable solution to the interstellar oxygen depletion problem? *Astronomy & Astrophysics*, 627:A38, 2019.

[36] CJFP Jones, CR Lawson, DJ Ayres, et al. Geotextile reinforced piled embankments. *Geotextiles, Geomembranes and Related Products, Den Hoedt (ed.)*, pages 155–160, 1990.

[37] JPL. Visions of the future, 2020. URL: `https://www.jpl.nasa.gov/visions-of-the-future/`.

[38] Dominik Koll, Gunther Korschinek, Thomas Faestermann, JM Gómez-Guzmán, Sepp Kipfstuhl, Silke Merchel, and Jan M Welch. Interstellar fe 60 in antarctica. *Physical Review Letters*, 123(7):072701, 2019.

[39] Andrei Kounine. The alpha magnetic spectrometer on the international space station. *International Journal of Modern Physics E*, 21(08):1230005, 2012.

[40] Andrzej S Krajewski, Kevin Magniez, Richard JN Helmer, and Viktoria Schrank. Piezoelectric force response of novel 2d textile based pvdf sensors. *Sensors Journal, IEEE*, 13(12):4743–4748, 2013.

[41] Manami Kurihara, Masumi Higashide, Yuu Takayanagi, Kazuyoshi Arai, Hajime Yano, Makoto Tabata, Sunao Hasegawa, and Akihiko Yamagishi. Impact frequency estimate of micron-sized meteoroids and debris on tanpopo capture panels on the iss. *Procedia Engineering*, 103:334–340, 2015.

[42] Jeffrey L Linsky, Seth Redfield, and Brian E Wood. New results concerning the environment of the heliosphere, nearby interstellar clouds, and physical processes in the inter–cloud medium. In *Journal of Physics: Conference Series*, volume 1620. IOP Publishing, 2020.

[43] Ivo Locher, Maciej Klemm, Tnde Kirstein, and Gerhard Trster. Design and characterization of purely textile patch antennas. *IEEE Transactions on advanced packaging*, 29(4):777–788, 2006.

[44] Martin L. Analog devices ad5933 product web site., 2021. [Online; accessed Sept, 2021]. URL: `https://forum.arduino.cc/t/itsybitsy-m4-dmac-adc-compile-error/891358/5`.

[45] Brian Mayton, Gershon Dublon, Spencer Russell, Evan F Lynch, Don Derek Haddad, Vasant Ramasubramanian, Clement Duhart, Glorianna Davenport, and Joseph A Paradiso. The networked sensory landscape: Capturing and experiencing ecological change across scales. *Presence*, 26(2):182–209, 2017.

[46] DJ McComas, Eric R Christian, Nathan A Schwadron, N Fox, J Westlake, F Allegrini, DN Baker, D Biesecker, M Bzowski, G Clark, et al. Interstellar mapping and acceleration probe (imap): A new nasa mission. *Space science reviews*, 214(8):1–54, 2018.

[47] Maltida McQuaid and Philip Beesley. *Extreme textiles: designing for high performance*. Princeton Architectural Press, 2005.

[48] Anna Mocker, Sebastian Bugiel, Siegfried Auer, Günter Baust, Andrew Colette, Keith Drake, Katherina Fiege, Eberhard Grün, Frieder Heckmann, Stefan Helfert, et al. A 2 mv van de graaff accelerator as a tool for planetary and impact physics research. *Review of Scientific Instruments*, 82(9):095111, 2011.

[49] Behzad Mohammadi, Ali Akbar Yousefi, and Samad Moemen Bellah. Effect of tensile strain rate and elongation on crystalline structure and piezoelectric properties of pvdf thin films. *Polymer testing*, 26(1):42–50, 2007.

[50] AV Moorhead. Nasa meteoroid engineering model (mem) version 3. Technical report, NASA, 2020.

[51] Tobin Munsat. Dust accelerator laboratory (dal). `https://impact.colorado.edu/facilities.html`. Accessed: 2022-04-20.

[52] NASA. Space station's expandable habitat, 2016. URL: `https://www.nasa.gov/image-feature/space-stations-expandable-habitat`.

[53] NASA. Small leak aboard iss, 2018. URL: `https://www.orbiter-forum.com/threads/small-leak-aboard-iss.36369/#post-550777`.

[54] NASA. Vapor tracer technology, 2020. URL: `https://www.nasa.gov/mission_pages/sounding-rockets/tracers/index.html`.

[55] Erik Nilsson, Anja Lund, Christian Jonasson, Christer Johansson, and Bengt Hagström. Poling and characterization of piezoelectric polymer fibers for use in textile sensors. *Sensors and Actuators A: Physical*, 201:477–486, 2013.

[56] NASA ORBITAL DEBRIS PROGRAM OFFICE. Debris measurements, 2020. URL: `https://www.orbitaldebris.jsc.nasa.gov/measurements/`.

[57] Syamantak Payra, Irmandy Wicaksono, Juliana Cherston, Cedric Honnet, Valentina Sumini, and Joseph A Paradiso. Feeling through spacesuits: Application of space-resilient e-textiles to enable haptic feedback on pressurized extravehicular suits. In *2021 IEEE Aerospace Conference (50100)*, pages 1–12. IEEE, 2021.

[58] Veljko Radeka. Low-noise techniques in detectors. *Annual Review of Nuclear and Particle Science*, 38(1):217–277, 1988.

[59] Le Petit Robert. Experience, 2020. URL: `https://dictionnaire.lerobert.com/definition/experience`.

[60] Tomas Saraceno. Particular matter(s). Exhibition, The Shed (New York City), 4 2022. Photograph retrieved online at https://studiotomassaraceno.org/printed-matters/.

[61] Vitor Sencadas, M Vitor Moreira, Senentxu Lanceros-Méndez, António Sergio Pouzada, and Rinaldo Gregório Filho. α-to β transformation on pvdf films obtained by uniaxial stretch. In *Materials science forum*, volume 514, pages 872–876. Trans Tech Publ, 2006.

[62] Nick Siegler, Rudra Mukherjee, and Harley Thronson. The future of space astronomy will be built: Results from the nasa-chartered in-space assembled telescope (isat) study. In *AAAS/235th Meeting of the American Astronomical Society*. Pasadena, CA: Jet Propulsion Laboratory, National Aeronautics and Space ..., 2020.

[63] Jonathan D Slavin, Eli Dwek, Mordecai-Mark Mac Low, and Alex S Hill. The dynamics, destruction, and survival of supernova-formed dust grains. *The Astrophysical Journal*, 902(2):135, 2020.

[64] Frank Spahn, Jurgen Schmidt, Nicole Albers, Marcel Horning, Martin Makuch, Martin Sei, Sascha Kempf, Ralf Srama, Valeri Dikarev, Stefan Helfert, et al. Cassini dust measurements at enceladus and implications for the origin of the e ring. *Science*, 311(5766):1416–1418, 2006.

[65] Helmuth Spieler. Semiconductor detectors part 2. *Lectures on Detector Techniques, http://physics. lbl. gov/spieler, Stanford Linear Accelerator Center, Stanford, CA*, page 2, 1999.

[66] Zoltan Sternovsky, AJ Gemer, E Grün, M Horanyi, S Kempf, K Maute, F Postberg, R Srama, and E Williams. Hyperdust: An advanced in-situ

detection and chemical analysis of microparticles in space. In *2015 IEEE Aerospace Conference*, pages 1–10. IEEE, 2015.

[67] Zoltan Sternovsky, Eberhard Grün, Keith Drake, Jianfeng Xie, Mihaly Horanyi, Ralf Srama, Sascha Kempf, Frank Postberg, Anna Mocker, Siegfried Auer, et al. Novel instrument for dust astronomy: Dust telescope. In *2011 Aerospace Conference*, pages 1–8. IEEE, 2011.

[68] Masaki Watanabe, Hironori Sahara, Shinsuke Abe, Takeo Watanabe, Yuta Nojiri, and Lena Okajima. Development of artificial meteor for observation of upper atmosphere. *Acta Astronautica*, 121:172–178, 2016.

[69] Joseph C Weingartner and BT Draine. Dust grain-size distributions and extinction in the milky way, large magellanic cloud, and small magellanic cloud. *The Astrophysical Journal*, 548(1):296, 2001.

[70] Darrel L Williams, Samuel Goward, and Terry Arvidson. Landsat. *Photogrammetric Engineering & Remote Sensing*, 72(10):1171–1178, 2006.

[71] Stanley E Woodard. Sansec sensing technology—a new tool for designing space systems and components. In *Aerospace Conference, 2011 IEEE*, pages 1–11. IEEE, 2011.

[72] Wei Yan, Grace Noel, Gabriel Loke, Elizabeth Meiklejohn, Tural Khudiyev, Juliette Marion, Guanchun Rui, Jinuan Lin, Juliana Cherston, Atharva Sahasrabudhe, et al. Single fibre enables acoustic fabrics via nanometre-scale vibrations. *Nature*, 603(7902):616–623, 2022.